Improving the seismic image in Reverse time migration by analysis of wavefields via continuous wavelet transform

Improving the seismic image in Reverse time migration by analysis of wavefields via continuous wavelet transform

Thesis

A Thesis submitted in partial fulfillment of the requirements for the degree of
Doctor of Philosophy in Mathematical Engineering

by

Juan Guillermo Paniagua Castrillón

MSc. in Engineering
born in Medellín, Colombia.

This thesis has been approved by the promoter:

Prof. dr. O.L. Quintero

Composition of the Promotion Committee::

Prof. dr. L. Ángel Toro,	Universidad EAFIT, Dean of the School of Sciences
Prof. dr. C. M. Vélez Sánchez,	Universidad EAFIT, Head of Department of Mathematical Sciences
Prof. dr. A. Sicard-Ramírez,	Universidad EAFIT, Department of Mathematical Sciences
Prof. dr. O. García Jaimes,	Universidad EAFIT, Department of Mathematical Sciences
Prof. dr. C. A. Cadavid Moreno,	Universidad EAFIT, Department of Mathematical Sciences
Prof. dr. O. L. Quintero Montoya,	Universidad EAFIT, Academic Director PhD program
Prof. dr. R. E. Velásquez Ossa,	Universidad de Antioquia, External professor

Keywords: Seismic migration, imaging condition,reverse time migration, wavelet transform

Printed by: Universidad EAFIT

An electronic version of this dissertation is available at
https://repository.eafit.edu.co/handle/10784/20.

There does not exist a category of science to which one can give the name applied science. There are science and the applications of science, bound together as the fruit of the tree which bears it.

Louis Pasteur

Contents

Abstract

We will summarize the contributions of this thesis.

During the last 50 years there has been a lot of effort to obtain subsurface structures on the oil and gas exploration. Some of them even if they are based on the mathematical formulation of the phenomenon, were not easily implemented due to the lack of computational power.
Nevertheless, the problem is not only the algorithmic complexity but also, the uncertainty reduction of the scalar field that is obtained after the mathematical modeling and inversion procedures.
Specifically, this thesis deals with the well known Reverse time migration (RTM) procedure, which is basically the two-way wave equation migration that is able to generate models with both great structural and velocity complexities, problems arise when the construction of subsurface models take into account seismic signals recorded on the surface. The data is mapped into the subsurface using the acoustic wave equation and the models obtained contain uncertainties that affect their subsequent interpretation.
In order to reduce these uncertainties, we seek to improve the algorithm used in RTM before and after the generation of the final model looking for uncertainty reduction and improved scalar fields.
We propose a set of strategies of extracting information from the seismic signals in order to obtain characteristics that allow a better and more refined representation of the subsurface structure model. Integral transforms are developed for this purpose.
Inspired on the concept of information retrieval from data, we developed a signal procedure algorithm to determine in time-scale domain, the main features of the traveler wave in order to relate temporarily the inherent physics phenomena, locate complex structures by pointing the velocity field singularities due to the main changes on the frequency content revealed within the scalogram obtained by Gaussian wavelet family.
Later on, a wavefield separation for the scalar field calculation is proposed based on the same principle and we called it Time Scale Wavefield Separation (TSWS). The space defined by Source wave propagation is decomposed on the subspaces and the analysis in time-domain time-scale of the subset of the wavefield is performed by selecting special features extracted by Wavelet Transform Modulus Maxima (WTMM) and a numerical algorithm is introduced for massive data [1].
Consequently, a Depth Scale Wavefield Separation (DSWS) is developed to the Receiver Wavefield separation by extracting the depth-domain scale-domain features of the relevant information of the reverse traveler wave [2].
Finally and taking into account the need for the proper structure definition for drilling purposes, we introduced the Laguerre Gauss Transform as final part of the Zero lag cross correlation imaging condition (ZL-CC-IC-LG) and provide a useful transformation of the final real scalar field into a complex scalar field with properties of spatial features enhancement [3, 4, 5, 6].

References

[1] J. G. Paniagua and O. L. Quintero, *Singularity analysis of receiver field and its relation to RTM imaging condition,* Paper submitted to Nature Geoscience (2017).

[2] J. G. Paniagua and O. L. Quintero, *Time-scale depth-scale domain wavefield separation in reverse time migration,* Paper submitted to IEEE Signal Processing Magazine (2017).

[3] J. G. Paniagua and D. Sierra-Sosa, *Laguerre Gaussian filters in Reverse Time Migration image reconstruction,* VII Simpósio Brasileiro de Geofísica. Expanded abstract (2016).

[4] J. G. Paniagua and O. L. Quintero, *The use of Laguerre-Gauss transform in 2D reverse time migration imaging,* 15th International Congress of the Brazilian Geophysical Society. Expanded abstracts (2017).

[5] J. G. Paniagua and O. L. Quintero, *Attenuation of reverse time migration artifacts using Laguerre-Gauss filtering,* 79th EAGE Conference and exhibition. Extended abstracts (2017).

[6] J. G. Paniagua, D. Sierra-Sosa, and O. L. Quintero, *Laguerre-Gauss filters in reverse time migration image reconstruction,* Revista Brasileira de Geofísica (2017).
dissertation

1

Introduction

This thesis is focused on the construction of subsurface models from seismic signals recorded on the surface. The data is mapped into the subsurface using the acoustic wave equation. Reverse time migration (RTM) is a two-way wave equation migration that is able to generate models with both great structural and velocity complexities. The scalar fields obtained contain uncertainties that affect their subsequent interpretation. In order to reduce these uncertainties, we seek to improve the algorithm used in RTM before and after the generation of the final model looking for uncertainty reduction. Based on the main hypothesis that a traveler wave propagating through a very singular velocity field experiences changes characterizables, a method based on integral transforms for signal analysis is designed. Consequently, we obtain the main features of the traveler wave in order to relate temporarily the inherent physics phenomena, and locate complex structures by pointing the velocity field singularities due to the main changes on the frequency content revealed by Gaussian wavelet family. We also propose a set of strategies of extracting information from the wavefield subspaces signals in order to obtain characteristics that allow a better and more refined representation of the subsurface structure model. A analog approach was also developed for the real scalar field.

1

Problem statement

In the exploration stage of the oil industry it is very important the interpretation of approximated models of the subsurface structure, obtained from signals recorded on the surface by applying a seismic method in a particular region. These models have some degree of uncertainty due to the characteristics of the subsurface, geological structure and the specific method used to obtain them. One of the major tools to obtain models of the subsurface structure is seismic imaging or seismic migration.

Seismic migration should not be confused with the seismic method. The seismic method is the artificial production of mechanical waves by means of impacts or explosions on the surface, to be registered later on stations called geophones (or hydrophones) that are distributed along the surface.

Seismic migration is a process to obtain the information of the subsurface structures using mechanical waves and signals which information is recorded in receivers located on the surface of the ground (on-shore) or sea (off-shore). In seismic exploration, sources produce energy that disturbs the surface of the ground and generate mechanical waves which travel into the deep subsurface. Mechanical waves can be reflected, diffracted or refracted when they reach any contrast in seismic properties, such as velocity or density [1].

Migration is defined as the process which takes the seismic section, denoted as $d(\mathbf{g}, t|\mathbf{x}_s, 0)$ and moves the reflection events back to their origin at the interfaces. Mathematically, migration maps the signals recorded on the surface, $d(\mathbf{g}, t|\mathbf{x}_s, 0)$, into the reflectivity distribution $m(\mathbf{x})$, denoted as the scalar field or migrated model (See eq. 1.1).

Seismic reflection is a geophysical method that provides seismic models with greater resolution at depth than other seismic methods and it is the choice for hydrocarbon-reservoir exploration. It allows to obtain high accuracy, high resolution and penetration in depth. Consequently, the data and information obtained from arrivals of reflected signals are considered.

Seismic reflection methods can be classified in two categories: Ray-based methods, such as Kirchhoff depth migration and beam migration, and wave-equation-based methods, such as one-way wave equation migration (OWWE) and two-way wave equation methods or reverse time migration (RTM) [2].

Reverse time migration (RTM) is a two-way wave equation migration that is able to generate models with both great structural and velocity complexities.

Reverse time migration solves with greater accuracy the two-way acoustic wave equation for wavefield propagation, and it has proven to be the preferred imaging algorithm in many geologically complex structures due to the fact that it is not restricted by steep dips or overhangs; that is, no limitations on dip angles, achieving more accurate amplitudes of the reflectors and better location of the structures.

Superiority of RTM over other migration algorithms results from the fact that the full wave equation is solved to extrapolate the wavefields simulating the propagation of the waves in any direction without plunge limitations and illuminating overturned structures and other complex structures. These conditions are common in salt basins and other geologic basins with complex structures and velocity distributions.

This algorithm is becoming more and more attractive to the industry because of its robustness in subsurface models with complex geology [3].

Reverse time migration (RTM) consists in three basic steps: forward propagation of source wavefield, backward propagation of receiver wavefield, and application of an mathematical operation to relate the source and receiver wavefields to obtain the final scalar field (Final model). In order to implement RTM is necessary to have as initial condition highly uncertain because of the velocity field of the wave in the media and the signals recorded on the surface, obtained through a seismic acquisition.

Reverse time migration can be represented mathematically by the integral equation [4]:

$$m(\mathbf{x}) = \int_D [g(\mathbf{g}, -t|\mathbf{x}, 0) * d(\mathbf{g}, t|\mathbf{x}_s, 0)] \otimes [f(t) * g(\mathbf{x}, t|\mathbf{x}_s, 0)]\big|_{t=0} dg \qquad (1.1)$$

where $\mathbf{x} = (x, y, z)$ is the location in the Cartesian coordinate system in the semi-infinite domain D, where $z > 0$; $f(t)$ is the source wavelet function; $g(\mathbf{g}, t|\mathbf{x}_s, 0)$ is the acausal Green's function; $d(\mathbf{g}, t|\mathbf{x}_s, 0)$ is the shot gather traces; $g(\mathbf{g}, -t|\mathbf{x}, 0) * d(\mathbf{g}, t|\mathbf{x}_s, 0)$ is the back propagated field to be called "the receiver wavefield", $R(\mathbf{x}, \mathbf{x}_s, t)$; $f(t) * g(\mathbf{x}, t|\mathbf{s}, 0)$ is the forward propagated source field for a single source at $\mathbf{x}_s$ to be called "the source wavefield", $S(\mathbf{x}, \mathbf{x}_s, t)$; and $m(\mathbf{x})$ is the RTM migration model. Symbol $\otimes$ represents the temporal dot product.

The scalar field (migrated model) $m(\mathbf{x})$ is kinematically accurate at points where the waves are reflected due to incident and reflected wavefields coincident in space and time, but the migrated amplitudes no longer hold any physical meaning. Nonetheless, it produces kinematically correct models of the geometry of the subsurface structure, that is, an approximated structural model [5].

As consequence of the unwanted correlation of diving, head and backscattered waves the model is contaminated with low spatial frequency uncertainty (It is commonly called Artifacts) [6]. However, for large impedance contrasts on the initial condition (Velocity field), the low frequency uncertainty becomes stronger and distorts the migrated model [7, 8]. In presence of strong velocity changes, strong amplitude changes occur and the appearance of artifacts is greater than in smooth velocity changes [9].

These artifacts occur most frequently in shallow parts and hard interfaces, that can be understood as singularities in the velocity field, can mask important details in the model [10, 11] which are the significant difference between a good or bad drilling process and it will allow an adequate use of exploration resources.

Different strategies have been proposed to attenuate or remove these artifacts. Some researchers proposed modifications of the acoustic wave equation in order to attenuate reflections at the boundaries [12, 13]; others modified the conventional zero-lag cross-correlation imaging condition or proposed different imaging conditions [14, 15, 16]; and different filtering techniques were implemented to post-processed the migrated images [17, 18].

1

Research hypothesis

The aim of this thesis is to reduce the numerically induced uncertainties by RTM procedure and the possible error in the scalar field called migrated model obtained by (1.1), also to provide a solution based on the proper understanding of the phenomenon and related it to the real dynamics of the traveler wave under the surface. Based on the main hypothesis that a traveler wave propagating through a very singular velocity field experiences changes characterizables, there must be representation that simplifies the interest features.

Consequently, it will be possible to obtain the main features of the traveler wave in order to relate temporarily the inherent physics phenomena, and locate complex structures by pointing the velocity field singularities due to the main changes on the frequency content?

If yes, can be obtained a kernel that provides accurate and valuable information about these changes? Would it be the Wavelet analysis an optimal feature extraction theoretical framework? Is the Gaussian family a kernel that maximize the information retrieval due to their properties as heat equation solution [19, 20] and its compromise of time-scale on the Heisenberg uncertainty rectangle?

Would it be possible to develop a set of strategies of extracting information from the wavefield subspaces signals in order to obtain characteristics that allow a better and more refined representation of the subsurface structure model compensating the uncertainties induced by (1.1)?

Contributions

In this work, we analyze the time-scale features of the seismic signals generated by the wave propagation via continuous wavelet transform, scale domain is understood as the inverse of frequencies. These seismic signals correspond to the subspaces created from the fields mapped by the function solution of the acoustic wave equation immersed in the reverse time algorithm in forward and backward direction. The extraction of relevant information featured by the Hölder exponent -via Maximum Modulus Wavelet Transform- from incident and reflected wavefields, which are the upgoing and downgoing components of the source and receiver wavefields, allows to reach this goal.

Accordingly, this wavefield separation provides a framework for the significant reduction of uncertainties to interpretation and numerical errors, the improvement of the spatial and temporal location of the reflective events and a better approximation in the enhancement of subsurface structures in comparison with the recent contributions found in literature [3, 21, 22, 23].

Continuous wavelet transform and singularity analysis via Maximum Modulus Wavelet Transform have been applied in some branches of sciences such as wave propagation, data compression, signal processing, image processing, pattern recognition, computer graphics, the detection of aircraft and submarines and other medical image technology [24, 25, 26, 27]. In Geophysics and Mathematical Engineering, we have not found any applications related with wavefield decomposition [28]. The contribution of this thesis lies in locating in time-scale, space-time reflection events

or changes in impedance (Field singularities) present in complex structures of the subsurface. Similarly, the robustness of the proposed method is given by the ability to perform the analysis and separation of wavefields in the presence of attenuation of the waves since the analysis can be performed at very low and high scales (high and low frequencies) due to the range of resolutions that can be reached [29].
The proposed method allows to obtain a model with high resolution and fidelity, a clear delineation of structures in complex geological areas both onshore and offshore and with a good preservation of the amplitude field so that it can be related to the reflectivity of the medium, thus leading to the narrowing of the gap of uncertainty in the interpretation and decreased exploration costs.

In addition and related to the post processing stage in RTM, we proposed the use of the linear integral transformation called Laguerre-Gauss transform [30] in the post-processing of the scalar field obtained by eq. (1.1). This integral transformation maps the scalar real field (Model) $m(x)$ to a complex scalar field $\tilde{m}(x)$, which represents the processed migrated model, with a significant reduction of low and high frequency noises and with an edge enhancement. An effect associated with the application of the Laguerre-Gauss transform is a π phase shift in the reflectors compared to the $\frac{\pi}{2}$ phase shift of the traditional laplacian filtering. The subsurface structures are well delineated and located in their correct position and the transformation has the property of detecting very small phase shifts and intensity changes in the model [31, 32, 33, 34].

The mentioned contributions will enhance the capability of human interpretation of the migrated image and improve the exploration process in complex structures onshore and offshore (Cases like the Caribbean sea and Piedemonte llanero in Colombia), where it is traditionally difficult to explore due to lateral changes in the velocity of propagation of the seismic waves and high values of angles of dip, causing that the reflective events appear located in different places to their real position. In addition, it will increase the possibility of success in oil exploration, especially in Colombia where legislation and popular actions have avoided drilling of wells and affected the sustainable development of the oil industry.
The scope of this thesis is based on the achievement of the objectives described as follows.

1.1. General objective

To Design and implement tools and mathematical methods to improve seismic scalar fields (Models) obtained by reverse time migration so that an excellent focusing of energy, definition of structures and preservation of the attributes of the seismic data is achieved; contributing to the decrease in the degree of uncertainty in the process of interpretation of seismic methods results in hydrocarbon exploration.

1.2. Specific objectives

1. To perform a mathematical analysis of the topological spaces generated in the wave propagation in an acoustic media and its effects on the source and receiver illumination maps and the cross correlation imaging condition.

2. To extract useful information for the enhancement the $2D$ RTM technique and analyze its effect on the results.

3. To propose and implement a new imaging condition, modification or post processing technique of cross correlation imaging condition based on the study and analysis of the topological properties of the spaces generated through the use of mathematical methods, such as linear integral transforms, in the source and receiver wavefields.

4. To study, implement and analyze the different imaging conditions and the regularization or stabilization techniques to avoid divisions by zero used in reverse time migration.

1.3. Outline of the thesis

This thesis begins with the theoretical foundation of reverse time migration (RTM) and how it generates models under uncertainties in Chapter 2. This includes some numerical examples which show the uncertainties in the model and different strategies to avoid or reduce these uncertainties are described.

Chapter 3 introduces the singularity spectrum algorithm for a signal applied to a receiver wavefield at $z = 0$ and analyze the features time-scale of the traces, extracting their main features in time-scale domain proving clues for the possible reduction of uncertainties that appears in RTM models. We propose a method to extract relevant features about the receiver wavefield in order to use this information on the subsurface contained to understand phenomena related to attenuation and reflection. In addition, this method can be used to characterize the frequency spectrum and to analyze changes in the velocity field and their effect on wave propagation.

Chapter 4 discusses and proposes a new method to separate the components of the wavefields via maximum modulus wavelet transform and Hölder exponent in order to analyze and characterize the seismic signals and extract relevant information that allows to improve the scalar fields obtained by RTM. The proposed method will allow to obtain a scalar field with high resolution and fidelity, a clear delineation of structures in complex geological areas.

In Chapter 5 a new post-processing method of the RTM scalar fields is developed. The proposed method is based on the Laguerre-Gauss transform and some spectral features of the transformation are discussed. In addition, the improvement of the final models are shown through some synthetic datasets.

During the development of this thesis, some publications were achieved and they are cited below:

J. G. Paniagua and D. Sierra-Sosa, Laguerre Gaussian filters in Reverse Time Migration image reconstruction, VII Simpósio Brasileiro de Geofísica, expanded abstract (2016).

Paniagua, J.G., Sierra-Sosa, D. and Quintero, O. L. Técnica no convencional para la condición de imágenes sísmicas. Seminario INNOVA ECOPETROL (2016).

Paniagua, J.G. Improving the seismic image in Reverse time migration by analyzing of wavefields and post processing the zero lag Cross Correlation imaging condition. II Workshop en Modelado, Migración, Inversión Sísmica y Aplicaciones Geofísicas (2016).

J. G. Paniagua and O. L. Quintero, The use of Laguerre-Gauss transform in 2D reverse time migration imaging, 15th International Congress of the Brazilian Geophysical Society. Expanded abstracts (2017).

Paniagua, J.G. Extracting information from wavefields using the continuous wavelet transform. III Workshop en Modelado, Migración e Inversión Sísmica (2017).

J. G. Paniagua and O. L. Quintero, Attenuation of reverse time migration artifacts using Laguerre-Gauss filtering, 79th EAGE Conference and exhibition. Extended abstracts (2017).

J. G. Paniagua and D. Sierra-Sosa, Laguerre-Gauss filters in reverse time migration image reconstruction, Revista Brasileira de Geofísica (2017).

J. G. Paniagua and O. L. Quintero, Singularity analysis of receiver field and its relation to RTM imaging condition, Paper submitted to Nature Geoscience (2017).

J. G. Paniagua and O. L. Quintero, Time-scale depth-scale domain wavefield separation in reverse time migration, Paper submitted to IEEE Signal Processing Magazine (2017).

In addition, an academic internship was done in the Faculty of Electrical Engineering, Mathematics and Computer Science at Delft University of Technology, in the Netherlands .

References

[1] H. Zhang, *Seismic Exploration of Hydrocarbons in Heterogeneous Reservoirs* (Elsevier Inc., 2015).

[2] J. P. Leveille, I. F. Jones, B. Wang, and F. Liu, *Subsalt imaging for exploration, production, and development: a review,* Geophysics **76**, WB3 (2011).

[3] F. Liu, G. Zhang, S. Morton, and J. Leveille, *An effective imaging condition for reverse time migration using wavefield decomposition,* Geophysics **76**, 29 (2011).

[4] G. T. Schuster, *Basics of seismic imaging* (Cambridge University Press, 2010).

[5] S. Chattopadhyay and G. McMechan, *Imaging conditions for prestack reverse time migration,* Geophysics **73**, 81 (2008).

[6] S. Y. Sun and J. Cai, *Reverse-time migration by fan filtering plus wavefield decomposition,* SEG 2009 International Exposition and Annual Meeting , 2804 (2009).

[7] B. Kaelin and A. Guitton, *Imaging condition for reverse time migration,* 76th International Annual Meeting and exposition, SEG, Expanded abstracts , 2594 (2006).

[8] J. B. Tary, M. Van der Baan, and R. H. Herrera, *Attenuation estimation using high resolution time–frequency transforms,* Digital Signal Processing **60**, 46 (2017).

[9] D. Loewenthal, P. Stoffa, and E. Faria, *Suppressing the unwanted reflections of the full wave equation,* Geophysics **52**, 1007 (1987).

[10] I. F. Jones, *Tutorial: migration imaging conditions,* First break **32**, 45 (2014).

[11] I. F. Jones and I. Davison, *Seismic imaging in and around salt bodies,* Interpretation **24**, SL1 (2014).

[12] E. Baysal, D. D. Kosloff, and J. W. Sherwood, *A two way nonreflecting wave equation,* Geophysics **49**, 132 (1984).

[13] R. Fletcher, P. Fowler, and P. Kitchenside, *Suppressing artifacts in prestack reverse time migration,* 75th International Annual Meeting, SEG, Expanded abstracts , 2049 (2005).

[14] J. Costa, F. Silva, R. Alcántara, J. Schleicher, and A. Novais, *Obliquity-correction imaging condition for reverse time migration,* Geophysics **74**, S57 (2009).

[15] A. Guitton, A. Valenciano, D. Bevc, and J. Claerbout, *Smoothing imaging condition for shot-profile migration,* Geophysics **72**, 149 (2007).

[16] R. Pestana, A. Dos Santos, and E. Araujo, *RTM imaging condition using impedance sensitivity kernel combinated with the Poynting vector,* SEG Technical Program Expanded Abstracts , 3763 (2014).

[17] O. Youn and H. Zhou, *Depth imaging with multiples,* Geophysics **66**, 246 (2001).

[18] A. Guitton, B. Kaelin, and B. Biondi, *Least-square attenuation of reverse time migration,* 76th International Annual Meeting, SEG, Expanded abstracts , 2348 (2006).

[19] S. Mallat and W. Hwang, *Singularity detection and processing with wavelets,* Information Theory, IEEE Transactions on **38**, 617 (1992).

[20] S. Mallat, *A Wavelet Tour of Signal Processing*, 2nd ed., edited by A. Press (Academic Press, 2009).

[21] T. W. Fei and Y. Luo, *De-blending reverse time migration,* SEG 2010 International Exposition and Annual Meeting , 3130 (2010).

[22] T. Chen and B. He, *A normalized wavefield separation cross-correlation imaging condition for reverse time migration based on Poynting vector,* Applied Geophysics **11**, 158 (2014).

[23] E. Wang and Y. Liu, *Reverse time migration using analytical wavefield and wavefield decomposition imaging condition,* 86th Annual International Meeting, SEG, Ex- panded abstracts , 4461 (2016).

[24] R. Struzik, *Local Effective Hölder Exponent Estimation on the Wavelet Transform Maxima Tree,* in *Fractals* (Springer, 1999) pp. 93–112.

[25] B. H. Chen, H. Z. Wang, S. H. Yang, and C. McGreavy, *Application of wavelets and neural networks to diagnostic system development, 1, feature extraction,* Computers & Chemical Engineering **23**, 899 (1999).

[26] C. Tu, W. Hwang, and J. Ho, *Analysis of Singularities From Modulus Maxima of Complex Wavelets,* IEEE Transactions on information theory **51**, 1049 (2005).

[27] P. Addison, *Wavelet transforms and the ECG: a review,* Physiological measurement **26**, R155 (2005).

[28] J. G. Paniagua and O. L. Quintero, *Singularity analysis of receiver field and its relation to RTM imaging condition,* Paper submitted to Nature Geoscience (2017).

[29] J. G. Paniagua and O. L. Quintero, *Time-scale depth-scale domain wavefield separation in reverse time migration,* Paper submitted to IEEE Signal Processing Magazine (2017).

[30] W. Wang, T. Yokozeki, R. Ishijima, M. Takeda, and S. G. Hanson, *Optical vortex metrology based on the core structures of phase singularities in Laguerre-Gauss transform of a speckle pattern,* Optics Express **14**, 10195 (2006).

[31] J. G. Paniagua and D. Sierra-Sosa, *Laguerre Gaussian filters in Reverse Time Migration image reconstruction,* VII Simpósio Brasileiro de Geofísica. Expanded abstract (2016).

[32] J. G. Paniagua, D. Sierra-Sosa, and O. L. Quintero, *Laguerre-Gauss filters in reverse time migration image reconstruction,* Revista Brasileira de Geofísica (2017).

[33] J. G. Paniagua and O. L. Quintero, *The use of Laguerre-Gauss transform in 2D reverse time migration imaging,* 15th International Congress of the Brazilian Geophysical Society. Expanded abstracts (2017).

[34] J. G. Paniagua and O. L. Quintero, *Attenuation of reverse time migration artifacts using Laguerre-Gauss filtering,* 79th EAGE Conference and exhibition. Extended abstracts (2017).

2

Reverse time migration

One of the major tools to obtain models of the subsurface structures is seismic migration. In geologically complex zones with steep dips and strong velocity contrasts, the two-way wave equation methods produce better models than other methods such as Kirchhoff migration or one-way wave equations methods.

This chapter describe a two-way wave equation method called reverse time migration. The integral equation that represents the reverse time migration operator allows to find models of the subsurface with uncertainties. These uncertainties should be reduced to get a refined subsurface model with closeness to reality.

The general theory and wave equations used in wave extrapolation and the imaging condition are shown. Although reverse time migration is considered as the best imaging algorithm for complex areas, it is not free of problems. Commonly observed issues such as low-frequency noise and the techniques proposed to reduce them are discussed.

In reverse time migration (RTM), the full acoustic wave equation is solved for wavefield propagation. Reverse time migration (RTM) solves the two-way acoustic wave equation, by the propagation in time domain of the source wavefield in forward direction (Section 2.1.1), and of the receiver wavefield in backward direction (Section 2.1.2). The scalar field (See 1.1) is obtained by a mathematical relationship between the extrapolated source and receiver wavefields summed over the sources or so many others, it is known in geophysics as imaging condition and the commonly used is the zero-lag cross-correlation (ZL-CC-IC). In section 2.3 we describe different imaging conditions used in reverse time migration and their effects in the final model.

RTM becomes more relevant in the exploration of hydrocarbons as the configuration of the geological structures have more challenges such as structures with steep dips, which are limiting for migration algorithms based on one-way wave equations. Moreover, many complex structures has often strong lateral velocity variations limiting the effectiveness of ray-based methods such as Kirchhoff migration. Reverse time migration is superior to other imaging methods in complex structures [1], besides, it had its appearance in the $80s$ [2, 3, 4] but due to its high computational cost it has only been applied recently. Advances in high performance computing technologies resulted in renewed attention from the seismic community to these techniques. Different works have been developed to improve the computational performance of RTM algorithm but it is not the focus of this thesis [5, 6, 7, 8].
There are a variety of migration algorithms, which can be classified by their output domain in time migration or depth migration, and pre-stack migration or post-stack migration.

Depth migration strives for fidelity both laterally and vertically, whereas time migration leaves the vertical direction in traveltime units. Depth migration requires a detailed field of propagation velocities within the Earth, while time migration needs only an average, or root-mean-squared (rms) velocity structure. Given the right velocity field, depth migration can produce superior models, but time migration is less sensitive to velocity error [9].

Post-stack migration assumes that the section built of stacked seismic signals recorded on the surface (traces), is equivalent to a zero-offset section. Meaning each trace is made as if the source and receiver are coincident. The advantages of post-stack migration derived from stacking are compression of data, removal of multiples and other noise, and fast, inexpensive processing. Post-stack migration holds up even in fairly strong lateral velocity variation, but at some level of velocity variation, stacking breaks down and prestack processing is required. Prestack migration is done on unstacked traces. It is preferred when two or more events occur at the same time but with different stacking velocities. Prestack depth migration is advantageous when velocities in the overburden or the target are complex [10].

In this thesis, we are focused on pre-stack depth migration by RTM algorithm due to we need to obtain models of more complex areas associated with large, rapid changes in velocity such as low-velocity layers, structure below salt or gas, or structures with steeply dipping structures and overhangs.

In the depths where there are interests for seismic exploration, the subsurface is elastic solid. During tectonics, different forces possibly in different direction have been applied on the rocks. Therefore, the seismic properties of the rock may be different in different directions. This direction-dependent property is called anisotropy. Another important mechanism of anisotropy is fine layering [11]. When seismic wavelength is much larger than the scale of layers, the media behaves equivalently transversely isotropic even though each layer is isotropic. Wave propagation in anisotropic media is fundamentally different from that in isotropic media. In isotropic media, phase propagation direction is always the same as the energy propagation [12]. This fact does not hold in anisotropic media. In anisotropic media, for a given spatial location, waves propagating in different directions experience different resistance [13], thus they may travel at different velocity. As a result, the phase and energy travel in different directions. This causes significant difficulties in understanding both theoretical aspect of wave phenomenon and numerical algorithm designs. Because of these difficulties and the desired scope in this thesis, we initially implement the 2D reverse time migration on isotropic media and in future work we will extrapolate our results to anisotropic media.

In the following sections 2.1.1, 2.1.2, we describe the mathematical foundations of reverse time migration implemented by the author to obtain the source and receiver wavefields and the subsurface model. Later on the migrated model and the problem formulation will be presented.

2.1. Basic wave equations for 2D reverse time migration on isotropic media

To perform reverse time migration, the wave equation is solved via the Finite Difference Method (FDM), where the derivatives in time and space are approximated by central finite differences. Finite difference representations of derivatives are derived from Taylor series expansion.

2.1.1. Forward modeling of acoustic wave equation

Let

$$\frac{\partial^2 u(\mathbf{x},t)}{\partial t^2} = \rho(\mathbf{x})c(\mathbf{x})^2\left[\frac{\partial}{\partial x}\left(\frac{1}{\rho(\mathbf{x})}\frac{\partial u(\mathbf{x},t)}{\partial x}\right)+\frac{\partial}{\partial z}\left(\frac{1}{\rho(\mathbf{x})}\frac{\partial u(\mathbf{x},t)}{\partial z}\right)\right] \tag{2.1}$$

be the $2D$ variable-density acoustic wave equation, where $\mathbf{x} = (x, z)$ is location in the 2D space, $c(\mathbf{x})$ is the scalar wave propagation velocity field, $\rho(\mathbf{x})$ is the density of the medium, t is the time of wave propagation, and $u(\mathbf{x}, t)$ is the solution function of the acoustic wave equation, defined by

$$\begin{aligned} u : \mathbb{R}^3 &\rightarrow \mathbb{R} \\ (x,z,t) &\rightarrow u(x,z,t) \end{aligned} \tag{2.2}$$

Under assumptions of the medium is isotropic with constant density, then the $2D$ acoustic wave equation (2.1) is transformed in

$$\frac{\partial^2 u(\mathbf{x},t)}{\partial t^2} = c(\mathbf{x})^2 \left[\frac{\partial^2 u(\mathbf{x},t)}{\partial x^2} + \frac{\partial^2 u(\mathbf{x},t)}{\partial z^2}\right] = c(\mathbf{x})^2 \nabla^2 u(\mathbf{x},t) \tag{2.3}$$

where $\nabla^2 = \frac{\partial^2}{\partial x^2} + \frac{\partial^2}{\partial z^2}$ is the laplacian operator.

Because RTM is based on seismic modeling algorithms, it is desirable to use a highly accurate numerical modeling approach. In this thesis, the $2D$ acoustic wave equation (2.3) is solved via Finite difference method (FDM) replacing the second derivative in time by a second-order central difference form and the second derivative in space by a eight-order central difference form to get a highly accurate, numerically stable results at the same level of other schemes such as pseudospectral Fourier method for the spatial derivatives [14].
Let

$$\frac{\partial^2 u(\mathbf{x},t)}{\partial t^2} = c(\mathbf{x})^2 \left[\frac{\partial^2 u(\mathbf{x},t)}{\partial x^2} + \frac{\partial^2 u(\mathbf{x},t)}{\partial z^2}\right] + f(\mathbf{x},t) \tag{2.4}$$

be the $2D$ acoustic wave equation (2.3) with an additional term $f(\mathbf{x},t) = f(t)\delta(\mathbf{x} - \mathbf{x}_s)$. $f(t)$ is the source wavelet function located in $\mathbf{x}_s$ that represents the external source that disturbs the surface. Eq. (2.4) allows to obtain the source wavefield.
To develop a finite difference method, we need to introduce grid points. Let us assume that the spacing of the grid points in the x direction is uniformly spaced, and given by Δx. Likewise, the spacing of the points in the z direction is also is uniformly spaced, and given by Δz. It is not necessary that the grid size Δx and Δz be the same. The values of Δx and Δz depend on the conditions of stability and accuracy of the method. The spacing of points in t direction is also uniformly spaced, and given by Δt. The grid points are identified by an index i which increases in the positive x-direction, an index j, which increases in the positive z-direction, and an index n which increases in the positive t-direction. For stability reasons, the size of the time steps must decrease as the size of the grid cells decreases (See 2.9).

Let $u_{i,j}^n$ an approximation to $u(x_i, z_i, t_i)$ obtained from a finite difference scheme.
The approximation of the second time derivative by the second order centered difference is given by

$$\frac{\partial^2 u(x,z,t)}{\partial t^2} = \frac{u_{i,j}^{n+1} - 2u_{i,j}^n + u_{i,j}^{n-1}}{(\Delta t)^2} \tag{2.5}$$

Approximating the second spatial derivative by the eight order centered difference is given by

$$\begin{aligned}\frac{\partial^2 u}{\partial x^2} &= \frac{1}{(\Delta x)^2}\left(-\frac{1}{560}u_{i-4,j}^n + \frac{8}{315}u_{i-3,j}^n - \frac{1}{5}u_{i-2,j}^n + \frac{8}{5}u_{i-1,j}^n - \frac{205}{72}u_{i,j}^n\right. \\ &+ \left.\frac{8}{5}u_{i+1,j}^n - \frac{1}{5}u_{i+2,j}^n + \frac{8}{315}u_{i+3,j}^n - \frac{1}{560}u_{i+4,j}^n\right)\end{aligned} \tag{2.6}$$

$$\begin{aligned}\frac{\partial^2 u}{\partial z^2} &= \frac{1}{(\Delta z)^2}(-\tfrac{1}{560}u^n_{i,j-4} + \tfrac{8}{315}u^n_{i,j-3} - \tfrac{1}{5}u^n_{i,j-2} + \tfrac{8}{5}u^n_{i,j-1} - \tfrac{205}{72}u^n_{i,j} \\ &+ \tfrac{8}{5}u^n_{i,j+1} - \tfrac{1}{5}u^n_{i,j+2} + \tfrac{8}{315}u^n_{i,j+3} - \tfrac{1}{560}u^n_{i,j+4}) \end{aligned} \tag{2.7}$$

Replacing eq. (2.5), eq. (2.6) and eq. (2.7) in eq. (2.3), the acoustic wave equation can be written as

$$\begin{aligned}u^{n+1}_{i,j} &= 2u^{n-1}_{i,j} - u^n_{i,j} + \beta^2(-\tfrac{1}{560}u^n_{i-4,j} + \tfrac{8}{315}u^n_{i-3,j} - \tfrac{1}{5}u^n_{i-2,j} \\ &+ \tfrac{8}{5}u^n_{i-1,j} - \tfrac{205}{72}u^n_{i,j} + \tfrac{8}{5}u^n_{i+1,j} - \tfrac{1}{5}u^n_{i+2,j} + \tfrac{8}{315}u^n_{i+3,j} \\ &- \tfrac{1}{560}u^n_{i+4,j} - \tfrac{1}{560}u^n_{i,j-4} + \tfrac{8}{315}u^n_{i,j-3} - \tfrac{1}{5}u^n_{i,j-2} + \tfrac{8}{5}u^n_{i,j-1} \\ &- \tfrac{205}{72}u^n_{i,j} + \tfrac{8}{5}u^n_{i,j+1} - \tfrac{1}{5}u^n_{i,j+2} + \tfrac{8}{315}u^n_{i,j+3} \\ &- \tfrac{1}{560}u^n_{i,j+4}) + f(x,z,t) \end{aligned} \tag{2.8}$$

where $\beta = \dfrac{c(x,z)\Delta t}{\Delta h}$ and $\Delta x = \Delta z = \Delta h$, where Δh is the grid spacing of finite difference mesh for an uniform grid. The stability condition for the finite difference scheme is given by [15]

$$\frac{c\Delta t}{\Delta h} \leq \frac{\sqrt{a_1}}{\sqrt{a_2 m}} \tag{2.9}$$

where Δt is the temporal sample interval, a_1 is the sum of absolute values of temporal weights for derivatives, a_2, the sum of absolute values of spatial weights for derivatives, and m is the dimension of domain.
Furthermore,

$$\Delta h = \frac{c}{10 f_c} \tag{2.10}$$

where f_c is the central frequency of the source wavelet function
The stability condition for the finite difference scheme of second order in time and eighth order in space is

$$\frac{c\Delta t}{\Delta h} \leq \frac{3}{32}\sqrt{35} \tag{2.11}$$

The values of Δh and Δt depend of minimum and maximum values of the velocity in the media and the frequency of the source wavelet function.

Source function term

We consider a source function term $f(\mathbf{x}, t) = f(t)\delta(\mathbf{x} - \mathbf{x}_s)$ in the form of a Ricker pulse such that $f(t)$ is as follows

$$\begin{aligned} f : \mathbb{R} &\rightarrow \mathbb{R} \\ t &\rightarrow f(t) \end{aligned} \tag{2.12}$$

and given by

$$f(t) = \left(1 - (2\pi f_c \tau)^2\right) e^{-(\pi f_c \tau)^2} \tag{2.13}$$

where f_c is the central frequency of the pulse, t is the time and τ is the time parameter used to define the start of the active phase. In this thesis, $f_c = 40\ Hz$ and $\tau = t - 0.05$. We chose a central frequency of 40 Hz due to computational limitations. The value of Δt decreases as the value of Δh while the value of f_c increases, according to the Courant condition in eq. 2.9. This behavior causes that the number of wavefields to be recorded, are increased considerably reducing rapidly the storage capacity. The Ricker pulse is depicted in Figure 2.1

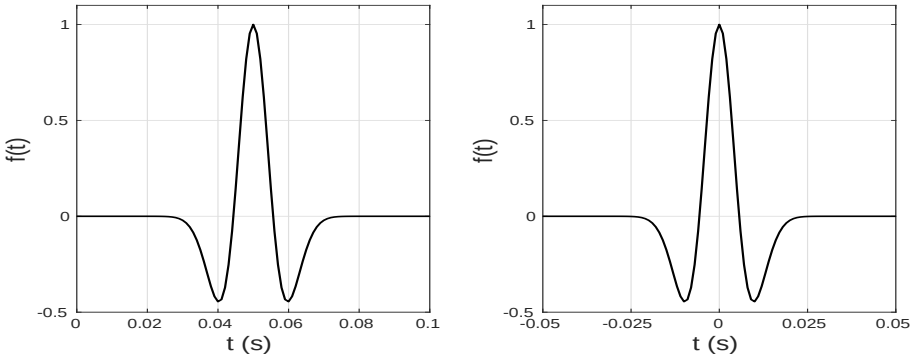

Figure 2.1: Ricker pulse with $f_c = 40$ Hz and $\tau = t - 0.05$ (Left) and $\tau = t$ (Right)

2.1.2. Backward modeling of acoustic wave equation

Backward modeling of the 2D acoustic wave equation can be performed by backward extrapolating the seismic signals recorded at the surface.

Let

$$\frac{\partial^2 u(\mathbf{x},\tau)}{\partial \tau^2} = c(\mathbf{x})^2 \left[\frac{\partial^2 u(\mathbf{x},\tau)}{\partial x^2} + \frac{\partial^2 u(\mathbf{x},\tau)}{\partial z^2}\right] + \sum_{\mathbf{x}_g} D(\mathbf{x}_g,\tau) \tag{2.14}$$

be the $2D$ acoustic wave equation (2.3) with an additional term $\sum_{\mathbf{x}_g} D(\mathbf{x}_g,\tau)$, where $D(\mathbf{x}_g,\tau)$ is the seismic signal recorded on the surface at position $\mathbf{x}_g$, $\tau = T - t$ and T is the total observation time.

Then, using the same finite difference scheme shown above, the receiver wavefield can be approximated by

$$
\begin{aligned}
u_{i,j}^{n+1} &= 2u_{i,j}^{n-1} - u_{i,j}^{n} + \beta^2(-\tfrac{1}{560}u_{i-4,j}^{n} + \tfrac{8}{315}u_{i-3,j}^{n} - \tfrac{1}{5}u_{i-2,j}^{n} \\
&+ \tfrac{8}{5}u_{i-1,j}^{n} - \tfrac{205}{72}u_{i,j}^{n} + \tfrac{8}{5}u_{i+1,j}^{n} - \tfrac{1}{5}u_{i+2,j}^{n} + \tfrac{8}{315}u_{i+3,j}^{n} \\
&- \tfrac{1}{560}u_{i+4,j}^{n} - \tfrac{1}{560}u_{i,j-4}^{n} + \tfrac{8}{315}u_{i,j-3}^{n} - \tfrac{1}{5}u_{i,j-2}^{n} + \tfrac{8}{5}u_{i,j-1}^{n} \\
&- \tfrac{205}{72}u_{i,j}^{n} + \tfrac{8}{5}u_{i,j+1}^{n} - \tfrac{1}{5}u_{i,j+2}^{n} + \tfrac{8}{315}u_{i,j+3}^{n} \\
&- \tfrac{1}{560}u_{i,j+4}^{n}) + D(x,z,\tau) \qquad (2.15)
\end{aligned}
$$

where $\beta = \dfrac{c(x,z)\Delta t}{\Delta h}$, $\Delta x = \Delta z = \Delta h$, and the stability condition is the same shown in eq. (2.9), eq. (2.10) and eq. (2.11).

2.1.3. Non-reflecting boundary conditions

The wave propagation problems are normally solved for an infinite medium, but the finite-difference solution can only be obtained at a finite number of points; thus it is necessary to introduce boundaries to obtain a finite model. The introduction of these unwanted boundaries in the models used cause waves to be reflected from the boundaries whereas, in the actual physical process of interest, waves pass through these boundaries with no reflection. This boundary reflection phenomenon which occurs in models is due to the use of Dirichlet or Neumann boundary data along the unwanted boundaries. Since the use of these boundaries cannot be avoided in finite-difference generation of synthetic seismograms, we should seek boundary conditions which reduce edge reflection [16].

We use a modified version of non-reflecting boundary conditions described on [17]:

Let $u_{i,j}^{n}$ denote the displacement at time $t = n\Delta t$ and at spatial location $x = i\Delta x$, $z = j\Delta z$, $i = 1, \dots N_x$, $j = 1, \dots N_z$, where Δt denotes the time step size, Δx and Δz denote the mesh size in the $x-$ and $z-$ directions, and N_x, N_z denote the total points in the grid in the $x-$ and $z-$ directions.

For the non-reflecting boundary condition the values of $u_{i,j}^{n}$ obtained by eq. (2.8) or eq. (2.15) are slightly reduced after each time step in a strip of nodes surrounding the numerical mesh. The value of $u_{i,j}^{n}$ is gradually reduced by multiplying it by a factor G that depends of position of the strip. For example, for the strip on the left the factor G is calculated by $G = e^{-[\alpha(m-i)]^2}$, where m is the number of nodes in the strip and α is an arbitrary absorbing factor. In our simulations we used $m = 40$ and $\alpha = 0.008$ because the amplitude of the wavefield decreases until it tends to zero close to final of the strip in each boundary.

2.2. Migrated model

After both source and receiver wavefields have been extrapolated, the scalar field can be obtained by using an imaging condition.

The final model has been conventionally obtained by the zero lag cross-correlation [18] by examining the double summation of products of seismic amplitudes between the source and the receiver wavefields. One of them, summed in time domain and

the other one, summed in the source domain (Zero-lag cross-correlation imaging condition (ZL-CC-IC)).

The source wavefield $S(\mathbf{x}, t)$ is the image of the map

$$\begin{aligned} u : \mathbb{R}^3 &\rightarrow \mathbb{R} \\ (x, z, t) &\rightarrow u(x, z, t) \end{aligned}$$

where u is a solution function of the acoustic wave equation (2.4) and given by eq. (2.8) with an initial condition, that is the source function, given by the map

$$\begin{aligned} f : \mathbb{R} &\rightarrow \mathbb{R} \\ t &\rightarrow f(t). \end{aligned}$$

And, the receiver wavefield $R(\mathbf{x}, t)$ is the image of the map

$$\begin{aligned} u : \mathbb{R}^3 &\rightarrow \mathbb{R} \\ (x, z, t) &\rightarrow u(x, z, t) \end{aligned}$$

where u is a solution function of the acoustic wave equation (2.14) and given by eq. (2.15) with an initial condition from the seismic signals recorded on the surface.

In 1971, Claerbout defined the reflective imaging condition as the dimensionless ratio between the upgoing wavefield (Reflected) and the downgoing wavefield (Source) in the time of first arrival. This imaging condition is defined as follows [18].

$$I(x, y, z; s_j) = \frac{R(x, y, z; t_i; s_j)}{S(x, y, z; t_i; s_j)} \tag{2.16}$$

where I, R, and S represent the migrated model, the receiver wavefield and the source wavefield, respectively, for a particular source s_j, in the time t_i, in a grid location (x, y, z).

Due to the ratio given by expression (2.16) can be unstable (Division for very small values) away from the reflectors, Claerbout derived an approximation to the imaging condition (2.16) through a zero lag cross correlation operator given by eq. 2.17, where gives the product of wavefields R and S summed over all times i for each source, and then summed over all sources j, to produce at the end a stack migrated model. s_{max} is the maximum number of sources in data set, and t_{max} is the maximum number of time steps used in the propagation. This imaging condition is often used and is easy to implement [1]. Next section will extend this idea.

2.3. Uncertainty in reverse time migration models

Uncertainties in RTM appear mostly because of the superposition of extrapolated source an receiver wavefields and by applying the ZL-CC-IC proposed by Claerbout [18]. It has been demonstrated that the ZL-CC-IC is computationally more simple to implement and favorable than another mathematical expression used to obtain the final model.

Then, the zero-lag cross-correlation imaging condition is given by

$$I(\mathbf{x}) = \sum_{j=1}^{s_{max}} \sum_{i=1}^{t_{max}} S(\mathbf{x}; t_i; s_j) R(\mathbf{x}; t_i; s_j) \tag{2.17}$$

where $\mathbf{x} = (x, z)$ is the location in the Cartesian coordinate system, $S(\mathbf{x}; t_i; s_j)$ and $R(\mathbf{x}; t_i; s_j)$ are the source and receiver wavefields, respectively, t_{max} is the total time, s_{max} is the total number of sources, and I is the final RTM model.
It produces kinematically correct images of the geometry of the subsurface structure [19]. The final model is kinematically accurate at the reflectors due to the fact that incident and reflected wavefields are coincident in space and time [1], but the migrated amplitudes no longer hold any physical meaning.

However, the final model is contaminated with low spatial frequency uncertainties which can affect its interpretation. These low spatial frequency uncertainties are common in RTM and are called artifacts. The reasons why these artifacts appear are described in section 2.3.

2.3.1. Low spatial frequency noises: Artifacts

Several implementations of RTM using the cross-correlation imaging condition given by eq. (2.17) has been reported by [2, 20, 21, 22], among others.

However, this imaging condition often produces a significant amount of strong amplitudes, low-frequency noise that contaminates the model. This low-frequency noise (Artifacts) appears due to presence of singularities in the velocity field (Strong velocity contrasts) and the unwanted cross-correlation of source and receiver wavefields in non-reflective points along the ray paths. In presence of singularities in the velocity field, strong amplitude changes occur and the appearance of artifacts is greater than in smooth velocity changes [23]. Correlation of diving waves, head waves and backscattered waves appear as low-frequency noise (Artifacts) which can hide important details in the model [24].

This type of uncertainties is unique in reverse time migration: They are not present in one-way equation-based migration models constructed using the same cross-correlation imaging condition.
In order to show how the uncertainties are generated in RTM models, we will consider some wave paths that come from a source located on the surface of a subsurface structure depicted in Figure 2.2:

When the source disturbs the surface, the wave is forward propagated and it travels into the ground starting at a source location. The energy of the wave is partitioned into two parts when it find an interface. One part of the energy is reflected back to the surface and the other part is transmitted through the interface and continues to propagate in the medium. In Figure 2.2 these wave paths are marked as IW (incident wave), TW (transmitted wave) and RW (reflected wave) and it corresponds to the natural path of the wave (black lines). In addition, when the seismic signals are back propagated into the ground, the waves have the same behavior as the forward propagation when interacting with the subsurface structures. Due to this,

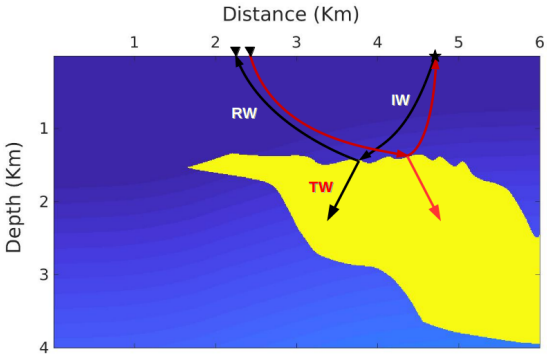

Figure 2.2: Some wavepaths for a single source and one receiver on the surface

in RTM the forward and backward propagation have similar paths of the wave that are correlated. The cross-correlation of the wavefields obtained by 2.8 and 2.15 will not only generate amplitude in the reflection points, but also in the non-reflecting points along the path of the wave, causing uncertainties in the model that are low spatial frequency.

Different methods have been proposed to eliminate or reduce the artifacts in the models. These methods can be classified in three categories [25]:

1. Wavefield propagation approaches, where the wave equation is modified to attenuate reflections at the boundaries.

2. Imaging condition approaches, where only the energy created by reflections is kept in the final model.

3. Post-imaging condition approaches, where the artifacts are filtered after imaging on each shot or the stacked model.

Some of these methods, which are applied in both frequency domain and time domain, are described chronologically as follows in section 2.3.2 in order to present the state of the art on the topic.

In this thesis, we are focused on imaging conditions in time domain because of the RTM algorithm used to obtain the models is applied in the same domain and the computational cost is reduced due to the wavefields are not transformed to another domain. Also, will be focused on the RTM improvement via trace analysis on the wavefields.

2.3.2. On the imaging condition developments

Several works have been developed around to attenuate these low-frequency artifacts, preserving the reflections, and improving the model quality, implementing other strategies such as modifications of the wave equation [23, 26], proposing

other imaging conditions [1, 25, 27, 28, 29, 30] and using image filtering techniques [21, 22]. Some of these methods are briefly described below.

In RTM, the reflections at interfaces can be suppressed by matching the impedance of the medium both sides of an interface, resulting in the non-reflective wave equation [26]. Loewenthal et al., in 1987 [23], showed an alternative method to achieve the same purpose of suppressing the reflections, even for a constant density model based on the smoothing slowness field over the medium. However, both approaches showed less effectiveness in the prestack cases because the reflections can occur at non-zero incident angles at a velocity interface when the impedances are the same ([1]).

In 2001, Youn et al. [21] processed each cross correlation frame for an individual source recorded through a Laplacian model reconstruction of the form:

$$I_{lp}(x,y,z) = \left(\frac{\partial^2 I_{cc}}{\partial x^2} + \frac{\partial^2 I_{cc}}{\partial y^2} + \frac{\partial^2 I_{cc}}{\partial z^2} \right) \tag{2.18}$$

where $I_{lp}(x,y,z)$ is the reconstructed image frame for a source recorded and I_{cc} is the model obtained by cross-correlation between the forward wavefield (source wavefield) S and backward wavefield R (Receiver wavefield), determined by eq. 2.17

Valenciano and Biondi [27] proposed an imaging condition based on the principle of image of Claerbout and it consisted of deconvolution of the receiver wavefield with the source wavefield in two dimensions. The $2D$ deconvolution is expressed as:

$$I(x,z) = \sum_{k_{x_s}} \sum_{\omega} \frac{\tilde{R}(x,z,\omega,k_{x_s})\tilde{S}^*(x,z,\omega,k_{x_s})}{\tilde{S}(x,z,\omega,k_{x_s})\tilde{S}^*(x,z,\omega,k_{x_s}) + \varepsilon^2(x,z)} \tag{2.19}$$

where $I(x,z)$ is the zero offset of the $2D$ deconvolution calculated as the sum over the temporal frequency (ω) and frequency of source position (k_{x_s}). $\tilde{R}(x,z,\omega,k_{x_s})$ and $\tilde{S}(x,z,\omega,k_{x_s})$ are the $2D$ Fourier transforms of the receiver and source wavefields, respectively. $\varepsilon(x,z)$ is variable but constant in (x_s,t) plane and is calculated as:

$$\varepsilon^2(x,z) = \lambda \langle \tilde{R}(x,z,\omega,k_{x_s})\tilde{S}^*(x,z,\omega,k_{x_s}) \rangle \tag{2.20}$$

where $\langle\rangle$ means the mean and λ is a parameter of stabilization between $0 < \lambda < 1$ [31]. This imaging condition is applied in the frequency domain, using migration methods based on one way wave equations.

In 2005, Fletcher et al. [32] proposed to remove unwanted reflections during the wave propagation by applying a directional damping term in the non-reflective wave equation in areas of the velocity field where unwanted reflections occur.

Yoon and Marfurt [33] proposed to use the Poynting vector to improve the cross correlation imaging condition. Calculating the direction of wave propagation from the Poynting vector results in a new image condition. From

$$I = \frac{\sum_t P_s(t) P_g(t)}{\sum_t [P_s(t)]^2} \tag{2.21}$$

2

where $P_s(t)$ and $P_g(t)$ are the pressures in the source and receiver wavefields, respectively, and establishing a table of weights $W(\cos\theta)$ depending on the opening angle between the correlated waves determined by

$$\cos\theta = \frac{\mathbf{v}_s(t)P_s(t) \cdot \mathbf{v}_g(t)P_g(t)}{|\mathbf{v}_s(t)P_s(t)||\mathbf{v}_g(t)P_g(t)|} \tag{2.22}$$

model where v_s and v_g are the director vectors of source and receiver ray paths, respectively, the new imaging condition is given by

$$I = \frac{\sum_t [P_s(t)P_g(t)W(\cos\theta)]}{\sum_t [P_s(t)]^2} \tag{2.23}$$

Kaelin y Guitton in 2006 [28], implemented for big impedance contrasts and complex geological structures an improved imaging condition dividing the cross correlation imaging condition by the "receiver illumination", whose expression is given by

$$I(x,z) = \sum_s \frac{\sum_t S(x,z,t)R(x,z,t)}{R^2(x,z,t)} \tag{2.24}$$

This implementation eliminates artifacts and preserves reflectors at the same time. Normalization by receiver illumination reduces artifacts throughout the image very effectively and preserves the lowest reflections ([28]). But, in most cases this imaging condition requires to be applied regularization in the denominator to avoid division by zero.
Guitton et al[22] tried to remove the artifacts using a least squares filtering with prediction error filters after the imaging condition and they used an inversion process that preserves the phase and the signal integrity while most of the artifacts are attenuated.

One year later, Guitton et al. [25] showed a method to improve the deconvolution imaging condition raised in the eq. (2.19) approaching the division of receiver wavefield by the source wavefield. This approach consisted in smoothing the denominator, as opposed to adding a stabilization parameter. The idea was to fill the values at zero of $\mathbf{S}(\omega,\mathbf{x},\mathbf{x_s})\mathbf{S}'(\omega,\mathbf{x},\mathbf{x_s})$ (Product of the 2D Fourier transform of the source wavefield and its complex conjugated) with the value of neighboring points, opposed to using an arbitrary constant as in the eq. (2.19). This condition is given by:

$$\mathbf{I_s}(\mathbf{x}) = \sum_{\mathbf{x_s}} \sum_{\omega} \frac{\tilde{\mathbf{R}}(\omega,\mathbf{x},\mathbf{x_s})\tilde{\mathbf{S}}'(\omega,\mathbf{x},\mathbf{x_s})}{\langle \tilde{\mathbf{S}}(\omega,\mathbf{x},\mathbf{x_s})\tilde{\mathbf{S}}'(\omega,\mathbf{x},\mathbf{x_s})\rangle_{(x,y,z)}} \tag{2.25}$$

where $\langle . \rangle_{(x,y,z)}$ represents the smoothing in the image space in the x, y, and z directions ans x_s is the position of each source.
Vivas et al [34] compared four techniques used to avoid instability of the division of the downgoing wavefield in the condition of image used in one-way wave equations migration, showing the advantages and disadvantages of each of them through numerical experiments. In addition, within the numerical examples, they presented a new approach that avoids the problem of instability in the deconvolution imaging condition type, achieving noise-free images, preserving amplitudes of the reflection coefficients. These stabilization techniques were implemented in the frequency domain and using the true amplitude shot-profile migration method.

Similarly, Schleicher et al. (2008, [31]), realized a comparison between deconvolution imaging condition images and studied the impact of these conditions on improving migration artifacts and quality of amplitudes at different deep reflectors. Chattopadhyay and McMechan (2008,[19]), analyzed three kinds of imaging conditions and compared image amplitudes extracted with reflector coefficient for the model used. Their aim was to analyze the reflector coefficient amplitudes obtained using different imaging conditions in reverse time migration to identify which of those had an acceptable approximation for the subsequent development of true amplitude reverse time migration.

Based on the results of Haney et al. (2005, [35]), Costa et al. (2009, [36]) proposed a new imaging condition in RTM. The idea was to propose a obliquity-correction factor introducing a dip-dependent weight function in the source illumination imaging condition to compensate for the reflector dip effect on amplitudes of RTM. They combined obliquity factor weight W with the illumination compensation of the imaging condition and is described as

$$I(\mathbf{x}) = \int_{\mathbf{x}_s} \frac{\int_{\mathbf{x}_g} \int_0^{t_{max}} W(\mathbf{S}_s, \mathbf{S}_g) p_s(\mathbf{x}, t; \mathbf{x}_s) p_g(\mathbf{x}, t; \mathbf{x}_g) dt d\mathbf{x}_g}{\int_0^{t_{max}} p_s(\mathbf{x}, t; \mathbf{x}_s) p_s(\mathbf{x}, t; \mathbf{x}_s)} d\mathbf{x}_s \tag{2.26}$$

Through numerical experiments they showed that obliquity correction strongly reduces the artifacts after illumination compensation (Source illumination). But the image produced with this imaging condition presents fewer artifacts than previous imaging condition and does not completely eliminate the backscattering.

Fei et al. [37] developed a RTM de-blending technique which separates upgoing and downgoing source and receiver wavefields and used them to construct final RTM images. They demonstrated that the de-blended RTM is less velocity-sensitive compared to conventional RTM. The de-blending RTM provides high fidelity images for complex salt structures without artifacts while preserving steeply dipping reflectors and overturned structures where one-way wave equation extrapolation methods may become inadequate.

Liu et al. (2011, [1]) proposed a new imaging condition using the decomposition of full wavefield in their unidirectional components along some specific direction and applying it to the combinations of opposite direction to the decomposed wavefields. This new imaging condition is given by:

$$I_{ud}(\vec{x}) = \int_0^{T_{max}} [s_d(t,\vec{x}) r_u(t,\vec{x}) + s_u(t,\vec{x}) r_d(t,\vec{x})] dt \tag{2.27}$$

where $s_d(t,\vec{x})$, $s_u(t,\vec{x})$, $r_d(t,\vec{x})$, $r_u(t,\vec{x})$ are the components of the downward and upward wave of source and receiver wavefields, respectively. The upward and downward wavefields are decomposed and calculated in the frequency-wavenumber domain $(f-k)$ (Hu and McMechan, 1987, [38]).

Cogan et al. [39] addressed different strategies of normalization of RTM images and introduced a new hybrid normalization scheme. They demonstrated the impact of the various RTM normalization schemes in the noise and the characteristics of the final image.

Whitmore et al., (2012, [40]), demonstrated that by applying an inverse scattering imaging condition, it reduced significantly artifacts in the image and preserved the true reflection data. This imaging condition attenuates the backscattered waves using a combination of two separate images: one based on the product of the time derivatives of the incident and reflected wavefields and the other based on the product of the spatial gradients of the incident and reflected wavefields. This imaging condition is given by [40], [30]:

$$I_{IS}(x,z) = \sum_{t=0}^{T_{max}} \left[\nabla S(x,z,t) \cdot \nabla R(x,z,t) - \frac{1}{v(x,z)^2} \frac{\partial S(x,z,t)}{\partial t} \frac{\partial R(x,z,t)}{\partial t} \right] \tag{2.28}$$

where $S(x,z,t)$ and $R(x,z,t)$ are the source and receiver wavefields, respectively, and $v(x,z)$, is the velocity field.

In 2013, Nguyen and McMechan [41], used the excitation amplitude imaging condition as a stable, robust and efficient alternative to cross-correlation imaging condition. This imaging condition is obtained dividing the receiver wavefield R for the maximum amplitude of source wavefield (S_{max}) only at points where images are created, thus obtaining high-resolution migrations, with a fraction of the usual cost of traditional implementations. In terms of the amplitude of excitation S_{max}, eq. (2.16) can be written as follows

$$I(x,y,z;s_j) = \frac{R(x,y,z;t_i;s_j)}{S_{max}(x,y,z;t_i;s_j)} \tag{2.29}$$

where $t_i = t_i(x,y,z)$ is the corresponding time step arrangement of excitation for source s_j. This division is made only at points where the image is created at the time t_i. This condition scales the amplitudes of the receiver wavefield by the maximum amplitude of the source wavefield at that location, generating that the R and S wavefields are accurate to have been corrected for all propagation effects. The main limitation of the excitation amplitude approach is that it includes only one (the maximum) incident amplitude per source at each image point, and so gives lower stacked amplitudes where there are multipath contributions that are not included [41].

Arnsted et al (2013, [42]) from the cross correlation imaging condition de Claerbout (1971, [18]), made a modification that produced common-angle gathers with correct estimates of the amplitude versus angle relationships. The method modifies the initial wavefield in the downward propagation and decomposes into plane waves in the midpoint-slowness domain. This new modification avoids instabilities associated with the division of wavefields.

Qin and McGarry (2013, [43]), proposed an approach to generate the true-amplitude RTM common-shot image by incorporating the directional fold correction into the receiver wavefield. They combined the source-illumination-normalized cross-correlation imaging condition with the directional fold correction factor. This imaging condition is given by:

$$I(\mathbf{x}) = \frac{\int R_U(\mathbf{x};\omega) S_D^*(\mathbf{x};\omega)}{\int S_D(\mathbf{x};\omega) S_D^*(\mathbf{x};\omega) + \epsilon} \tag{2.30}$$

where ϵ is a damping parameter to avoid numerical instability issues when the denominator is too small. $S_D(\mathbf{x};\omega)$ is the source wavefield and $R_U(\mathbf{x};\omega)$ is the receiver wavefield denoted by

$$R_U(\mathbf{x};\omega) = \int D(\mathbf{x}_r;\omega) G^*(\mathbf{x}_r,\mathbf{x};\omega) \frac{i\omega\cos(\alpha_{r0})}{v_r} d^2\mathbf{x}_r \tag{2.31}$$

where $G^*(\mathbf{x}_r,\mathbf{x};\omega)$ is the complex conjugate of the Green function between receiver $\mathbf{x}_r$ and the image point $\mathbf{x}$; v_r is the wave speed at the receiver location, $\frac{\cos(\alpha_{r0})}{v_r}$ is the directional fold correction and D is the signals recorded on the surface in the frequency domain. The image quality at shallow depths can be significantly improved.

Chen and He (2014, [44]) used the Poynting vector of the acoustic wave equation to the separate the wavefields in the up-going, down-going, left-going, and right-going waves and applied the normalized wavefield separation cross-correlation imaging condition to suppress the low-frequency noise and improve the imaging precision. The normalized wavefield separation cross-correlation imaging condition is given by

$$\begin{aligned} I(x,z) &= \frac{\sum_t S_u(x,z,t) R_d(x,z,t) + \sum_t S_d(x,z,t) R_u(x,z,t)}{\sum_t S^2(x,z,t)} \\ &+ \frac{\sum_t S_l(x,z,t) R_r(x,z,t) + \sum_t S_r(x,z,t) R_l(x,z,t)}{\sum_t S^2(x,z,t)} \end{aligned} \tag{2.32}$$

where $S_u(x,z,t)$ and $R_u(x,z,t)$ are the up-going wavefields of sources and receivers, respectively, $S_d(x,z,t)$ and $R_d(x,z,t)$ are the down-going wavefields of sources and receivers, $S_l(x,z,t)$ and $R_l(x,z,t)$ are left-going wavefields of sources and receivers, and $S_r(x,z,t)$ and $R_r(x,z,t)$ are the right-going wavefields of sources and receivers, respectively.

In 2014, Pestana and Dos Santos [29], showed that the reverse time migration images produced by impedance sensitivity kernel imaging condition can significantly reduce the low spatial frequency artifacts and preserve reflections.

Based on the work of Whitmore and Crawley (2012, [40]), they proposed the impedance sensitivity kernel imaging condition given by:

$$\begin{aligned} I_k(x,z) &= \frac{1}{v^2(x,z)} \int \frac{\partial}{\partial t} S(x,z,t) \frac{\partial}{\partial t} R(\mathbf{x},t) dt \\ &+ \int \nabla S(x,z,t) \cdot \nabla R(x,z,t) dt \end{aligned} \tag{2.33}$$

where $S(x,z,t)$ and $R(x,z,t)$ are the source (forward) and receiver (backward) wavefields, respectively, and $v(x,z)$ is the velocity field. This imaging condition separated by the Poynting vector achieves cleaner results and low contamination of low-frequency noises. They demonstrated that the RTM images obtained with the impedance sensitivity kernel for the downgoing wavefield separated using the Poynting vector can preserve the reflections and attenuated the low frequency artifacts.

Ren et al. (2015, [45]) proposed a new imaging condition following the steps developed by Yoon (2006,[33]) and Lui et al. (2011, [1]). They combine the Poynting vector imaging condition and the wavefield decomposition imaging condition. This new imaging condition is given by

$$I(\mathbf{x}) = \int_0^{T_{max}} (S_{z+}(\mathbf{x},t) R_{z-}(\mathbf{x},t) + S_{z-}(\mathbf{x},t) R_{z+}(\mathbf{x},t)) W(\cos\theta) dt \tag{2.34}$$

where the weight $W(\cos\theta)$ is expressed as

$$W(\cos\theta) = \begin{cases} 1 & \cos\theta \geq \gamma, \gamma \in [-1,1] \\ 0 & else \end{cases} \tag{2.35}$$

where γ is a truncation parameter, by which some correlation is muted, $S_{z+}(\mathbf{x},t)$, $R_{z+}(\mathbf{x},t)$ are the upgoing components of source and receiver wavefields and $S_{z-}(\mathbf{x},t)$, $R_{z-}(\mathbf{x},t)$ are the downgoing components of source and receiver wavefields, respectively. The proposed imaging condition can effectively remove artifacts by muting these correlations based on the directions of incident and reflect wave propagating.

Shen and Albertin (2015, [46]) showed an algorithm that explicitly separates a wavefield into upgoing and downgoing components. They used the Hilbert transform in time that generates the imaginary part of the analytical signal that corresponds to the positive or negative temporal frequency component of the wavefield. With this Hilbert transform the source and receiver wavefield can be separate in their components. To do this, it needs to solve the wave equation twice: once for the source and another for the Hilbert transform of the source. In addition, they used the causal imaging condition to remove certain imaging artifacts in the stacks as well as in the image gathers.

Wang et al. (2016, [47]), presented a new optical imaging technique based on RTM for reconstructing optical structures in homogeneous media and developed

new methods to suppress the artifacts and to refine the image quality. The optical RTM reconstructs the image by modeling the wave propagation with both forward modeling and reverse-time extrapolation using Maxwell's equations in optics instead of elastodynamic equations in seismic. They compared the Laplacian filtering, illumination normalization, and the ratio method with a new derivative-based and power-image methods and it was used in biomedical applications.

Wang and Liu (2016, [48]) used the one-step low-rank extrapolation method and wavefield decomposition imaging condition ([1, 49]). The one-step extrapolation method allows very large time step to be used. In addition, due to the wavefield is analytical, the wavefield decomposition can be performed at each time level, avoiding the Fourier transformation in the time domain. The final migration result was nearly noise-free and the salt structure was well imaged.

Wang and Xu (2016, [50]) proposed an algorithm to perform wavefield decomposition in the time-space domain via the Hilbert transform. This algorithm consists in a limited-length convolution operator of the Hilbert transform in time-space domain and it can achieve the same goal of improving the RTM quality but with significant reduction of computation time. The proposed wavefield decomposition algorithm can effectively remove the imaging artifacts and improve the quality of RTM images and angle gathers.

The main contribution of this thesis will be developed in Chapters 3, 4 and 5 challenging the previous presented approaches in depth and time. As follows, a numerical examples section will illustrate the former equations of this Chapter and enlighten the reader on the uncertainty magnitude on simple and complex structures of subsurface.

2.4. RTM application in synthetic datasets

In order to illustrate basically the RTM algorithm, taking into account the concepts given in sections 2.1.1, 2.1.2, 2.1.3, and using the conventional imaging condition in section 2.3.2, we will apply it in the two-layer model and the $2D$ SEG-EAGE salt model .

Two-layer model

We consider a synthetic two-layer wave propagation velocity field with a horizontal distance of 3.0 Km and a vertical distance of 1.5 Km as shown in Figure 2.3a). The velocity of the top layer is $3\ \frac{Km}{s}$ and in the bottom layer is $5\ \frac{Km}{s}$.

We used 39 source points located along the surface. The first source is located on the surface at $x = 0.075$ Km and the last one at $x = 2.9175$ Km from the origin; the source interval is 75 m; each source contains 400 receivers equally spaced and distributed along the surface beginning at $x = 7.5$ m from the origin and the receiver interval is 7.5 m. Each source disturbs the medium separately and the 400 receivers register the seismic signals due to the reflections of the waves in the subsurface (Figure 2.3b)).

Figure 2.4 shows some snapshots of the data volume representing the source wavefield obtained by eq. (2.8). The wavefield was obtained with a source located at

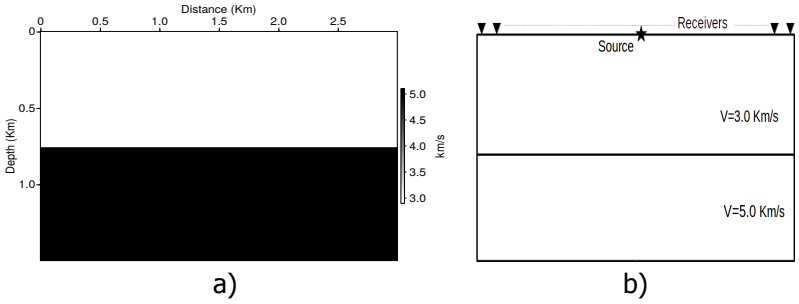

Figure 2.3: a) Synthetic two-layer velocity field b) Survey geometry for the source at $x = 1.5$ Km (bottom)

$x = 1.5$ Km on the surface. The snapshots correspond to the times 80, 140, 210, 270, 340, 400, 460 and 510 milliseconds. The total propagation time of the wave was 1.2 seconds. We can note the wavefront propagation from the origin of the source on the surface for specific times.

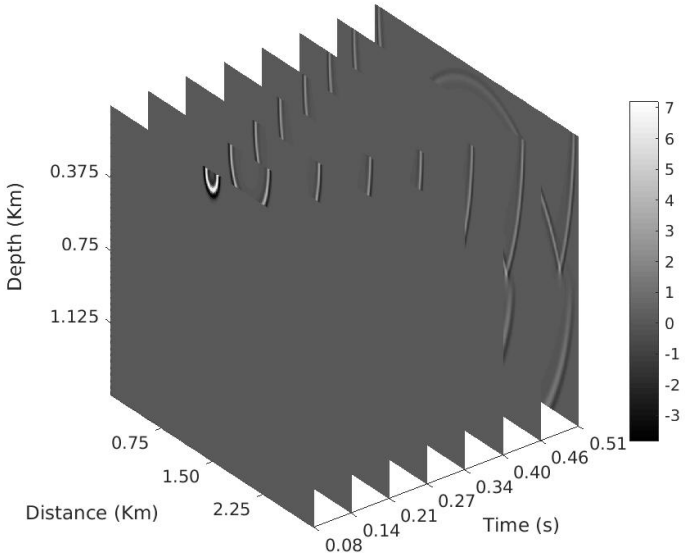

Figure 2.4: Snapshots of the source wavefield for a source located at $x = 1.5$ Km on the surface

The receiver wavefield is obtained by eq. (2.15) and using the seismic signal (Seismogram) recorded on the surface. Figure 2.5 shows the seismic signals recorded on the surface due to the forward propagation with a source located at $x = 1.5$ Km on the surface and a seismic trace from a receiver located at $x = 1.7$ Km.

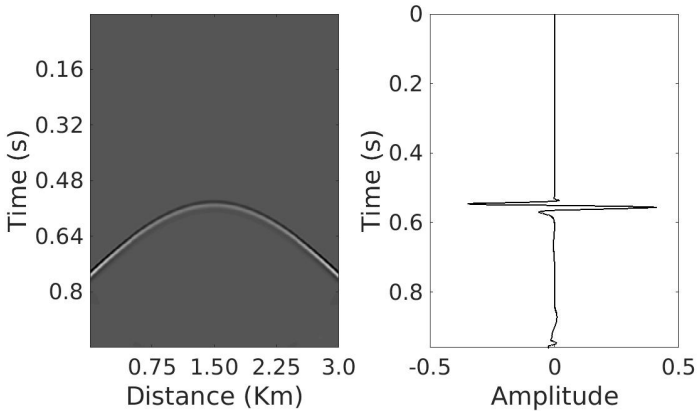

Figure 2.5: Seismic signal recorded on the surface (left) and seismic trace at $x = 1.7$ Km (right)

The data volume that represents the receiver wavefield is shown in Figure 2.6. The snapshots are at the same time values 80, 140, 210, 270, 340, 400, 460 and 510 milliseconds. The total propagation time of the wave was also 1.2 seconds. The propagation of the wavefield was done in reverse time as shown in eq. (2.14) and eq. (2.15).

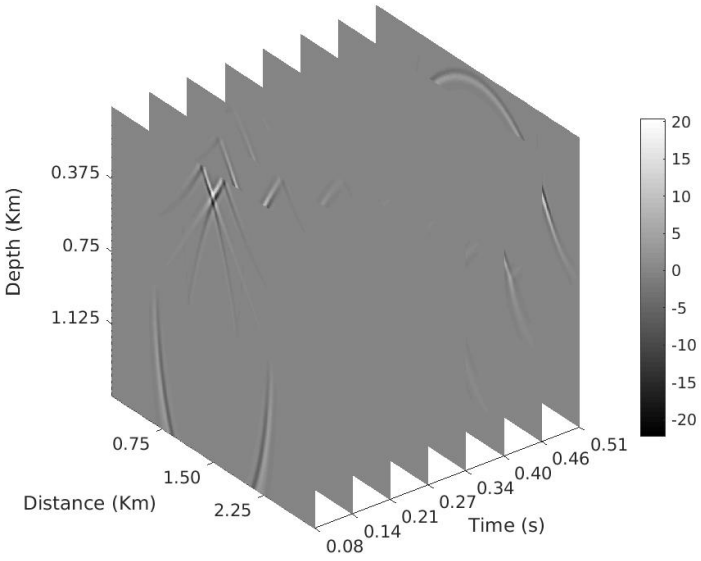

Figure 2.6: Snapshots of the receiver wavefield for data recorded on the surface due to a shot located at $x = 1.5$ Km

Figure 2.7 corresponds to the RTM model obtained by zero-lag cross-correlation imaging condition given by eq. (2.17). We can note the high correlation between the source and receiver wavefields represented by the high amplitude values near to the reflector. The units of the model are amplitude squared and due to this the amplitude model has no physical interpretation as a reflection coefficient. It has arbitrary scaling that depends on the source strength, that is, if the amplitude of the source strength is increased, the amplitude model also increases.

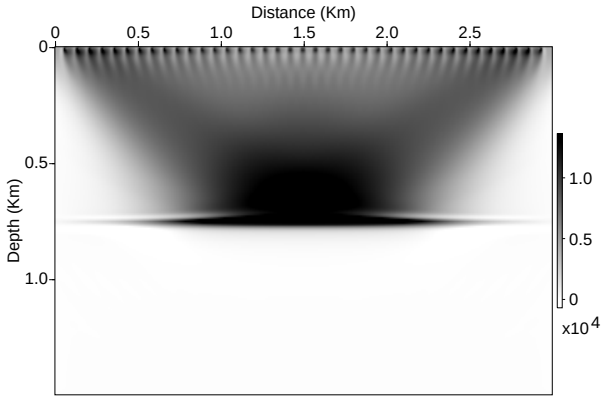

Figure 2.7: Scalar field two-layer model

2D SEG-EAGE salt model

The $2D$ SEG-EAGE salt model has a complicated structural nature, which is representative of salt intrusions such as those that can be found in the Colombian Caribbean. The length of the model is 4.91 Km; the depth of model is 1.14 Km. The velocity field of the wave propagation is shown in Figure 2.8.

We lay out 14 source points. The first source is located at 0.33 Km and the last one at 4.59 Km. The source interval is 328 m, each shot contains 1290 receivers and the receiver interval is 3.81 m.

Figure 2.9 shows some snapshots of the data volume representing the source wavefield obtained by eq. (2.8). The wavefield was obtained with a source located at $x = 2.45$ Km on the surface. The snapshots correspond to the times 160, 210, 260, 310, 360 and 410 milliseconds. The total propagation time of the wave was 3.5 seconds. We can note the wavefront propagation from the origin of the source on the surface for specific times.

The receiver wavefield is obtained by eq. (2.15) and using the seismic signal (Seismogram) recorded on the surface. Figure 2.10 shows the seismic signals recorded on the surface due to the forward propagation with a source located at $x = 2.45$ Km on the surface and a seismic trace from a receiver located at $x = 2.66$ Km.

The data volume that represents the receiver wavefield is shown in Figure 2.11. The snapshots are at the same time values 160, 210, 260, 310, 360 and 410

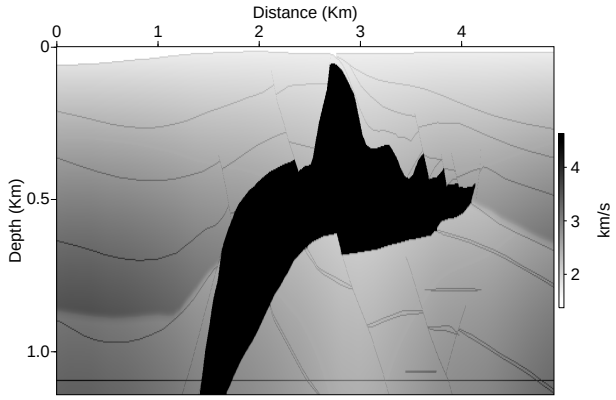

Figure 2.8: 2D SEG-EAGE velocity model

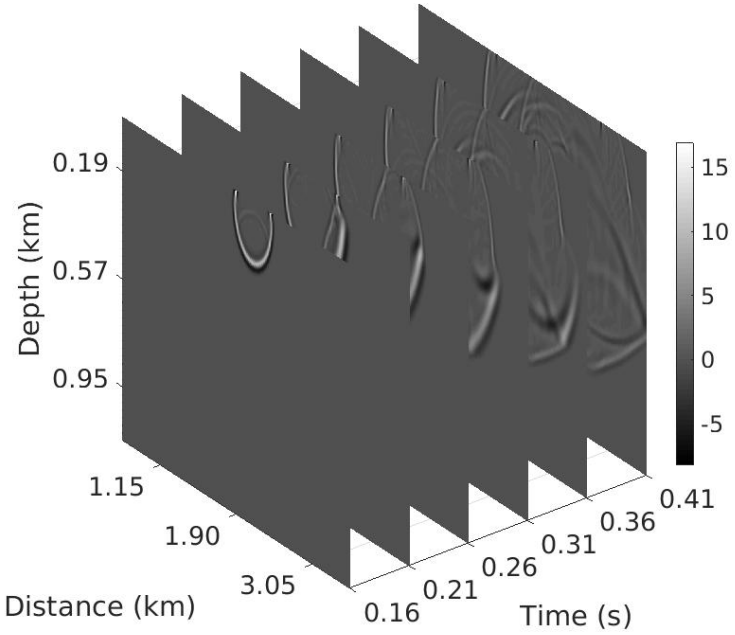

Figure 2.9: Snapshots of the source wavefield for a source located at $x = 2.45$ Km on the surface

milliseconds. The total propagation time of the wave was also 3.5 seconds. The propagation of the wavefield was done in reverse time as shown in eq. (2.14) and

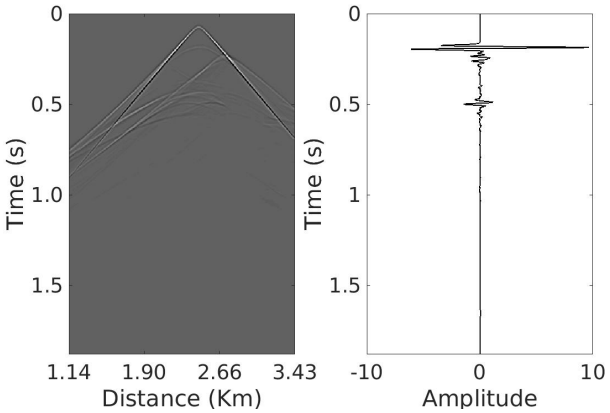

Figure 2.10: Seismic signal recorded on the surface (left) and seismic trace at $x = 2.66$ Km (right)

eq. (2.15).

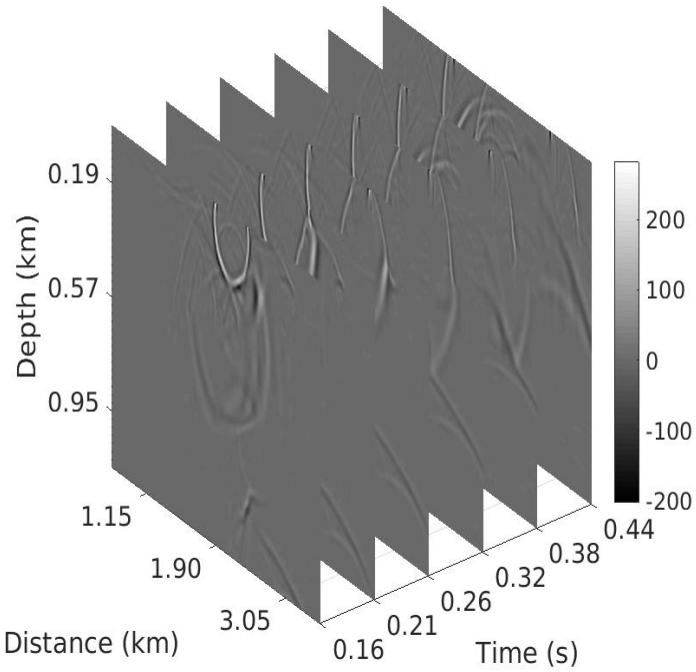

Figure 2.11: Snapshots of the receiver wavefield for data recorded on the surface due to a shot located at $x = 2.45$ Km

The RTM model obtained by using the zero-lag cross-correlation imaging condition given by eq. (2.17) is shown in Figure 2.12.

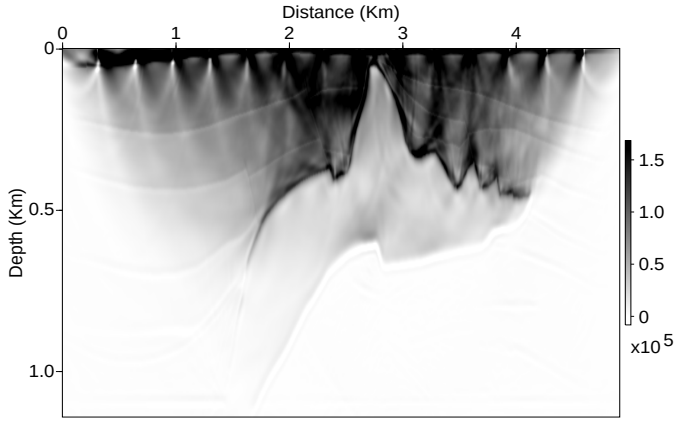

Figure 2.12: Scalar field 2D SEG-EAGE

The high correlation between the source and receiver wavefields are evident in the high amplitude values of the model in the shallow parts and near to salt body. These high amplitude values can hide important details in the image especially below the salt body. Some areas have strong energy due to the focusing effects of the salt body but the energy in the subsalt area is weak. These effects are caused by the geometrical shapes of the salt body and the strong variations (Singularities) in the velocity field.

Summary

In this chapter, we developed the mathematical foundations and the implementation of RTM algorithm. we showed that the RTM algorithm and the zero-lag cross-correlation imaging condition produces spatial low-frequency uncertainties (Artifacts) in the scalar field due to the correlation between of the incident and reflected wavefields in points at locations are not reflections points. These artifacts can hide important details in the scalar field and can increase the risk of a bad interpretation. Different techniques have been proposed to remove or attenuated the artifacts and they were briefly described above. Through numerical examples we illustrated the effects of artifacts in the scalar fields and their behavior in presence of complex wave propagation velocity fields. In the next chapters we will focus on providing tools to understand the behavior of uncertainties in seismic signals and scalar fields in order to propose a method to reduce or eliminate them in the stages of pre-obtaining or post-obtaining the scalar field which represents subsurface structures.

Next chapter (Chapter 3) will be focused on the analysis of traces from receiver

wavefield $R(\mathbf{x}, t)$ at $z = 0$, it means seismic signals recorded on surface used for the backward extrapolation of the wavefield presented in section 2.1.2.

References

[1] F. Liu, G. Zhang, S. Morton, and J. Leveille, *An effective imaging condition for reverse time migration using wavefield decomposition,* Geophysics **76**, 29 (2011).

[2] E. Baysal, D. D. Kosloff, and J. W. C. Sherwood, *Reverse time migration,* Geophysics **48**, 1514 (1983).

[3] D. Loewenthal and M. I. , *Reverse time migration in spatial frequency domain,* Geophysics **48**, 627 (1983).

[4] G. A. McMechan, *Migration by extrapolation of time - depend boundary values,* Geophysics Prospecting **31**, 413 (1983).

[5] K. Akanksha and G. N. Kumar, *Parallelization of reverse time migration using MPI+OpenMP ,* 2016 International Conference on Advanced Communication Control and Computing Technologies (ICACCCT) , 695 (2016).

[6] J. Amado, W. Salamanca, F. Vivas, and A. Ramírez, *A GPU implementation of the reverse time migration algorithm,* 14th International Congress of the Brazilian Geophysical. Expanded abstracts , 1016 (2015).

[7] R. Abdelkhalek, H. Calandra, O. Coulaud, G. Latu, and J. Roman, *Fast seismic modeling and reverse time migration on a GPU cluster,* The 2009 high performance computing & simulation - HPCS'09 , 36 (2009).

[8] H. Liu, B. Liu, H. Liu, X. Tong, and Q. Liu, *The algorithm of high order finite difference pre-stack reverse time migration and GPU implementation,* Chinese journal of geophysics **53**, 600 (2010).

[9] R. Stolt and A. Weglein, *Seismic imaging and inversion. Application of linear inverse theory*, Vol. 1 (Cambridge University Press, 2012).

[10] P. Farmer, S. Gray, D. Whitmore, G. Hodgkiss, A. Pieprzak, D. Ratcliff, and D. Whitcombe, *Structural imaging: Toward a sharper subsurface view,* Oilfield review **5**, 28 (1993).

[11] G. E. Backus, *Lon-wave elastic anisotropy produce by horizontal layering,* Journal of geophysical research **67**, 4427 (1962).

[12] V. Cerveny, *Seismic Ray Theory* (Cambridge University Press, 2001).

[13] L. Thomsen, *Understanding seismic anisotropy in exploration and exploitation*, Distinguished Instructor Series (Society of Exploration Geophysicists, 2002).

[14] M. A. Dablain, *The application of high-order differencing to the scalar wave equation,* Geophysics **51**, 54 (1986).

[15] L. Lines, P. Slawinski, and P. Bording, *recipe for stability analysis of finite-difference wave-equation computations,* Geophysics **64**, 967 (1999).

[16] A. Reynolds, *Boundary conditions for the numerical solution of wave propagation problems ,* Geophysics **43**, 1099 (1978).

[17] C. Cerjan, D. Kosloff, R. Kosloff, and M. Reshef, *A nonreflecting boundary condition for discrete acoustic and elastic wave equations,* Geophysics **50**, 705 (1985).

[18] J. F. Claerbout, *Toward a unified theory of reflector mapping,* Geophysics **36**, 467 (1971).

[19] S. Chattopadhyay and G. McMechan, *Imaging conditions for prestack reverse time migration,* Geophysics **73**, 81 (2008).

[20] D. Kosloff and E. Baysal, *Migration with the full wave equation,* Geophysics **48**, 677 (1983).

[21] O. Youn and H. Zhou, *Depth imaging with multiples,* Geophysics **66**, 246 (2001).

[22] A. Guitton, B. Kaelin, and B. Biondi, *Least-square attenuation of reverse time migration,* 76th International Annual Meeting, SEG, Expanded abstracts , 2348 (2006).

[23] D. Loewenthal, P. Stoffa, and E. Faria, *Suppressing the unwanted reflections of the full wave equation,* Geophysics **52**, 1007 (1987).

[24] S. Y. Sun and J. Cai, *Reverse-time migration by fan filtering plus wavefield decomposition,* SEG 2009 International Exposition and Annual Meeting , 2804 (2009).

[25] A. Guitton, A. Valenciano, D. Bevc, and J. Claerbout, *Smoothing imaging condition for shot-profile migration,* Geophysics **72**, 149 (2007).

[26] E. Baysal, D. D. Kosloff, and J. W. Sherwood, *A two way nonreflecting wave equation,* Geophysics **49**, 132 (1984).

[27] A. Valenciano and B. Biondi, *Deconvolution imaging condition for shot profile migration,* 73th International Annual Meeting and exposition, SEG, Expanded abstracts , 1059 (2003).

[28] B. Kaelin and A. Guitton, *Imaging condition for reverse time migration,* 76th International Annual Meeting and exposition, SEG, Expanded abstracts , 2594 (2006).

[29] R. Pestana, A. Dos Santos, and E. Araujo, *RTM imaging condition using impedance sensitivity kernel combinated with the Poynting vector,* SEG Technical Program Expanded Abstracts , 3763 (2014).

[30] J. Shragge, *Reverse time migration from topography,* Geophysics **79**, 1 (2014).

[31] J. Schleicher, J. Costa, and A. Novais, *A comparison of imaging for wave-equation shot-profile migration,* Geophysics **73**, S219 (2007).

[32] R. Fletcher, P. Fowler, and P. Kitchenside, *Suppressing artifacts in prestack reverse time migration,* 75th International Annual Meeting, SEG, Expanded abstracts , 2049 (2005).

[33] K. Yoon and K. Marfurt, *Reverse time migration using the Poynting vector,* Exploration Geophysics **37**, 102 (2006).

[34] F. Vivas and R. Pestana, *Imaging condition to true amplitude shot-profile migration: A comparison of stabilization techniques,* 10th International congress ofnthe Barazilian Geophysical Society , 1668 (2007).

[35] M. Haney, L. Bartel, D. Aldridge, and N. Symons, *Insight into the output of reverse time migration: What do the amplitudes mean?* 75th International Annual Meeting, SEG, Expanded abstracts , 1950 (2005).

[36] J. Costa, F. Silva, R. Alcántara, J. Schleicher, and A. Novais, *Obliquity-correction imaging condition for reverse time migration,* Geophysics **74**, S57 (2009).

[37] T. W. Fei and Y. Luo, *De-blending reverse time migration,* SEG 2010 International Exposition and Annual Meeting , 3130 (2010).

[38] L. Hu and G. McMechan, *Wave-field transformations of vertical seismic profiles,* Geophysics **52**, 307 (1987).

[39] M. Cogan, R. Fletcher, R. King, and D. Nichols, *Normalization strategies for reverse-time migration,* SEG Annual meeting Society of Exploration Geophysicists , 3275 (2011).

[40] N. Whitmore and S. Crawley, *Applications of RTM inverse scattering imaging conditions,* 82nd Annual International Meeting, SEG, Expanded abstracts , 779 (2012).

[41] B. Nguyen and G. McMechan, *Excitation amplitude imaging condition for prestack reverse time migration,* Geophysics **78**, 37 (2013).

[42] B. Arntsen, B. Kritski, B. Ursin, and L. Amundsen, *Shot-profile amplitude crosscorrelation imaging condition,* Geophysics **78**, S221 (2013).

[43] Y. Qin and R. McGarry, *True-amplitude common-shot acoustuc reverse time migration,* SEG Annual meeting Society of Exploration Geophysicists (2013).

[44] T. Chen and B. He, *A normalized wavefield separation cross-correlation imaging condition for reverse time migration based on Poynting vector,* Applied Geophysics **11**, 158 (2014).

[45] C. Ren, G. Song, and X. Tian, *The use of Poynting vector in wave-field decomposition imaging condition for reverse time migration,* Journal of Applied Geophysics **112**, 14 (2015).

[46] P. Shen and U. Albertin, *Up-Down separation using Hilbert transformed source for causal imaging condition,* SEG Annual meeting Society of Exploration Geophysicists, Expanded abstracts , 4175 (2015).

[47] Z. Wang, H. Ding, G. Lu, and X. Bi, *Reverse-tiome migration based optical imaging,* IEEE Transactions on medical imaging **35**, 273 (2016).

[48] E. Wang and Y. Liu, *Reverse time migration using analytical wavefield and wavefield decomposition imaging condition,* 86th Annual International Meeting, SEG, Ex- panded abstracts , 4461 (2016).

[49] T. W. Fei, Y. Luo, and F. Qin, *An endemic problem in reverse-time migration,* 84th Annual International Meeting, SEG, Expanded Abstracts (2014).

[50] M. Wang and S. Xu, *RTM artifact removal via a fast algorithm for wavefield decomposition ,* 86th Annual International Meeting, SEG, Expanded abstracts , 4690 (2016).

3

Singularity analysis of a receiver wavefield

In this chapter, we apply a singularity spectrum algorithm to the signal from a seismogram, and analyze the features of the traces, extracting their main information in the time-scale domain and providing clues to the possible eradication of artifacts by use of the zero-lag cross-correlation imaging condition in operator Reverse Time Migration. "Candle drooling" is a unique feature of the scale profile of a wave signal that can be used to identify the location of the energy of a set of scales at a certain time. The energy must not be treated as noise, and the complexity of the trace signal must be taken into account, to avoid eliminating the real features of the subsurface when tuning the final model. We propose a method to extract relevant features about the receiver wavefield in order to use this information on the subsurface contained to understand phenomena related to attenuation and reflection.

This chapter is an extended version of a submitted paper in Nature Geosciences [1]

When enhancing models of subsurface structures using RTM, the results depend mainly on the number of shots gathered and the simulation time taken to reach the correct depth, making it a computationally expensive procedure. In numerical wave propagation, the change in amplitude from the source and receiver wavefields, and the reflectivity of the waves at a certain velocity gradient, may produce misleading results when applied to the final RTM model.
Researchers have been investigating enhancement approaches in which imaging procedures are applied to the structural reconstruction of the image or to its subsequent post-processing.

Other on-going research is investigating the extension of numerical RTM methods to applications in high-performance computing. This will require improving the algorithms and imaging conditions, among other things. We are interested in identifying strategies that will allow the content of seismic traces or wave fields to be used to support the RTM technique, assuming the highly uncertain velocity model that is typical in real life applications. We are also exploring the possibility of localizing certain reflective effects that arise in imaging, to improve imaging procedures or post-processing strategies.

Seismic imaging resolution has been a major topic in seismology. However, most of the methods used in this field are based on ray theory. A number of techniques exist that allow seismic illumination to take advantage of full wave inversion, but their computational costs make them impractical. An attempt has been made to combine seismic wave illumination, seismic migration imaging, and imaging resolution analysis [2]. Fourier analysis has been applied to investigate the physical meaning of the 2D wavenumber spectrum. The results suggest that the illumination vectors of all source and receiver pairs sum at the position of interest. When applying ray tracing theory, this can be expressed as a source and receiver point within a local range. The attributes of the Point Spread Function have been applied to the imaging resolution of the target, using different geometrical parameters. When Hilbert transform is applied, the size of the envelope reflects the degree of resolution, while the amplitude of the envelope reflects the sharpness of the imaging point: the larger the amplitude, the sharper the image.

Frequency analysis is another widely used seismic method, and time-scale (wavelet) analysis remains popular in certain fields of information retrieval. These seek to identify the relationship between the numerical results and the physics of the phenomenon under investigation. A range of features have been addressed in the search for better methodologies, and in deriving explanations of attenuation, the elastic parameters, geothermal properties, porosity, temperature, and the velocity field. In this section, we present examples of the use of time-scale and transformed domains.

Spectral decomposition is used to extract the frequency components from seismic data. A number of spectral decomposition techniques have been proposed, including the short-time Fourier transform, continuous wavelet transform, the S transform, matching pursuit decomposition, and instantaneous spectral analysis. The Gabor-Morlet (G-M) transform, a subtype of continuous wavelet transform, has also been used for the high-resolution that it offers. It has been applied to low-

frequency seismic analysis and the direct detection of hydrocarbon indicators of homogeneous and heterogeneous reservoirs [3].
LeBras and Mcllmati (1995) presented a method that reduced the computational cost of the depth migration method when applied to seismic data [4]. Their proposed method solved the downward continuation problem in seismic data migration, and reduced the computation overhead by applying wavelet transform. This was applied to all the frequency components of the downward continuation operator of the velocity field, defining a downward continuation operator in the wavelet domain. Wavelet transform of the spatial dimension was also applied to the collection of trace functions, after transforming the time/amplitude traces by applying a standard fast Fourier transform method to the frequency/amplitude traces. This allowed the operators to be properly combined, producing a definition in the wavelet domain of all traces at the desired depths. Finally, the frequency components were used to display the depth/amplitude data as a function of depth.

Schmelzbach et al. (20l6) suggested that seismic methods can be extended to provide quantitative estimates of elastic parameters, from which it may be possible to derive the key geothermal properties, such as porosity and temperature [5], Another suggestion is that a method using controlled seismic sources may provide high-resolution characterization of faulting and fracturing at the depths necessary for successful well silting. Research has addressed a number of major challenges confronting hard-rock seismic exploration. These include i) the typically weak reflection amplitudes. These affect the signal-to-noise (S/N) ratio, making it difficult to image the interior features of crystalline rocks. ii) The complex morphology, lithology, and deformation, which mean that reflectors are often small, steeply dipping, and laterally discontinuous. iii) The high-velocity of results from the crystalline basement creates longer wavelengths and reduces resolution. iv) Long aperture recordings are needed if reliable velocity information is to be recovered. v) Fractures and layering may create anisotropy, making wave propagation more complex [6]. They also noted that steam increases the absorption of the seismic wave field while decreasing the seismic velocity [7].

The use of migration velocity analysis is also required for effective imaging, as the macro velocity field must be obtained. The derived interval velocities can also contribute to geological and petrological understanding, for example by identifying the type, condition, and fluid content of the rock. When using full wave inversion techniques, appropriate constraint of the velocity model allows quantitative estimates to be made of variation in attenuation [8, 9]. The key point is that simultaneous application of P and S wave attenuation imaging may potentially yield information on temperature variation and fluid saturation. Ge et al. (2016) proposed a method based on the application of a shaping filter in the generalized S transform domain for wavelet distortion correction in depth-converted data [10]. On the assumption that the reflection sequences in a selected window are sparse, the authors developed a window-based filtering scheme. The claimed benefits of this method are: higher resolution at greater depth, more accurate estimation of the properties of thin reservoirs, and accurate identification of deep well ties, due to the absence of depth-dependent wavelet stretching. The consistency of the wavelets also makes

interpretation of the depth data straightforward.

Attenuation can then be measured either in the time domain, using the amplitude decay of the signals over distance/time, or in the frequency domain, by quantifying the spectral changes. In attenuation estimation, research has focused on the use of instantaneous frequencies and the wavelet transform for the calculation of the synchro squeezing transform (SST) and other high-resolution time-frequency transformations [11]. The analysis of Tary et al. (2017) demonstrated that, even when spectra are discontinuous, highly-localized time-frequency transforms can be used for attenuation measurement in geophysical and other applications.

Zhang and Fomel (2017) presented a technique for wavelet extraction that applied local-attribute-based time-frequency decomposition to seismic inversion [12]. Such techniques assume that seismic data are non-stationary because of noise contamination and attenuation due to wave propagation, so that the frequency spectrum of the seismic signal changes when captured from shallow and deep formations. The study also estimated subsurface acoustic impedance, allowing the seismic data to be understood in terms of physical phenomena. In practice, field seismic data are always non-stationary, as wave attenuation causes the spectrum to change with depth. The goal of the study was to use local spectra to estimate the time-variant wavelet along the time axis, rather than assuming a constant wavelet for the whole trace, allowing the non-stationarity of the seismic data to be taken into account.

We postulate that, in a synthetic exercise, the seismic traces represent the so-called true information about the physical phenomenon, and assume that in real applications these are fully available when analyzing the subsurface information. They can also be treated as wave fields of zero depth. Our premise is that, when a seismic wave is sent from the surface to the subsurface and reflected from a medium that changes its velocity, it experiences a range of wave propagation effects, including noise contamination, dispersion, and attenuation [1]. Each of these may distort the frequency components of the seismic signal when recorded at the surface, introducing discrepancies between the data and the model [12].

Based on these assumptions, we propose the use of the time-scale (continuous wavelet transform) and singularity spectrum to extract information from the seismic traces or wavefields. we apply a singularity spectrum algorithm to the signal from a seismogram, and analyze the features of the traces, extracting their main information in the time-scale domain.

Our hypothesis is that the time-scale or time-frequency content of the signal reveals the nature of the medium and its physical effect, and will therefore provide information on the full wave inversion or RTM processes. We also discuss the singularity spectrum and the information retrieved from seismic trace signals.

It was introduced that to obtain the complete source wavefield $S(x,z,t)$ and the complete receiver wavefield $R(x,z,t)$ using RTM from eq. 2.8 and eq. 2.15, we apply the acoustic wave equation using a velocity field $c(x,z)$ and use seismic signals from surface.

If we call the receiver wavefield at $z=0$ by $r(x,t)=R(x,z=0,t)$ and source wavefield at $z=0$ as $s(x,t)=S(x,z=0,t)$, we can think the phenomenon as

$s(x,t)$ propagating through the media with $c(x,z)$, and the changes in $r(x,t)$ carries information of the traveler wave on the velocity field and its singularities.

Hence, for backward propagation 2.1.2 we assume that signal $r(x,t)$ propagating through $c(x,z)$ allows $R(x,z,t)$ to be obtained, capturing useful information about the subsurface structure and changing the frequency components in the traveling signal. By applying singularity analysis to $R(x,z,t)$ this information can be retrieved.

The goal is to establish a relationship between the coefficients of the wavelet transform and the spatial localization of changes in the velocity fields. The singularity spectrum of each trace can also be correlated with attenuation or reflective events reflected by changes in the velocity field, such as the presence of complex structures or large changes in velocity in the vertical or horizontal direction. Our contribution relies on demonstrating the capacity to extract features from signals and their location to improve the RTM method. The algorithm may offer wavefield separation in imaging using RTM (Chapter 4).

The chapter is organized as follows: Section 3.1 presents the theoretical framework underpinning singularity analysis and the wavelet transform modulus maxima (WTMM). Section 3.3 introduces the methodology used for singularity analysis and section 3.3.1 the singularity spectrum results obtained from three synthetic datasets: a two-layer velocity field, a velocity field with a high-velocity intrusion, and a small salt velocity field. We discuss their relationship to the velocity field properties. Section 3.4 presents our conclusions.

3.1. Continuous Wavelet signal analysis

Time-frequency analysis with short-time Fourier transform has been demonstrated to reveal patterns that can be used for signal characterization. An alternative approach to signal pattern extraction uses wavelet transform with complex wavelets. The Singularity Spectrum (SA) extracts specific features and quantifies the derivability of a function around a certain point, offering a different way of understanding the information contained in a signal. Signals whose singularity behavior presents specific patterns can be found in precipitation analysis [13], the vibrant signals used in fault detection [14], machine fault diagnosis [15], time series seismic data [16], DNA sequencing, and satellite imaging [17]. As noted above, frequency analysis has been widely used in seismic analysis. Time-scale (wavelet) analysis remains popular in certain areas of information retrieval. The goal is to associate the numerical results with the real physics of the phenomenon under investigation.

In the search for improved methods, and an improved understanding of attenuation, a range of features have been investigated. They include elastic parameters, geothermal properties, porosity, temperature, and the velocity field. In the following section, we present the theoretical framework underpinning the analysis of seismic traces in migrated synthetic models. In developing the singularity analysis, certain steps related to the WTMM must be applied to the time-scale structure of the signal, and the role of the Hölder exponent must be considered.

3.1.1. Integral transforms

Linear integral transforms have being used in multiple knowledge fields such as quantum mechanics, quantum field theory, quantum theory of scattering, viscoelasticity, circuit theory, dielectric theory, magnetic resonance, among others [18, 19]. In general, the linear integral transform convert a given function $f(x)$ of the variable x, to another function $g(k)$ of the same or different variable. These transform can be defined by

$$g(k) = \int_{C_n} K_n(k,x) f(x) dx \tag{3.1}$$

where K_n with $n = 1, 2$ are generic functions from the variables k and x known as transform kernel, for both the transform with $n = 1$ as for its inverse with $n = 2$ C_n denotes the path in the complex plane. In particular, if $f(x)$ is well-known and K_1 and C_1 are specified, it is possible to obtain $g(k)$ if the function is integrable. On the other hand, this equation is also a linear integral transform for $f(x)$ when $g(k)$, K_2 and C_2 are specified. For each integral transform there exist a relation that turns the transformed function into the original function, usually this relation its also an integral transform, that may be written in terms of algebraic operations. There exist a biunivocal relation among the function and its transform (2010, [20]).

There are many integral transformations such as the Fourier transform, the Laplace transform, the Mellin transform, the Hankel transform, the Hilbert transform, among others, which are widely used to solve initial and boundary value problems involving ordinary and partial differential equations and other problems in mathematics, science and engineering.

In this thesis, we apply different linear integral transforms on 2D or 3D real-valued functions or fields to obtain another 2D or 3D function or field with real or complex values. In next sections, we will describe the wavelet transform modulus maxima (Section 3.1.2) and the continuous wavelet transform (Section 3.1.3). In section 5.1.2, the Laguerre-Gauss transform is shown.

3.1.2. Wavelet transform Modulus Maxima (WTMM)

Jaffard [21] studied the relationship between wavelet transform and the regularity of a function, demonstrating that, at small scales, the decay of the coefficients of the wavelet transform allows the regularity of a function to be approximated. When applying the modulus maximum transform (MMWT) it is necessary to define the continuous wavelet transform, the scalogram, and the Hölder exponent.

3.1.3. Continuous Wavetet Transform

This mathematical tool allows a signal $f(t)$ to be analyzed in the two dimensions of time and scale. The latter is inversely proportional to the frequency, and mimics the short-time Fourier transform. The signal is decomposed into packets localized by time and frequency. Wavelet transform allows multiresolution analysis, image compression, and the detection of singularities and abrupt changes in the signal or image [22, 23, 24]. The following definitions are useful aids to understanding:

Definition 3.1.1 *Wavelet as inner product*

$$\begin{aligned} W_f(u,s) &= \langle f(t), \psi_{u,s}(t) \rangle \\ &= \frac{1}{\sqrt{s}} \int_{-\infty}^{\infty} f(t) \psi^* \left(\frac{t-u}{s} \right) dt \end{aligned} \tag{3.2}$$

Definition 3.1.2 *Wavelet as convolution*

$$\begin{aligned} W_f(u,s) &= \int_{-\infty}^{\infty} f(t) \bar{\psi}_s^*(u-t)\, dt \\ &= f(u) * \bar{\psi}_s^*(u) \end{aligned} \tag{3.3}$$

Definition 3.1.3 *Mother Wavelet*

$$\int_{-\infty}^{\infty} t^p \psi(t) dt = 0, \forall p \in \{0, 1, \ldots, (n-1)\} \tag{3.4}$$

Definition 3.1.4 *Gaussian Wavelet*

$$\psi_n(t) = c_n \frac{d^n}{dt^n} \left(e^{-t^2/2} \right) \tag{3.5}$$

$$\hat{\psi}_n(\omega) = c_n (i\omega)^n e^{-\omega^2/4} \tag{3.6}$$

The scalogram of a signal represents the values of the coefficients of its continuous wavelet transform on a time-scale plane. Figure 3.4a shows a continuous wavelet transform of a seismogram trace in the two-layer velocity model in Figure 3.3a. It shows the wide range of frequencies (on inverse scales) in the seismic signal. The wave that originally propagated through the velocity field is in the form of a Ricker pulse, with a central frequency of 40 Hz.

3.1.4. Hölder Exponent

The Taylor Theorem allows the approximation of a function that is derivable n times in terms of polynomials of order not less than n and an error term.

Theorem 3.1.1 *If a function $f(t)$ is derivable n times in the interval of center u and radius ϵ, then:*

$$f(t) = \sum_{k=0}^{n-1} \frac{f^{(k)}(u)}{k!} (t-u)^k + \frac{f^{(n)}(\xi)}{n!} (t-u)^n \tag{3.7}$$

The final term in Equation (3.7) is known as the error term. It is straightforward to demonstrate that the term can be bounded as follows:

$$\begin{aligned} |R_u(t)| &= \left| \frac{(t-u)^n}{n1} f^n(\xi) \right| \leq \frac{|t-u|^n}{n!} \\ \sup_{\xi \in [u-\epsilon, u+\epsilon]} f^{(n)}(\xi) &= A|t-u|^n, \forall t \in [u-\epsilon, u+\epsilon] \end{aligned} \tag{3.8}$$

This allows us to characterize the derivability of a function $f(t)$ by approximating the function using polynomials. It also provides a strong bound for the error. This definition is not sufficiently robust, as the degree of differentiability is limited to integers. For this reason, the Lipschitz or Hölder exponent is used instead. This allows the smoothness of a function to be measured using real numbers.

Definition 3.1.5 *A distribution $f(t)$ is Hölder of order $\alpha \geq 0$ in a point u, if there exists a constant $C > 0$ and a polynomial $P_n(t)$ of order n such that, for all t exists a vicinity u that satisfies*

$$|f(t) - P_n(t-u)| \leq K|t-u|^{\alpha} \tag{3.9}$$

The Fourier transform gives a frequency analysis of a signal of function $f(t)$ and characterizes the regularity at the global level in all **R**.

Theorem 3.1.2 *A function $f(t)$ is bounded and uniformly Hölder of order α in all **R** if and only if*

$$\int_{-\infty}^{\infty} |\hat{f}(\omega)|(1+|\omega|^{\alpha})d\omega < +\infty \tag{3.10}$$

This gives only a global view of the regularity of a function $f(t)$, and does not provide an analysis of regularity in the vicinity of a point u. In contrast, the decay of the wavelet transform allows strong local variations around this point to be detected. It can be regarded as a mathematical microscope. Before its introduction, certain properties of the wavelet transform that are necessary when estimating the value of the regularity α must be considered.

Theorem 3.1.3 *The family $\psi_n(t)$ is a set of wavelets with n vanishing moments and faster decay. It is generated as follows:*

$$\psi_n(t) = (-1)^n \frac{d^n \vartheta(t)}{dt^n}, \text{ with } \vartheta(t) = e^{-t^2/2} \tag{3.11}$$

When describing the WTMM, one further necessary condition and one sufficient condition must be introduced.

Theorem 3.1.4 *Let $f(t)$ be a Hölder function of order α in point τ and $\phi(t)$ a wavelet with $n \geq \alpha$ vanishing moments and n derivatives with faster decay. There then exists a constant $Q > 0$ such that*

$$\left|W_f(u,s)\right| \leq Q_s^{\alpha+1/2}\left(1+\left|\tfrac{u-\tau}{s}\right|^{\alpha}\right) \tag{3.12}$$
$$\forall (u,s) \in R \times R^{+}$$

This condition is necessary but not sufficient. It shows that the value of the regularity α bounds the absolute values of the coefficients for the wavelet transform, and that they decay in the same sense as the scale decreases. The fact that this is

not a sufficient condition does not limit the approximation for the Hölder exponent in numerical terms [25].
Finally, the WTMM corresponds to the entire set of local maximum points of the absolute value of the wavelet transform.

$$WTMM = \frac{\delta \left|W_f(u,s)\right|}{\delta u}\Big|_{u=u_0, s=s_0} = 0 \quad \text{with } (u_0, s_0) \in (R \times R^+) \tag{3.13}$$

The set of WTMM points concatenated across scales are known as maximum lines. These lines are fundamental in the calculation of the Hölder exponent. Mallat and Hwang (1992) demonstrated that an explicit relationship holds between the two [26], so that a point τ is Hölder of order $0 < \alpha < 1$ if there exists a succession of local maxima (u_q, s_q) that converge on point $(\tau, 0)$ when q when n tends to infinity. This does not guarantee that any maximum modulus will be part of a convergent succession at the small scale, but when using wavelets from the Gaussian family, all maximum lines will propagate at small scales as they are solutions to the heat equation. The maximum principle therefore guarantees the result [23, 26].

As noted above, the maximum modulus represents the local maxima of the function $\left|W_f(u,s)\right|$ for a fixed scale s. The WTMM provides as a result a set of points through the plane (u,s), and no maximum lines are defined. We call this set the skeleton of the maximum modulus transform.

3.2. Proposed numerical approach for singularity analysis

The lack of information about subsurface is one of the mayor concerns in RTM because there is no accurate information of the velocity field and it comes from experimental work and geological approaches. The only source of real data in RTM procedure that can be considered reliable is the acoustic signals from receivers (geophones or hydrophones) on surface.
By treating the seismic traces as signals, the above theoretical framework becomes crucial for the understanding of certain features and information retrieval.
Nevertheless, for massive data as seismic migration, the former theoretical approaches is not necessarily easy to compute, neither to analyze. Consequently the continuous wavelet transform, maximum modulus wavelet transform and Hölder exponent must be approached without loss of generality and information.
To approximate these lines, a local search algorithm must connect the points. The proposed method uses the following steps:

1. From the local maximum of the lowest scale, a local search is performed to find the m shortest distance points to the next two scales. In some cases, however, numerical errors prevent the identification of a local maximum relatively close to the next scale.

2. The smallest distance maximum point is assigned as the next point on the maximum line.

3. If two points have the same point as the shortest distance, the first is assigned as the closest point, and the other point as the second closest.

4. After the nearest local maximum has been assigning to all points, the algorithm moves to the connected points and repeats step 1 until all the local maximum points in the plane have been reached.

5. After concatenating the points, a linear approximation of eq. 3.12 is used to evaluate each maximum line in a range of scales $s \in [S_m, S_M]$, while maintaining the linear relationship.

Figure 3.1 shows an example of a scalogram generated using a trace from a small salt model. The trace corresponds to receiver wavefield $R(x, z, t)$ at $x = 0.375$ Km and $z = 0$ Km. It identifies changes in the scale spectrum of the signals from the complete phenomenon. The selection of the trace relies on its spatial location in the velocity model. Its meaning is discussed in a later section.

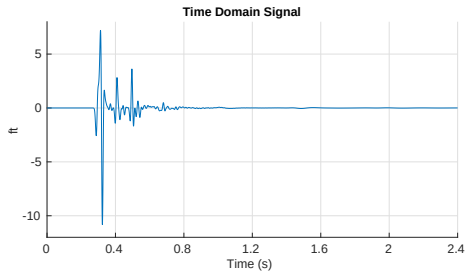

(a) Signal of trace 100

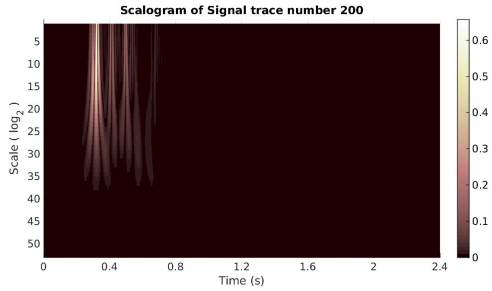

(b) Scalogram Seismogram 1

Figure 3.1: 3.1a Signal $f(t)$ (Seismic trace) of a seismogram of the RTM for small salt model (for details see Table 3.1) and its 3.1b scalogram.

Singularity spectrum analysis procedure

Our singularity spectrum algorithm applies a very simple procedure:

- Select a trace signal $f(t)$
- Perform continuous wavelet transform on signal $f(t)$
- Draw a scalogram of the analysis of the coefficients at multiple scales
- Calculate the WTMM
- Chain the maximum lines
- Approach the linear region for calculation of the Hölder exponent
- Calculate and plot the singularity spectrum

The goal is to establish a relationship between the coefficients of the wavelet transform and the spatial localization of changes in the velocity fields. The singularity spectrum of each trace can also be correlated with attenuation or reflective events reflected by changes in the velocity field, such as the presence of complex structures or large changes in velocity in the vertical or horizontal direction. Our contribution relies on demonstrating the capacity to extract features from signals and their location via Gaussian wavelet information retrieval capabilities to improve the RTM method. The algorithm may offer wavefield separation in imaging using RTM.
Figure 3.2 shows the singularity spectrum for three traces in a seismogram for a two-layer velocity model. Trace 100 and trace 200 represent the coefficients of alpha drawn as a straight line, whereas Trace 300 represents a nonlinear spectrum. This means that the Trace 300 signal changes its singularity (degree of derivability) over time.

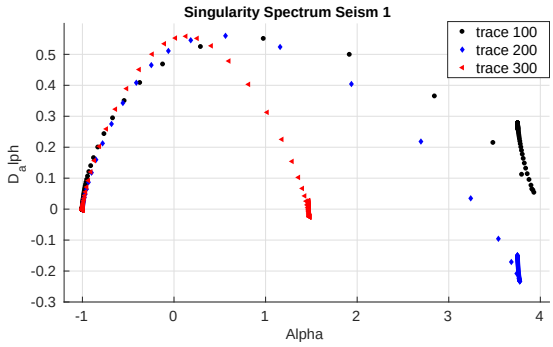

Figure 3.2: Singularity spectrum for three traces of a seismogram for the two-layer velocity field depicted in 3.3a

3.3. Experimental development

To pursue our hypothesis, we calculate the singularity spectrum and the information retrieved from seismic trace signals. We suppose that singularity analysis of $r(x,t)$ propagated through $c(x,z)$, which allows $R(x,z,t)$ to be obtained, embeds useful information about the subsurface structure. Applying singularity analysis to $R(x,z,t)$ yields information about the problem.
Our methodology analyzes the $R(x,z,t)$ at $z=0$ (seismogram) by applying singularity analysis based on the singularity spectrum and scalogram. This allows certain scale features to be time localized, and the fractal nature of the propagated signals to be evaluated.

The analysis must take into account the physics of the phenomenon, the known properties of structures such as salt bodies, and large changes in the velocity model. To Illustrate the effect of velocity changes on waves propagated with RTM, we will use as examples a simple model with two homogeneous and isotropic layers, a velocity model with three homogeneous layers and a high-velocity intrusion, and a small salt model. The dimensions of the models, number of shots, and time steps are listed in Table 3.1.

Table 3.1: The dimension of the models used for the experimental setup.

Model	Dimension	Shots	Seism.	Δt
Two-layer	3.0 x 1.5 Km	15	15	800 μs
High-velocity intrusion	4.5 x 2.25 Km	10	10	8.3 ms
Small salt	1.27 x 0.79 Km	10	10	400 μs

The goal is to find, for each model, both the scalogram and the singularity spectrum of selected traces of the different seismograms. The traces selected are spaced uniformly across the horizontal dimension of the 2D velocity model, and the seismograms are selected to show the spatial location of the surface geophones that register the signals. For example, if there are 15 seismograms in the model, seismograms 1, 7, and 15 will be selected for analysis.

The aim is to establish the relationship between the coefficients of the wavelet transform and the time-space localization of certain changes in the velocity field. The singularity spectrum of each trace should be related to possible attenuation or reflective events that produce changes in the velocity field, such as the presence of complex structures or large changes of velocity in the vertical or horizontal directions.

3.3.1. Results

The continuous wavelet transform of the seismograms is obtained from the data recorded at the surface $r(x,t)$ by forward modeling using $c(x,z)$ and $s(x,t)$ of each synthetic model, after applying the RTM procedure. A post-processing strategy is also used.
We first present the key results for the scalogram of the Trace 100 (Receiver wavefield $R(x,z,t)$ at $x=0.75$ Km and $z=0$) for the two-layer model based on seis-

mograms 1, 7 and 15 (Figure 3.4). For each seismogram, these correspond to the sources located at $x = 0.3$ Km, $x = 1.2$ Km, and $x = 2.5425$ Km and the singularity spectrum of Traces 100, 200 (Receiver wavefield $R(x, z, t)$ at $x = 1.5$ Km and $z = 0$), and 300 (Receiver wavefield $R(x, z, t)$ at $x = 2.25$ Km and $z = 0$).
Figure 3.3 shows the two-layer velocity field and the location of the sources that correspond to seismogram 1, 7 y 15.

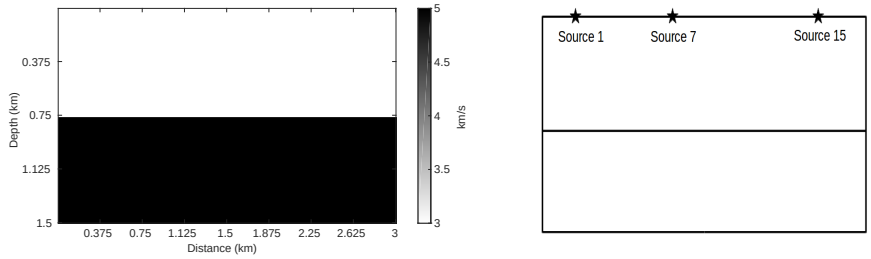

(a) Velocity model (b) Source location

Figure 3.3: 3.3a Two-layer velocity field and 3.3b source location.

In the case of the small salt velocity model shown in Figure 3.5, we will describe a case in which the traces reveal the presence of a salt body in the center of the model and the reflectivity events producing changes in velocity. This analysis uses time-scale analysis of Traces 100 and 200 against Trace 300 of seismograms 1 and 6, which correspond to sources located at $x = 0.15$ Km and $x = 0.6675$ Km. Figure 3.5a shows the small salt velocity model, illustrating the effect of the spatial location of the signals extracted at the surface. As shown in Figure 3.5b, Trace 200 of seismogram 6 (simulating a location at the top of the salt body) is chosen for calculation of the wavelet transform.
Figure 3.5c shows the scalogram and the relevant components in the time-scale domain.
In Figure 3.5d, the WTMM of the scalogram generated from a trace from the small salt model reveals the changes that have taken place in the scale spectrum of the signals for the full phenomenon. It is important to emphasize that the values that appear in the WTMM correspond to positive or negative values of the coefficients of the continuous wavelet transform of the seismic trace and in the next chapter this characteristic will be taken into account.
Figure 3.6 shows the scalogram of Trace 100 for the model, with high-velocity intrusion of seismograms 1, 6, and 10, corresponding to sources located at $x = 0.3075$ Km, $x = 2.1825$ Km and $x = 3.6825$ Km, and the singularity spectrum of Traces 100, 200, 300,400, and 500 for each seismogram.
Figure 3.7 shows the signal $f(t)$ of Trace 100 (located at $x = 371.25$ m) from seismogram 1 of the RTM of the small salt model, and the scalogram obtained using a Gaussian wavelet. Figure 3.8 shows the singularity spectra of three traces (100, 200 and 300) from seismogram 1, derived from the data recorded for the

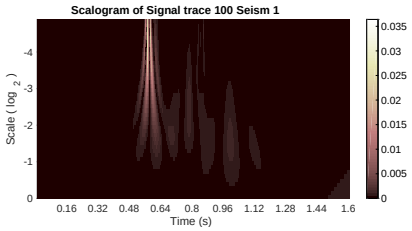

(a) Scalogram in seismogram 1

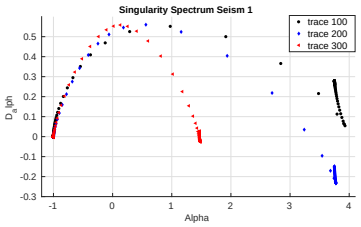

(b) Singularity spectrum seismogram 1

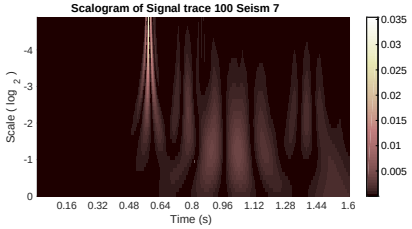

(c) Scalogram in seismogram 7

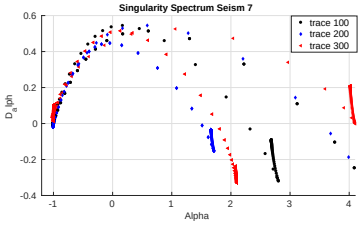

(d) Singularity spectrum seismogram 7

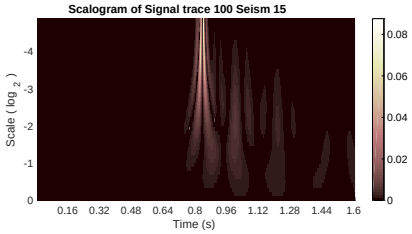

(e) Scalogram in seismogram 15

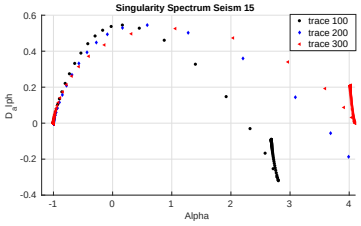

(f) Singularity spectrum seismogram 15

Figure 3.4: Scalogram of trace 100 in 3.4a seismogram 1, 3.4c seismogram 7 and 3.4e seismogram 12 looking for the spatial distribution in the two-layer model. 3.4b, 3.4d and 3.4f singularity spectrum for traces 100, 200, and 300 in seismograms 1, 7, and 15 respectively.

small salt model. Figure 3.9 shows the superposition of the full seismogram signal scalogram (individual continuous wavelet transform) for all traces in the small salt model.

3.4. Discussion

Previous studies have addressed the development of new imaging conditions for RTM by decomposing the source and receiver wavefields into their one-way propagation components, then applying correlation-based imaging to appropriate combinations of the decomposed variables [27]. Frequency-based techniques have been

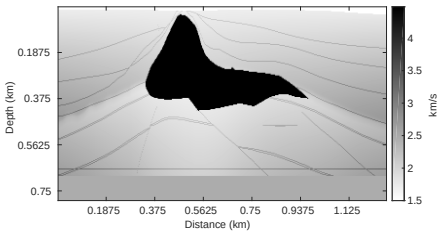

(a) Velocity model

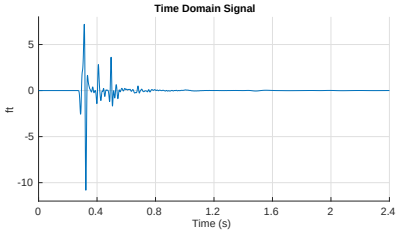

(b) Seismic Trace

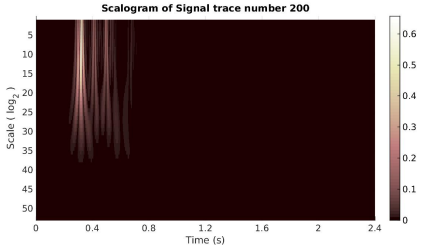

(c) Scalogram Seismogram

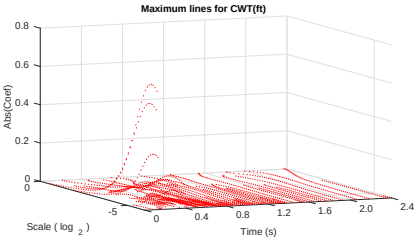

(d) Chainning of maximum lines

Figure 3.5: 3.5a Small salt velocity model; 3.5b Seismic trace 200 signal, 3.5c Scalogram 3.5d Chaining of maximum lines for a trace on a seismogram 6 of the data recorded $r(x,t)$

used to identify certain features in the wave fields (backward or forward) and special time-frequency or space-based values selected to distinguish the up and down components of the wave. We have not yet used wavelet transform to extract these components. Instead, we analyze points in the wavefields, and use these to retrieve information and to characterize the acoustic phenomenon that is affecting wave propagation through the subsurface.

As follows we present the analysis of the results obtained following the methodology proposed in the previous section with the algorithms presented for the signal analysis in the theoretical framework.

3.4.1. Two-layer model

Figure 3.4, illustrating the simplest change of velocity field in an RTM scheme, demonstrates information retrieval using our proposed methodology.

Figure 3.4 shows scalograms for the same trace from different seismograms, arbitrarily chosen to allow the sources in the experiment to be located in space. Figures 3.4a and 3.4b show high Intensity at almost in the same point in lime. This is because the distance between the source corresponding to seismogram I and the geophone that registered Trace 100 is almost the same as that between the source corresponding to seismogram 7 and the geophone. In Figure 3.4c, the highest intensity occurs at a later lime. This is because the distance from the source corresponding to seismogram 15 and the geophone registering Trace 100 is greater.

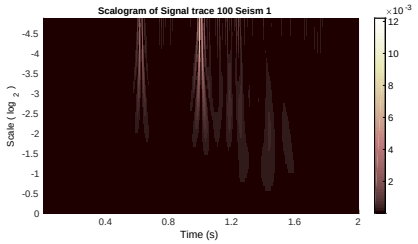

(a) Scalogram Seismogram 1

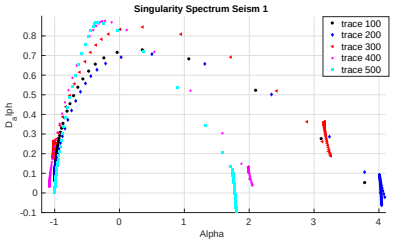

(b) Singularity Spectrum 1

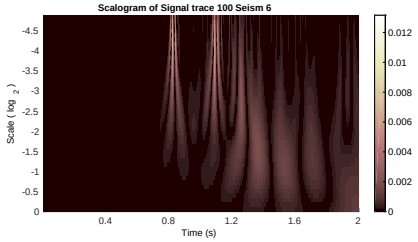

(c) Scalogram Seismogram 6

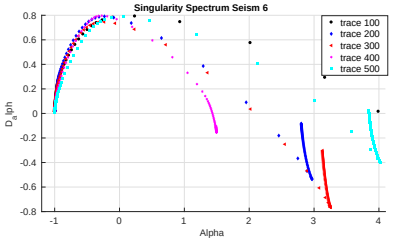

(d) Singularity Spectrum 6

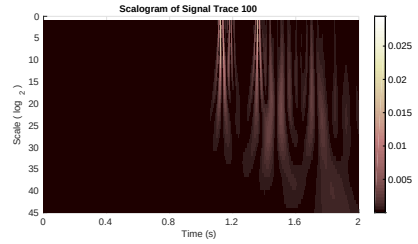

(e) Scalogram Seismogram 10

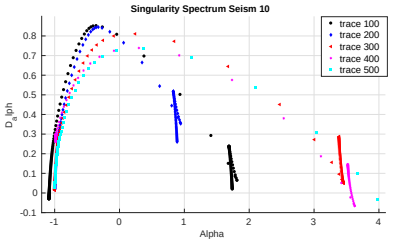

(f) Singularity Spectrum 10

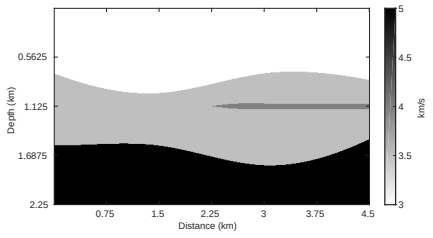

(g) Velocity Model

Figure 3.6: Scalogram of the trace 100 in Seismograms equally separated for the model with a high-velocity intrusion 3.6a Seismogram 1, 3.6c Seismogram 6 and 3.6e Seismogram 10. 3.6b, 3.6d and 3.6f Singularity spectrum for traces 100, 200, 300, 400 and 500 in seismograms 1, 6 and 10, respectively. 3.6g the model with high velocity intrusion

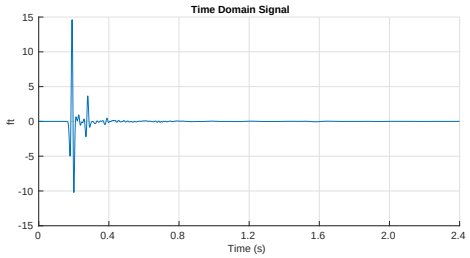

(a) Signal of trace 100

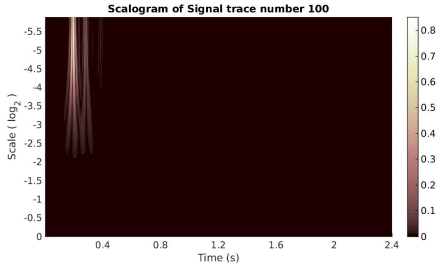

(b) Scalogram Seismogram 1

Figure 3.7: 3.7a Signal $f(t)$ trace number 100 (located ateps $x = 371.25$m) of a seismogram 1 of the RTM for Model small salt (for details see Table 3.1) and its 3.7b Scalogram.

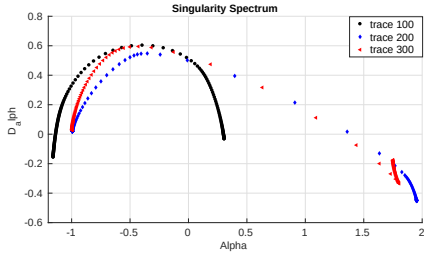

Figure 3.8: Singularity spectrum for three traces (100, 200 and 300) on a seismogram 1 of the data recorded for the small salt model.

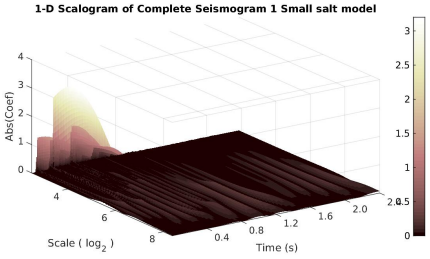

Figure 3.9: Scalogram of a complete seismogram of the data recorded for small salt model. It can be noticed that the values of the coefficients for the summation of the scales is different for the complete seismogram rather than for the scalogram for one single trace.

In the first two cases, the wave travels almost the same distance. In the third case, the wave travels a greater distance.

The continuous wavelet transform, shown as the scalogram of Trace 100 from 3.4a seismogram 1, 3.4b seismogram 7, and 3.4c seismogram 15, demonstrates that the time localization of the main frequency spectrum profiles (at approximately 0.0035 dB) is extended from 0.56 s in 3.4a to 0.84 s in 3.4c. In 3.4b the scale (frequency)

components appear and spread from 0.8 to 1.6 s. These were not detectable In the same trace for localization in 3.4a. This shows the effect that a change in the velocity field has on the frequencies of the wave (Trace 100) propagating through the subsurface, and also demonstrates the capacity of the proposed method to identify small changes in the main frequency component of the traveler wave. However, as can be seen from 3.4c, even when the main mark of the frequency spectrum is present, the new scalogram is unable to provide the full mark of frequencies present in the trace for 3.4b. This demonstrates the capacity of the scalogram to reveal wave transformation when it registers a change in the velocity field, using information on the same signal from different instruments. It provides useful information about the time and features of the scale domain of the propagated wave.

The information retrieved also allows the singularity spectrum of each wave to be calculated via WTMM and a number to be assigned to the frequency features. Figure 3.4b shows the singularity spectra for Traces 100 (black), 200 (blue), and 300 (red) for seismogram 1 3.4d Seismogram 7, and 3.4f Seismogram 15, respectively.

Figure 3.4d shows the singularity spectrum of each trace from seismogram 1. As can be seen, the signal located close to the simulated instrument (Trace 100) is fully described, whereas the algorithm identifies the other signals by a small number of points. This reflects the spatial and temporal information retrieved and is related to the results shown in 3.4c, which give a better representation of the singularity spectrum of the signals. Figure 3.4f shows that the complexity of the waves captured by a certain instrument precludes a proper representation of subsurface features. The geophone is unable to capture sufficient information due to its position relative to the complex subsurface structures. This will degrade the information provided to the RTM algorithm and posterior imaging, creating numerical effects in regions of the image affected by the receiver wavefield.
This demonstrates the way in which an understanding of trace signals in certain regions of the spatial-temporal domain guides the RTM procedure in real applications.

3.4.2. Model with high-velocity intrusion

To improve understanding of the meaning of the singularity analysis of traces, we conducted a similar experiment using a model with a high-velocity intrusion. The velocity field is shown in Figure 3.6. This model had two sources of singularities in the two-dimcnsional function for the velocity field and the possibility that a wave propagating through the field would be reflected.

Figure 3.6 shows scalograms of the same trace from seismograms 1, 6, and 10. The convergence when the two main marks (lightest) showing the principal frequencies of the signal can he observed and their delay through the scalograms is clear. The spread of the scale profile from 1.245 to 2.075 seconds in b) identifies changes in frequency due to multiple reflections or residual reflections caused by incomplete absorption of waves at the boundaries. The fractality of the spectrum also provides clues to the topology of the two-dimensional model.

As can be seen from Figure 3.6b, 3.6d, and 3.6f, in this model Traces 100, 200,

300, 400, and 500 show an interesting singularity spectrum. For example, in the case of Trace 400, captured by the receiver located at $x = 3$ km in Figure 3.6f, the singularity spectrum shows many singularity points. These represent significant frequency changes and suggest proximity to the reflective event, that is located next to the source ($x = 3.68$ km) and immediately above the high-velocity intrusion.

3.4.3. Small salt model

Seismic imaging in and around salt bodies involves pitfalls at every stage of the process. Key challenges are as follows.

- Developing an adequate description of the large scale crystalline structure, rheology, and anisotropy.
- Understanding diagenesis and cap rock formation in salt bodies.
- Interpreting stress-induced effects. This includes changes to the sound speed.
- Acquisition limitations, producing poor illumination or poor sampling.
- The interpretation of time imaging. This is fortunately avoided in depth imaging.
- The complex travel paths associated with seismic arrivals in salt.
- Inappropriate preprocessing.
- Anisotropy representation and parameterization. In many cases, insufficient information (measured data) is available to adequately describe the anisotropic behavior of the subsurface.
- Seismic mode-converted events. Current theory is confined to acoustics [28].

We tested our algorithm on the small salt velocity model described in Table 3.1 and shown in Figure 3.5. One of the challenges of the RTM approach is the fact that certain subsurface formations related to salt diapirs induce strong velocity changes, which create reflective events in wave propagation. Retrieving these by simulation of instruments (geophones) in seismograms from previous algorithms such as Full Wave Inversion, or from real data, does not always provide accurate results.
It is known that artifacts arising in the RTM procedure may be caused by lateral amplitude terminations (localized edge effects) on the string vertical velocity boundaries, from laterally mispositioned double-bounce arrivals. These can arise from significant errors in the anisotropy parameters or from the migration of reflected refractions [28]. Some artifacts may appear as nearly vertical strong a events. These are clearly non-geologic, and are easily suppressed by filtering the RTM prestack angle gathers. Even when artifacts appear, RTM is able to correctly identify the energy traveling on the ray path.

As noted above, the surface signals from a salt body are very complex, due to the nature of the geometry of the body and the change in amplitude of the converted

mode arrivals. This introduces several artifact-generating mechanisms, for example when a reflector meets the salt perpendicularly, or when multiple incident angles generate head wave effects.
Figures 3.5 and 3.7 show examples of such signals, and the scalogram of one. In Figure 3.7, the scalogram shows a single, large scale mark in the signal. The scalogram in Figure 3.5c allows the three main energy profiles at times 0.32, 0.44, and 0.576 s from Trace 300 of seismogram 7 to be observed, localizing it in a central region of the velocity model. "Candle drooling" is a unique feature in the scale profile of a wave signal, indicating at least three changes in the wave frequency at different times. The spatial information about the trace is robust.

It is important to note that energy must not be treated as noise, and that the complexity of a trace signal must be taken into account. If this is not done, the real features of the subsurface may be eliminated from the final image. Figure 3.9 shows the superposition of the full seismogram, which we used to test the algorithm and its capacity to capture the properties of the traveler wave. This was derived by calculating each trace independently then summing the scale components in time.
The complexity of the signal may also convey information about the anisotropy of the salt body. It is therefore recommended that a range of velocities are tested in initial velocity model building for areas in which the evaporate composition is unknown. In RTM, the model is the initial condition, but the real data may suggest the presence of features not considered in the modeling, for example physical phenomena related to the elongation of interbeds with different compositions and mineral grains in the flow direction [29]. In future research we will relate our findings to salt anisotropy, which is not currently incorporated in the models.

Figure 3.8 shows a formalization of the information about the wave presented in terms of its singularity spectrum. The continuous nonlinear spectrum of Trace 300 (red) and the approximately linear behavior of Traces 100 and 200 can be observed. The singularity values shown in red suggest the kind of information to be incorporated into an improved RTM scheme. However, not all the singularities in the signal traversing the salt body can be attributed to the effects of reflection, energy, or anisotropy.

Summary

In this chapter, we described a singularity spectrum algorithm, based on wavelet analysis (WTMM), for extracting the main time-scale features of a signal. We applied this algorithm to the retrieval of information about the receiver wavefield at $z = 0$ by applying a forward wave propagation through different velocity fields.

Our main goal was to use information on the subsurface contained within the signal to understand phenomena related to attenuation and reflection. Our algorithm can be used to characterize the frequency spectrum and to analyze changes in the velocity field and their effect on wave propagation. The frequencies of the traveler wave can be used to enhance the quality of the RTM algorithm through refinement of the solution of the time steps and/or the application of post-processing strategies.

We found that both continuous wavelet analysis and the singularity spectrum allow the understanding of certain regions on the velocity field to be taken into account when applying the RTM procedure. To exemplify our findings, we relate the attenuation or reflection phenomena to the time-scale features, and locate certain salt body seismographic signals. The algorithm quantifies the feature set of the full procedure.

This algorithm can be applied to forward and backward analysis of the wavefields in the RTM procedure. They can be used to map time-space and time-depth features onto the scale domain, and to relate them to the frequency of the signal traveling through the velocity field. In the next chapter, we describe a method that allows to improve the scalar field with uncertainties obtained by RTM and the zero-lag cross-correlation imaging condition.

References

[1] J. G. Paniagua and O. L. Quintero, *Singularity analysis of receiver field and its relation to RTM imaging condition,* Paper submitted to Nature Geoscience (2017).

[2] B. He, D. Tang, Y. He, B. Long, and X. Xie, *The imaging resolution analysis for complex models applied in seismic survey design,* SEG Technical Program Expanded Abstracts , 2051 (2016).

[3] B. A. Bhatti and R. J. Brown, *Low-frequency seismic analysis and direct hydrocarbon indicators,* SEG Technical Program Expanded Abstracts 2016 , 2051 (2016).

[4] R. Bras and G. Mellman, *Wavelets and Their Applications* (Springer Netherlands, 1995) pp. 291–296.

[5] C. Schmelzbach, S. Greenhalgh, F. Reiser, J. Girard, F. Bretaudeau, L. Capar, and A. Bitri, *Advanced seismic processing/imaging techniques and their potential for geothermal exploration,* Interpretation **4**, SR1 (2016).

[6] S. Greenhalgh and E. Manukyan, *Seismic Reflection for Hardrock Mineral Exploration: Lessons from Numerical Modeling,* Journal of Environmental and Engineering Geophysics **18**, 281 (2013).

[7] S. Wei, M. V. DeAngelo, and B. A. Hardage, *Advantages of joint interpretation of P-P and P-SV seismic data in geothermal exploration,* Interpretation **2**, SE117 (2014).

[8] G. J. Hicks and R. G. Pratt, *Reflection waveform inversion using local descent methods: Estimating attenuation and velocity over a gas-sand deposit,* Geophysics **66**, 598 (2001).

[9] M. Malinowski, S. Operto, and A. Ribodetti, *High-resolution seismic attenuation imaging from wide-aperture onshore data by visco-acoustic frequency-*

domain full-waveform inversion, Geophysical Journal International **186**, 1179 (2011).

[10] Z. Ge, Y. Xu, J. Li, X. Chen, B. Wang, Z. Wang, and R. Chen, *Wavelet distortion correction using shaping filter in the generalized S-transform domain,* SEG Technical Program Expanded Abstracts 2016 , 2294 (2016).

[11] J. B. Tary, M. Van der Baan, and R. H. Herrera, *Attenuation estimation using high resolution time–frequency transforms,* Digital Signal Processing **60**, 46 (2017).

[12] R. Zhang and S. Fomel, *Time-variant wavelet extraction with a local-attribute-based time-frequency decomposition for seismic inversion,* Interpretation **5**, SC9 (2017).

[13] V. Venugopal, S. G. Roux, E. Foufoula-Georgiou, and A. Arneodo, *Revisiting multifractality of high-resolution temporal rainfall using a wavelet-based formalism,* Water Resources Research **42**, 1 (2006).

[14] Q. Sun and Y. Tang, *Singularity analysis using continuous wavelet transform for bearing fault diagnosis,* Mechanical Systems and Signal Processing **16**, 1025 (2002).

[15] Z. Peng, F. Chu, and P. W. Tse, *Singularity analysis of the vibration signals by means of wavelet modulus maximal method,* Mechanical Systems and Signal Processing **21**, 780 (2007).

[16] B. Enescu, K. Ito, and Z. Struzik, *Wavelet-Based Multifractal Analysis of Real and Simulated Time Series of Earthquakes,* Annuals of disaster prevention research institute **47** (2004).

[17] A. Arneodo, B. Audit, N. Decoster, J. F. Muzy, and C. Vaillant, *The Science of Disasters: Climate Disruptions, Heart Attacks, and Market Crashes* (Springer Berlin Heidelberg, 2002) Chap. 2, pp. 26–102.

[18] J. R. Macdonald and M. K. Brachman, *Linear-system integral transform relations,* Reviews of modern physics **28**, 393 (1956).

[19] D. Sierra-Sosa, L. Angel-Toro, N. Bolognini, and M. Tebaldi, *Novel vortex-transform for high frequency modulated patterns,* Optics Express **21**, 23706 (2013).

[20] L. Debnath and D. Bhatta, *Integral transforms and their applications* (CRC press, 2010).

[21] S. Jaffard, *Pointwise smoothness, two-microlocalization and wavelet coefficients,* Publicacions Matemátiques **35** (1991).

[22] O. Rioul and M. Vetterli, *Wavelets and signal processing,* IEEE Signal Processing Magazine **8**, 14 (1991).

[23] S. Mallat, *A Wavelet Tour of Signal Processing*, 2nd ed., edited by A. Press (Academic Press, 2009).

[24] I. Daubechies, *Ten Lectures on Wavelets*, CBMS-NSF Regional Conference Series in Applied Mathematics (Society for Industrial and Applied Mathematics, Philadelphia, 1992) pp. 1 – 357.

[25] G. Erlebacher, M. Y. Hussaini, and L. M. Jameson, *Wavelets: Theory and Applications*, 1st ed., edited by G. Erlebacher, M. Y. Hussaini, and L. M. Jameson, ICASE/LaRC Series in Computational Science and Engineering (Oxford University Press, New York, 1996).

[26] S. Mallat and W. Hwang, *Singularity detection and processing with wavelets,* Information Theory, IEEE Transactions on **38**, 617 (1992).

[27] F. Liu, G. Zhang, S. Morton, and J. Leveille, *An effective imaging condition for reverse time migration using wavefield decomposition,* Geophysics **76**, 29 (2011).

[28] I. F. Jones and I. Davison, *Seismic imaging in and around salt bodies,* Interpretation **24**, SL1 (2014).

[29] I. Davison, I. Alsop, and D. Blundell, *Salt tectonics: some aspects of deformation mechanics,* Geological Society, London, Special Publications **100**, 257 (1996).

4

In wavefield separation by continuous wavelet transform

In chapter 2 we described how the uncertanties in RTM are generated. The source and receiver wavefields propagate along a wave path in the same direction in nonreflecting points, and in reflection points, the reflected wavefield propagates in different direction from the incident source wavefield.

This chapter presents a new method that extracts relevant information about the source and receiver wavefields in order to separate the components of these. This wavefield separation is performed by using continuous wavelet transform via WTMM and the Hölder exponent analyzing the signals in a subset of the source and receiver wavefields. The proposed method will allow to obtain a scalar field with high resolution and fidelity, a clear delineation of structures in complex geological areas.

The uncertainties in RTM models are low-frequency noises that only exist in RTM. Such noises result from the unwanted cross-correlation of the source and the receiver wavefields at non-reflecting points along the raypath. In section 2.3 we described how the uncertainties are generated in RTM models and in section 2.3.2 we showed some methods proposed to avoid or reduce these low-frequency uncertainties. Some numerical examples were used to illustrate the uncertainties of RTM models in section 2.4.

One strategy to avoid the uncertainties in RTM that was mentioned in section 2.3.2 is the wavefield decomposition [1, 2, 3]. In this method, the source and receiver wavefields are decomposed in their one-way components along a certain specific direction in order to correlate the appropriate combinations of some of these decomposed wavefields. When the components of the source and receiver wavefields that propagate in opposite directions are correlated, it produces a model of the subsurface structures. The cross-correlation of decomposed source and receiver wavefields that propagate in parallel directions will not generate a model because one of them will be zero.

In chapter 3, we proposed the use of the capability of the continuous wavelet transform and the singularity spectrum to analyze seismic traces, that is, the receiver wavefield at $z = 0$ $(r(x,t))$ in order to extract relevant information that allows to identify the frequency changes of the wave while it travels through the media.

Taking into account the concepts developed in sections 3.1.2, 3.1.3, 3.1.4 and 3.2, we propose a new way to extract information from the source and receiver wavefields based on the analysis of the time-scale or time-frequency characteristics, using WTMM via wavelet continuous transform and the exponent of holder. The aim is to reduce the uncertainty in models obtained through RTM and the ZL-CC-IC correlating some specific information of the components of both wavefields.

4.1. Wavefield decomposition

From eq. 1.1, let $S(\mathbf{x},t)$ and $R(\mathbf{x},t)$ be the source and receiver wavefield, respectively. $S(\mathbf{x},t)$ and $R(\mathbf{x},t)$ can be partitioned mathematically as

$$S(\mathbf{x},t) = S_d(\mathbf{x},t) + S_u(\mathbf{x},t) \tag{4.1}$$

$S_d(\mathbf{x},t)$ and $S_u(\mathbf{x},t)$ are subsets of $S(\mathbf{x},t)$, called downgoing and upgoing source wavefields, respectively.

And

$$R(\mathbf{x},t) = R_d(\mathbf{x},t) + R_u(\mathbf{x},t) \tag{4.2}$$

$R_d(\mathbf{x},t)$ and $R_u(\mathbf{x},t)$ are subsets of $R(\mathbf{x},t)$, called downgoing and upgoing receiver wavefields, respectively.

Taking into account eq. (2.17) and replacing eq. (4.1) and eq. (4.1), the zero-lag cross-correlation imaging condition can be expressed as follows

$$I(\mathbf{x}) = \sum_{j=1}^{s_{max}} \sum_{i=1}^{t_{max}} \Big[S_d(\mathbf{x}; t_i; s_j) R_u(\mathbf{x}; t_i; s_j) + S_u(\mathbf{x}; t_i; s_j) R_d(\mathbf{x}; t_i; s_j) + S_d(\mathbf{x}; t_i; s_j) R_d(\mathbf{x}; t_i; s_j) + S_u(\mathbf{x}; t_i; s_j) R_u(\mathbf{x}; t_i; s_j) \Big] \quad (4.3)$$

Then,

$$I(\mathbf{x}) = I_{du}(\mathbf{x}) + I_{ud}(\mathbf{x}) + I_{dd}(\mathbf{x}) + I_{uu}(\mathbf{x}) \quad (4.4)$$

Based on [1] and [2], $I_{dd}(\mathbf{x})$ and $I_{uu}(\mathbf{x})$ are the cross-correlation of the two wavefields that propagate in the same direction downgoing (I_{dd}) or upgoing (I_{uu}) and generate the uncertainties in the RTM model.
Thus, the wavefield decomposition cross-correlation imaging condition can be formulated by keeping only the first two terms as follows

$$I(\mathbf{x}) = \sum_{j=1}^{s_{max}} \sum_{i=1}^{t_{max}} \Big[S_d(\mathbf{x}; t_i; s_j) R_u(\mathbf{x}; t_i; s_j) + S_u(\mathbf{x}; t_i; s_j) R_d(\mathbf{x}; t_i; s_j) \Big] \quad (4.5)$$

From eq. (4.4), we have

$$I_{ud}(\mathbf{x}) = S_d(\mathbf{x}; t_i; s_j) R_u(\mathbf{x}; t_i; s_j) \quad (4.6)$$

which is the cross-correlation of the downgoing source and upgoing receiver wavefields that is exactly what one will get in one-way wave-equation migration.
In the followings sections we propose a new method to wavefield separation based on the continuous wavelet transform and singularity analysis via maximum modulus wavelet transform in order to obtain models with high resolution and fidelity, and a clear delineation of structures.

4.2. Analysis of source and receiver wavefields

In order to illustrate how we extract information about the source and receiver wavefields via singularity analysis and continuous wavelet transform, we apply the RTM algorithm using a velocity model depicted in Figure 2.3.
We use only one source point located at $x = 1.5$ Km from the beginning of the surface. There are 400 receivers equally distributed along the surface and the receiver interval is 7.5 m.
Figure 4.1 shows some snapshots on the source and receiver wavefields, $S(x, z, t)$ and $R(x, z, t)$, respectively. The first column corresponds to the source wavefield and the second column to the receiver wavefield. The first row is at $t = 0.2$ s and the second row is at $t = 0.36$ s.
We can see that some parts of the both wavefields spatially coincide at the same time.

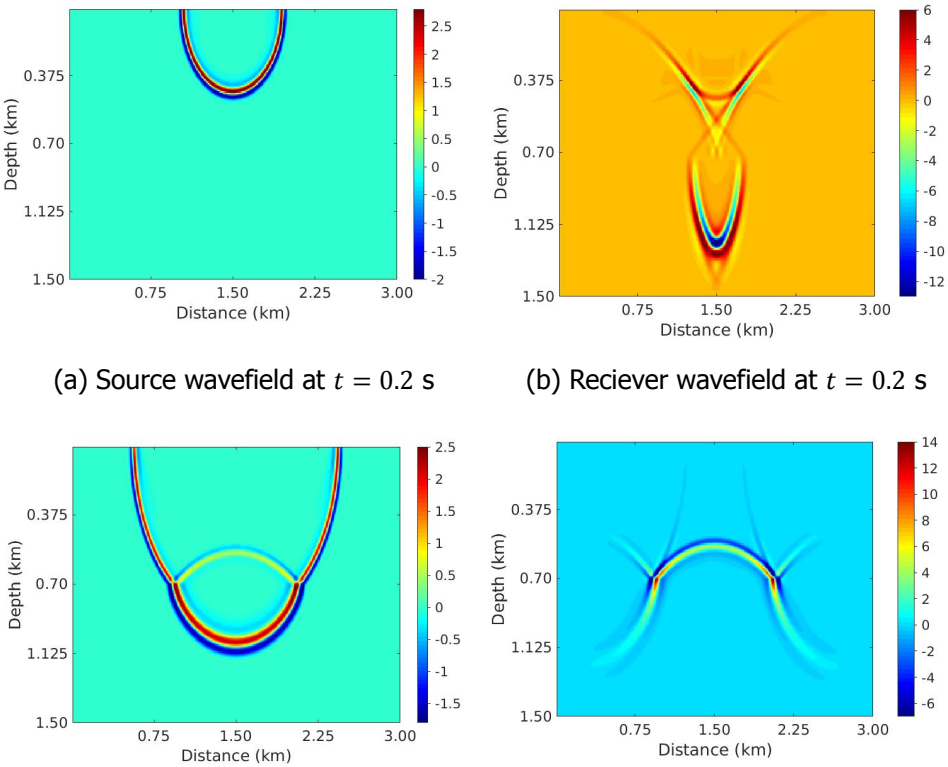

(a) Source wavefield at $t = 0.2$ s

(b) Reciever wavefield at $t = 0.2$ s

(c) Source wavefield at $t = 0.36$ s

(d) Reciever wavefield at $t = 0.36$ s

Figure 4.1: Snapshots of source wavefield 4.1a and 4.1c and receiver wavefield 4.1b and 4.1d

The migrated model obtained by RTM algorithm and the ZL-CC-IC is shown in Figure 4.2.

We can see that the model is contaminated with low frequency artifacts above and near the reflective event and in the shallow parts. The arrows indicate noises with strong energy, wide frequency band, low apparent frequency, and specific distribution along the propagation path of the seismic wave.

To avoid these low-frequency artifacts, Fei et al. (2010) [2] proposed a De-blending RTM algorithm to decompose the source and receiver wavefields into upgoing and downgoing wavefields and compare the images obtained by cross-correlation of different combinations of these wavefields. Liu et al. (2011) [1] proposed the wavefield separation cross-correlation imaging condition to suppress the artifacts. In this method, the source and receiver wavefield are decomposed in upgoing and downgoing directions using the 2D Fourier transform. Chen and He (2014) [3] used the Poynting vector to the separate the wavefields in the up-going, down-going, left-going, and right-going waves and applied the normalized wavefield separation

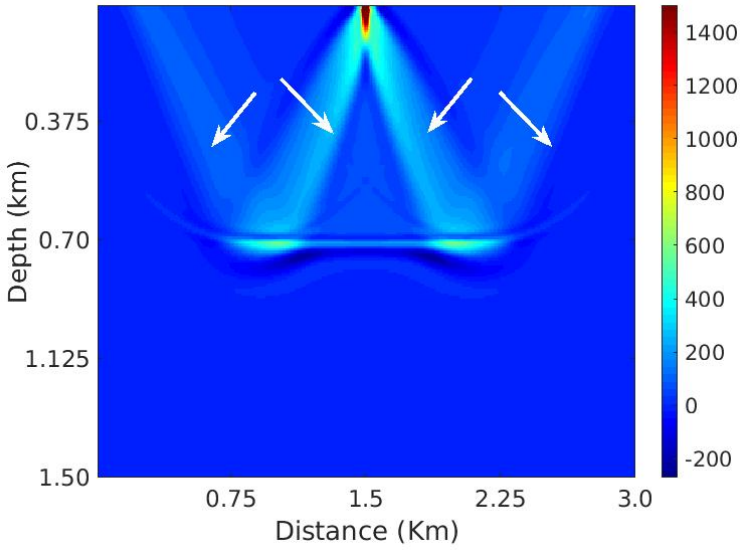

Figure 4.2: Cross-correlation scalar field of two-layer velocity field

cross-correlation imaging condition.
In next sections, we will describe the methodology to perform a time-scale analysis of the source and receiver wavefields to extract relevant information of them in order to correlate specific components of the wavefields in the ZL-CC-IC.

4.3. Time scale wavefield separation (TSWS)

Let $S(x,z,t)$ and $R(x,z,t)$ be the source and receiver wavefields described in section 2.2 and they are obtained as was illustrated in section 2.1.1 and 2.1.2. Let $S(x,z,t_i)$ and $R(x,z,t_i)$ be subsets of $S(x,z,t)$ and $R(x,z,t)$, respectively, for an arbitrary value of $t = t_i$.
We made a time-scale analysis on these subsets of the source and receiver wavefields by using CWT. Initially, we analyzed the subsets $S(x,z,t_i)$ of the source wavefield and the subsets $R(x,z,t_i)$ of the receiver wavefield for each time step $t = t_i$ to separate the downgoing and upgoing components using CWT.

Figure 4.3 shows a representation of some subsets of the source wavefield in a fixed value of t of the two-layer velocity field depicted in Figure 2.3. The subsets $S_u(x,z,t)$ and $S_d(x,z,t)$ that are the components of the source wavefield are marked with arrows.
Let $S(x_i,z,t_i)$ and $R(x_i,z,t_i)$ be subsets of $S(x,z,t_i)$ and $R(x,z,t_i)$, respectively, for an arbitrary value of $x = x_i$ and, let $S(x,z_i,t_i)$ and $R(x,z_i,t_i)$ be subsets of $S(x,z,t_i)$ and $R(x,z,t_i)$, respectively, for an arbitrary value of $z = z_i$.

We applied the one dimensional continuous wavelet transform in the direction of

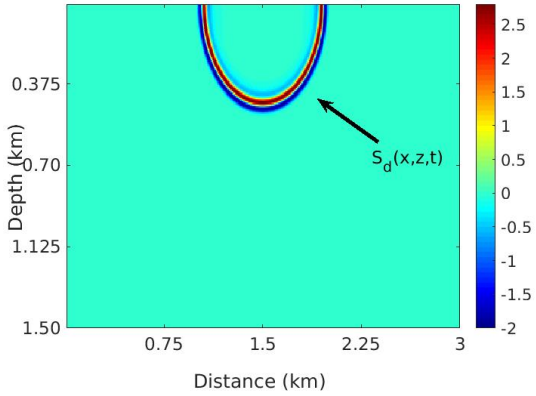

(a) Subset of the source wavefield at $t = 0.2$ s

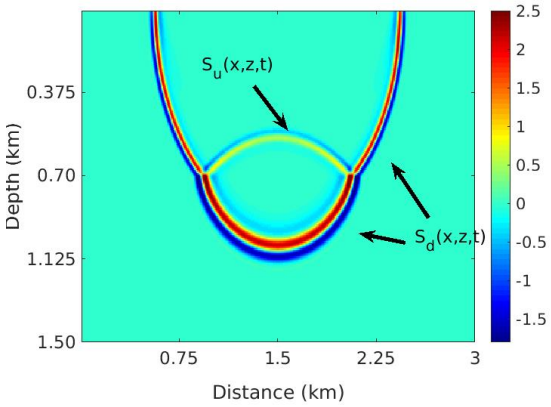

(b) Subset of the source wavefield at $t = 0.36$ s

Figure 4.3: Snapshots of source wavefield at 4.3a $t = 0.2$ s and 4.3b $t = 0.36$ s.

x-axis and z-axis, that is, the CWT was applied for all subsets $S(x_i, z, t_i)$, $R(x_i, z, t_i)$ for each value of $x = x_i$, and for all subsets $S(x, z_i, t_i)$, $R(x, z_i, t_i)$ for each value of $z = z_i$.

The scalogram and the value of coefficients were analyzed in order to find common characteristics between the coefficients and signals corresponding to the downgoing and upgoing components of the wavefields. However, we could not separate the components of wavefields since it was not possible to find specific characteristics that allowed to do it.

Then, we applied the CWT to the source and receiver wavefields for a fixed value in x-axis, that is, we used the subsets $S(x_i, z, t)$ which will be denoted by $S_{x_i}(z, t)$ and $R(x_i, z, t)$ which will be denoted by $R_{x_i}(z, t)$ of the source and receiver wavefields for

a fixed $x = x_i$ value (For each value $x = x_i$ the wavefields $S_{x_i}(z,t)$ and $R_{x_i}(z,t)$ were analyzed by applying the 1D CWT) and we found some common characteristics of the coefficients obtained by CWT and the components of wavefields.
Figure 4.4 shows a representation of the subsets $S_{x_i}(z,t) = S(x_i,z,t)$ and $R_{x_i}(z,t) = R(x_i,z,t)$ of the source wavefield $S(x,z,t)$ and receiver wavefield $R(x,z,t)$ for an arbitrary value $x = x_i$. The downgoing and upgoing components of these wavefields, denoted by $S^d_{x_i}(z,t)$, $S^u_{x_i}(z,t)$ and $R^d_{x_i}(z,t)$, $R^u_{x_i}(z,t)$ are marked with arrows.

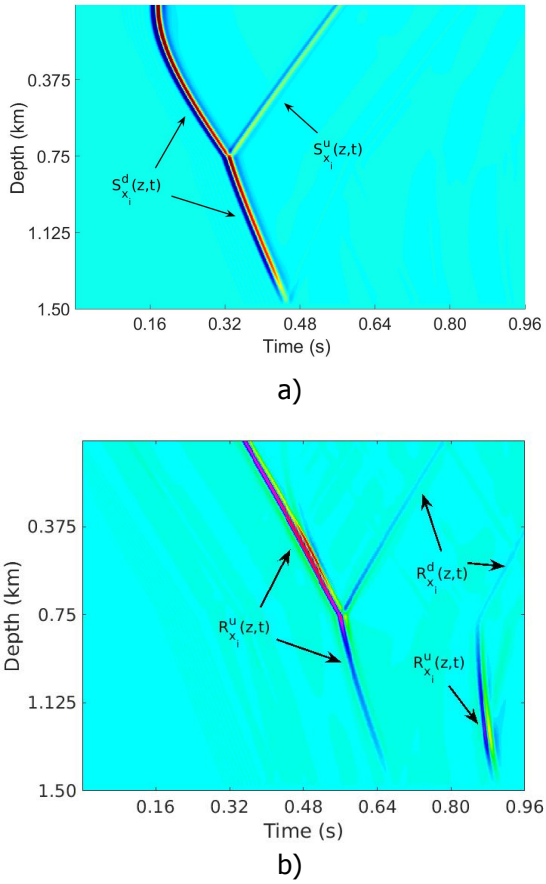

Figure 4.4: Subsets of a) source wavefield $S(x,z,t)$ at $x = 1.125$ km and b) receiver wavefield $R(x,z,t)$ at $x = 2.625$ km.

For each value in x-axis, we found a similar structure in subsets of the source wavefield, denoted $S_{x_i}(z,t)$ and in subsets of the receiver wavefield, denoted $R_{x_i}(z,t)$.
Next, the scheme used for the time-scale analysis of each wavefield (TSWS) is described as follows. It was used the source and receiver wavefields obtained by RTM of the two-layer model depicted in Figure 2.3. In addition, some partial results

are shown when applying the scheme in this model.

4.3.1. Analysis of the source wavefield $S(x,z,t)$

The methodology used to perform the time-scale analysis of the source wavefield $s(x,z,t)$ is the following:

1. With the source wavefield $S(x,z,t)$, select for each $x = x_i$ the subset $S(x_i,z,t)$, denoted by $S_{x_i}(z,t)$ (Defined in section 4.3).

2. Apply the $1D$ CWT on the subset $S_{x_i}(z,t)$ with a fixed value of $z = z_i$ denoted by $S_{x_i,z_i}(t)$ in order to obtain the scalogram of the signal. That is, for a fixed $x = x_i$ and $z = z_i$, $S_{x_i,z_i}(t) = S(x_i,z_i,t)$, then by $1D$ CWT of $S_{x_i,z_i}(t)$ (See definition 3.1.1), we obtain the field $\hat{S}_{x_i,z_i}(u,s) = W(S_{x_i,z_i}(t))$ and the scalogram of the signal is obtained. $\hat{S}_{x_i,z_i}(u,s)$ is the CWT of $S_{x_i,z_i}(t)$.

3. Select the minimum value of the all coefficients for all scales in $\hat{S}_{x_i,z_i}(u,s)$ and locate it in $S_{x_i,z_i}(t)$ and saved in a new source wavefield $S_{new}(x,z,t)$ for $x = x_i$ and $z = z_i$, that is a subset of the source wavefield $S(x,z,t)$ and corresponds to a subset of the downgoing component of the source wavefield $S_d(x,z,t)$. Two more points were taken before and after this point to improve the accuracy.

Next, a flux diagram of the methodology proposed above is shown in Figure 4.5

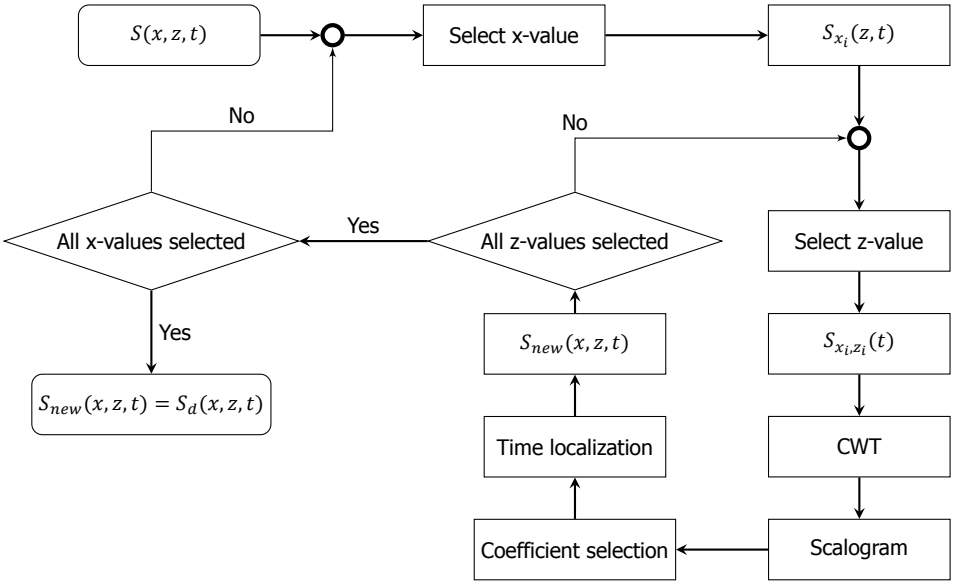

Figure 4.5: Methodology diagram of source wavefield analysis

Following the proposed methodology to analyze the source wavefield, with a fixed

value of $x = x_i$, the $S_{x_i}(z,t)$ wavefield is obtained from the $S(x,z,t)$ wavefield. Figure 4.6 shows the $S_{x_i}(z,t)$ wavefield from an arbitrarily chosen value of x.

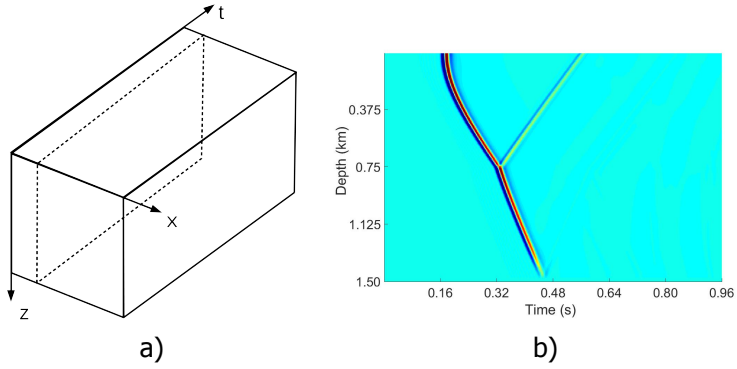

Figure 4.6: Selection of the wavefield to be processed a) Scheme of the $S(x,z,t)$ wavefield with a section in a fixed value of $x = x_i$ b) $S_{x_i}(z,t)$ wavefield at $x = 1.125$ km

Figure 4.7 shows a $S_{x_i}(z,t)$ wavefield at different values of $x = x_i$. The upgoing ($S^u_{x_i}(z,t)$) and downgoing ($S^d_{x_i}(z,t)$) wavefields are marked with arrows.
For each value in $z = z_i$ axis, the CWT is performed on the $S_{x_i,z_i}(t)$ wavefield.
Figure 4.8 shows the signal and its corresponding coefficients obtained by CWT of $S_{x_i,z_i}(t)$.
Analyzing the obtained scalograms, the minimum value of the all coefficients corresponds to the downgoing wavefield. This coefficient is selected and located in the time signal $S_{x_i,z_i}(t)$ taking into account the delay of the signal in time. This point is saved in a new wavefield $S_{new}(x,z,t)$. To improve the accuracy, two more points were taken before and after this point and saved in $S_{new}(x,z,t)$ too. This process is repeated until you get the whole wavefield $S_{new}(x,z,t)$. This is the source wavefield of the incident wave (Downgoing source wavefield).
Figure 4.9 shows the wavefield separation of the source wavefield in downgoing and upgoing components. Figure 4.9a) corresponds to the complete source wavefield and Figure 4.9b) is the obtained downgoing source wavefield by the algorithm described above.

4.3.2. Analysis of receiver wavefield $R(x,z,t)$

The methodology used to perform the time-scale analysis of the Receiver wavefield is the following:

1. With the receiver wavefield $R(x,z,t)$, select for each $x = x_i$ the subsets $R(x_i,z,t)$ of $R(x,z,t)$, denoted by $R_{x_i}(z,t)$.

2. Apply the $1D$ CWT on the subset $R_{x_i}(z,t)$ with a fixed value $t = t_i$ denoted $R_{x_i,t_i}(z)$ in order to obtain the scalogram of the signal. That is, for a fixed $x = x_i$ and $t = t_i$, $R_{x_i,t_i}(z) = R(x_i,z,t_i)$, then, by $1D$ CWT of $R_{x_i,t_i}(z)$ (See

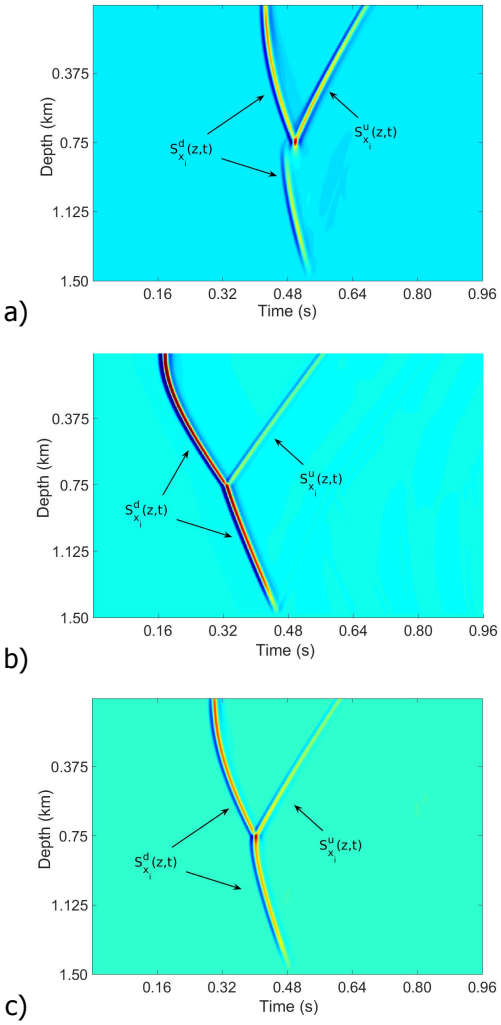

Figure 4.7: $S_{x_i}(z,t)$ wavefield at a) $x = 0.375$ km b) $x = 1.125$ km c) $x = 2.25$ km

definition 3.1.1), we obtain the field $\hat{R}_{x_i,t_i}(u,s) = W(\hat{R}_{x_i,t_i}(t))$ and the scalogram of the signal is obtained. $\hat{R}_{x_i,t_i}(u,s)$ is the CWT of $\hat{R}_{x_i,t_i}(t))$.

3. Select the maximum absolute value of coefficients that corresponds to a coefficient with negative value for all scales in $\hat{R}_{x_i,t_i}(u,s)$ and locate it in $R_{x_i,t_i}(z)$ and saved in a new receiver wavefield $R_{new}(x,z,t)$ for $x = x_i$ and $t = t_i$, that is a subset of the receiver wavefield $R(x,z,t)$ and corresponds to a subset of the upgoing component of the receiver wavefield $R_u(x,z,t)$. Two more points were taken before and after this point to improve the accuracy.

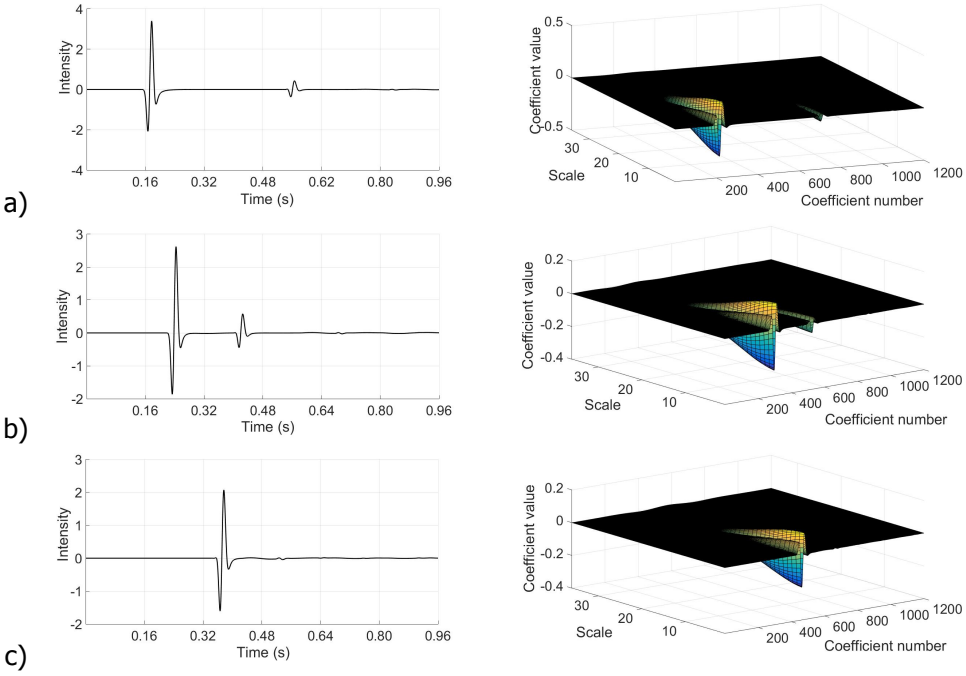

Figure 4.8: Signal $S_{x_i,z_i}(t)$ and coefficients of CWT at $x = 1.125$ km and a) $z = 0$ km b) $z = 0.45$ km c) $z = 1.05$ km

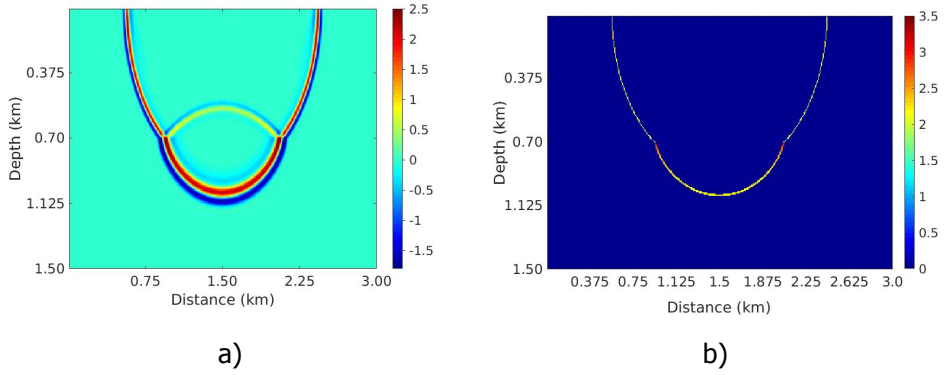

Figure 4.9: Downgoing separation wavefield results of the two-layer model. a) Snapshot when $t = 0.36$ s b) downgoing wave snapshot

Next, a flux diagram of the methodology can be found in Figure 4.10

Following the proposed algorithm to analyze the receiver wavefield, with a fixed value of $x = x_i$, the $R_{x_i}(z,t)$ wavefield is obtained from the $R(x,z,t)$ wavefield. Figure 4.11 shows the $R_{x_i}(z,t)$ wavefield from an arbitrarily chosen value of $x = x_i$.

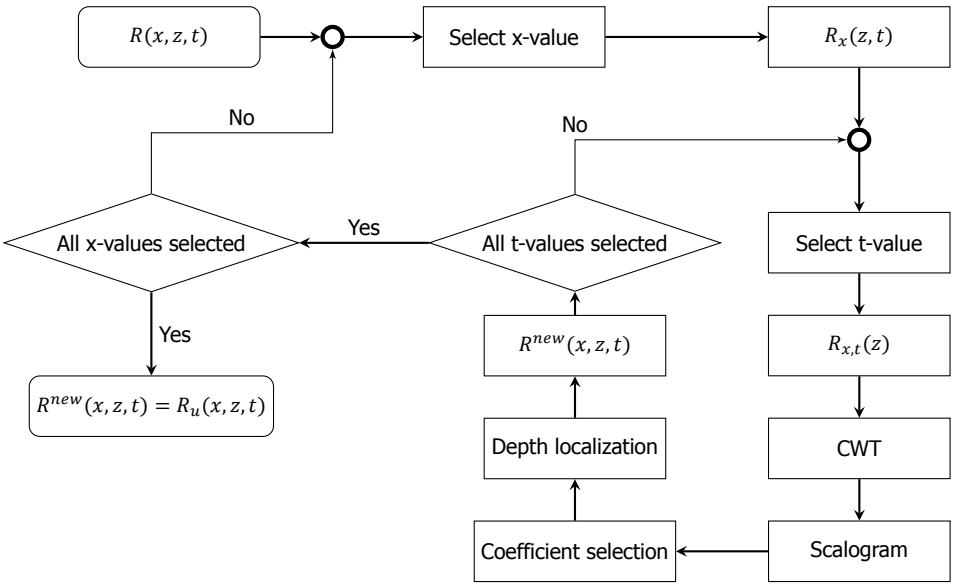

Figure 4.10: Methodology diagram of receiver wavefield analysis

Figure 4.12 shows a $R_{x_i}(z,t)$ wavefield at different values of $x = x_i$. The upgoing

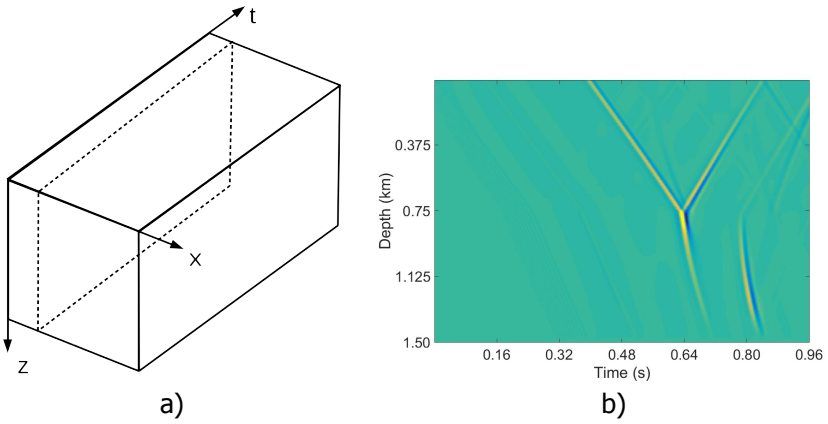

Figure 4.11: Selection of wavefield to be processed a) Scheme of the $R(x,z,t)$ wavefield with a section in a fixed value of x b) $R_{x_i}(z,t)$ wavefield at $x = 1.125$ km

($R^u_{x_i}(z,t)$) and downgoing ($R^d_{x_i}(z,t)$) wavefields are marked with arrows.
For each value in $t = t_i$, the CWT is performed on the $R_{x_i,t_i}(z)$ wavefield. Figure 4.13 shows the signal and its corresponding coefficients obtained by CWT of $R_{x_i,t_i}(z)$. Analyzing the obtained scalograms, the maximum absolute value of coefficients corresponds to a coefficient with negative value. This coefficient is selected and

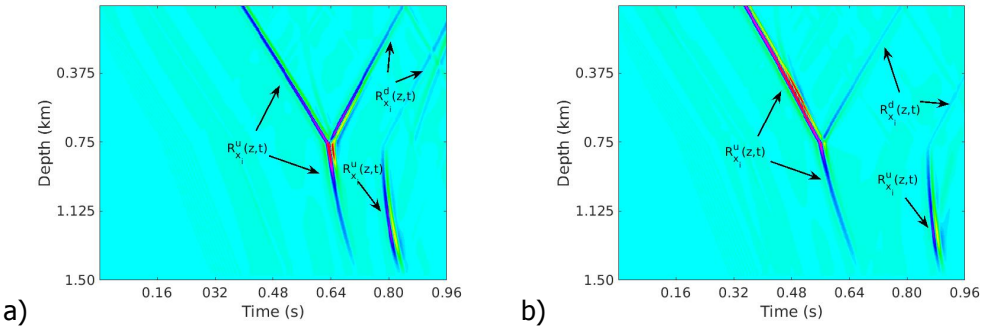

Figure 4.12: $R_{x_i}(z,t)$ wavefield at a) $x = 1.125$ km b) $x = 2.25$ km

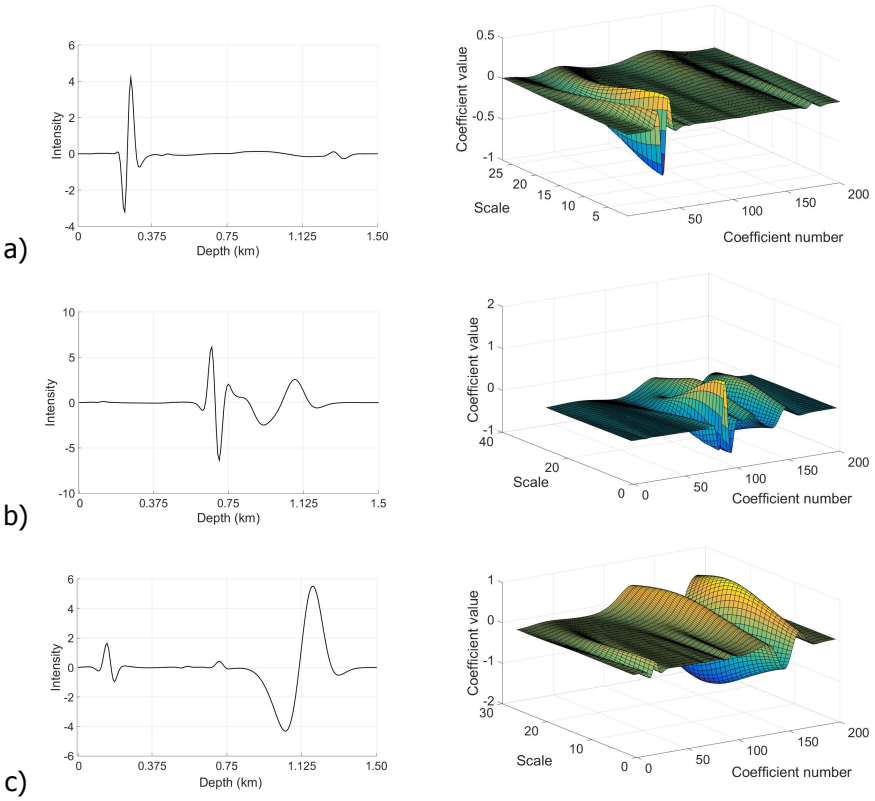

Figure 4.13: Signal $R_{x_i,t_i}(z)$ and coefficients of CWT at $x = 1.125$ km and a) $t = 0.48$ s b) $t = 0.66$ s c) $t = 0.80$ s.

located in the time signal $R_{x_i,t_i}(z)$ taking into account the delay of the signal in time. This point is saved in a new wavefield $R_{new}(x,z,t)$. To improve the accuracy,

two more points were taken before and after this point and saved in $R_{new}(x,z,t)$ too. This process is repeated until you get the whole wavefield $R_{new}(x,z,t)$. This is the receiver wavefield of the incident wave (Upgoing receiver wavefield).
Figure 4.14 shows the wavefield separation of the receiver wavefield in downgoing and upgoing components in a specific time value. Figure 4.14a) corresponds to the complete receiver wavefield and Figure 4.14b) is the obtained upgoing wavefield by the algorithm described above.

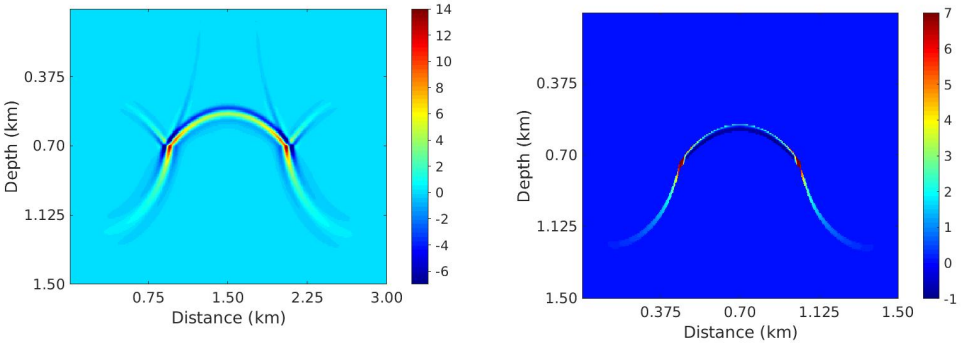

a) b)

Figure 4.14: Upgoing separation wavefield results of the two-layer velocity model. a) Snapshot when $t = 0.36$ s b) upgoing wave snapshot

4.4. Cross-correlation imaging condition using wavefield separation

Equation (4.6) is used to obtain the cross-correlation model. Figure 4.15 shows the scalar field of the velocity model in Figure 2.3 using a proposed method.

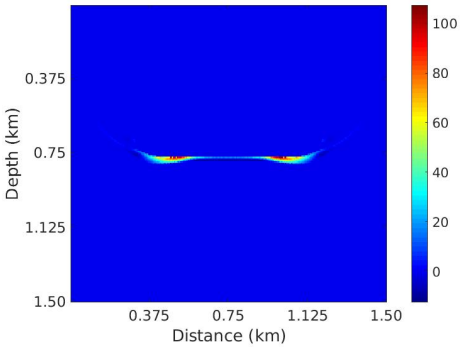

Figure 4.15: Cross-correlation image of two-layer model with wavefield separation

In Figure 4.16 a comparison between models obtained by using a conventional

cross-correlation imaging condition and using the proposed method is shown. As it can be seen the migration noises marked with arrows in Figure 4.16a) are removed (Figure 4.16b)).

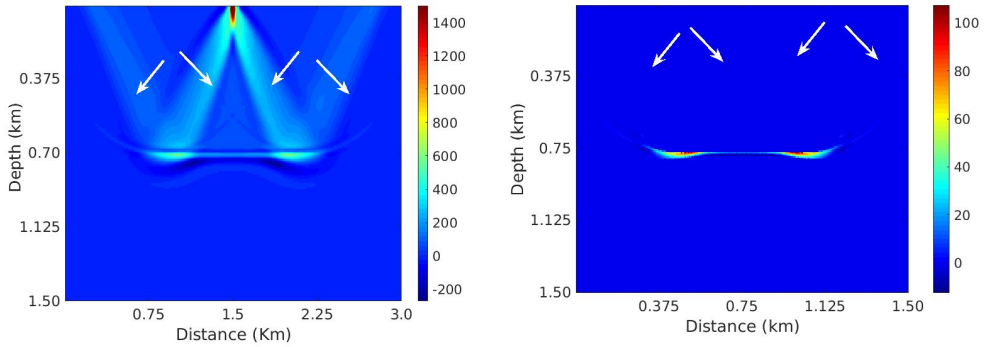

a) b)

Figure 4.16: Comparison of migration results of the two-layer models using a) the conventional cross-correlation imaging condition b) the proposed method

4.5. Application of the method to other synthetic datasets

The proposed method was applied to others synthetic datasets. These datasets are shown in Figure 4.17. Figure 4.17a) corresponds to a homogeneous three-layer velocity field and Figure 4.17b) is a velocity field with small salt diapir.

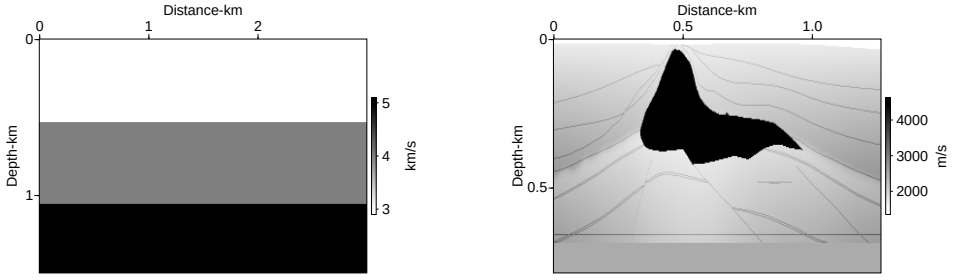

a) b)

Figure 4.17: Synthetic velocity models a) Three-layer velocity field b) Small salt velocity field

Three-layer velocity field has a horizontal distance of 3.0 km and vertical distance of 1.5 km. Small salt model has a horizontal distance of 1.27 km and vertical distance of 0.79 km. For each model one shot point is used located in the middle of the model on the surface. Three-layer model contains 400 receivers and the receiver

interval is 7.5 m, and the small salt contains 210 receivers and the receiver interval is 3.75 m.
When the proposed method is applied on both models, information about the downgoing component of the source wavefield can be extracted adequately. The extraction of information about the upgoing component of the receiver wavefield is being studied and the characteristics obtained through the CWT and WTMM are analyzed. Next, the preliminary results obtained by applying equation (4.6) using the extracted source wavefield, $S_d(x,z,t)$, and the receiver wavefield, $R(x,z,t)$, for the models in Figure 4.17 are shown.

4.5.1. Three-layer velocity model

Figure 4.18 shows the $S_{x_i}(z,t)$ wavefield at different values of $x = x_i$. The upgoing and downgoing components of the source wavefield $S^u_{x_i}(z,t)$ and $S^d_{x_i}(z,t)$, respectively, are marked with arrows.

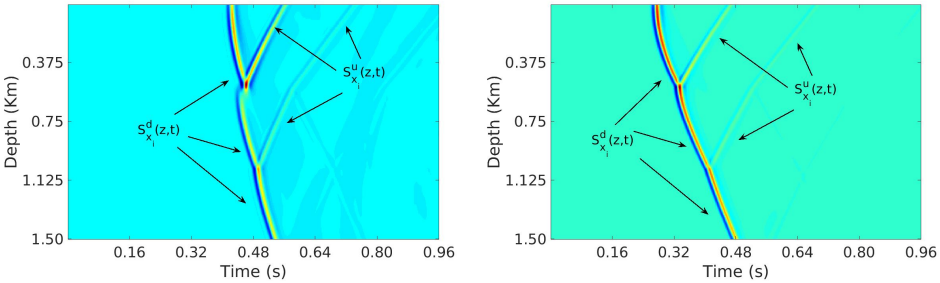

(a) $S_{x_i}(z,t)$ at $x = 0.375$ Km (b) $S_{x_i}(z,t)$ at $x = 0.825$ Km

Figure 4.18: Subsets of the source wavefield. 4.18a, 4.18b subsets $S_{x_i}(z,t)$ of the source wavefield, at $x = 0.375$ Km and $x = 0.825$ Km ,respectively.

Figure 4.19 shows the coefficients obtained by CWT of the subset $S_{x_i,z_i}(t)$ at an arbitrary value of $x = x_i$ and $z = z_i$.
Analyzing the obtained scalograms, we noted the same behavior in the value of the coefficients of the CWT on the subsets $S_{x_i,z_i}(t)$, that is, the minimum value of the all coefficients corresponds to the downgoing wavefield. We did the same procedure described in section 4.3.1.
A snapshot of a source wavefield and the downgoing component of the source wavefield obtained by the proposed method are shown in Figure 4.20. The proposed algorithm has a good behavior and allow to find the $S_d(x,z,t)$ wavefield.
Using only the downgoing component of the source wavefield, $S_d(x,z,t)$, the receiver wavefield, $R(x,z,t)$, and applying equation (2.17), a improved scalar field is obtained, that is, the artifacts in some regions are reduced compared with scalar field obtained with the conventional cross-correlation imaging condition. Figure 4.21 shows a comparison between scalar fields obtained by using a conventional cross-correlation imaging condition and the proposed method with the cross-correlation

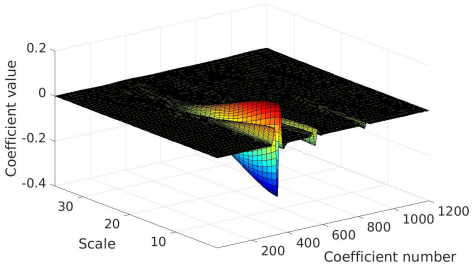

(a) $x = 0.825$ Km and $z = 0.075$ Km

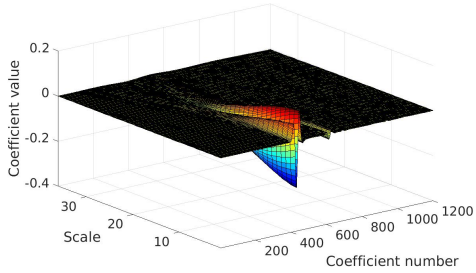

(b) $x = 0.825$ Km and $z = 0.675$ Km

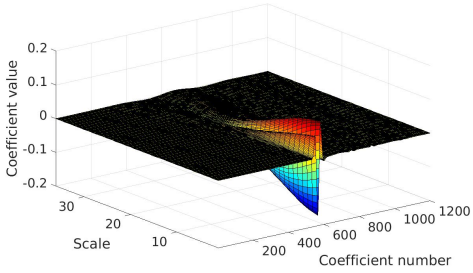

(c) $x = 0.825$ Km and $z = 1.35$ Km

Figure 4.19: Coefficients of the CWT of the subset $S_{x_i,z_i}(t)$ at $x = 0.825$ Km and 4.19a at $z = 0.075$ Km, 4.19b at $z = 0.675$ Km and 4.19c $z = 1.35$ Km.

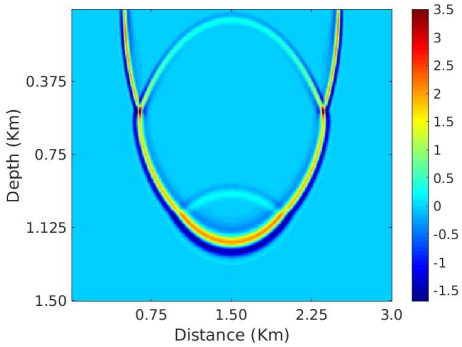

a)

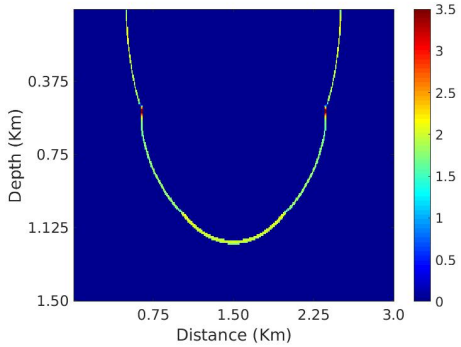

b)

Figure 4.20: Downgoing separation wavefield results of the three-layer model. a) Snapshot when $t = 0.384$ s b) downgoing wave snapshot when $t = 0.384$ s

between $S_d(x,z,t)$ and $R(x,z,t)$ wavefields. We can be noted that the artifacts marked with arrows are removed.

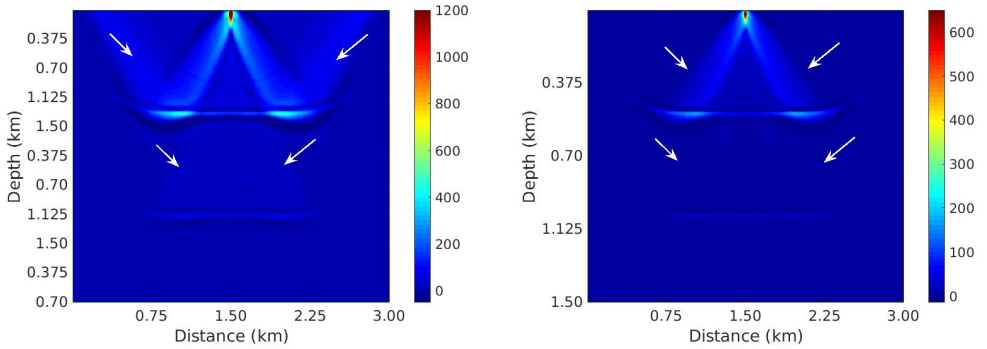

Figure 4.21: Comparison of migration results of the three-layer model using a) the conventional cross-correlation imaging condition b) the proposed method using only the separated source wavefield

4.5.2. Small salt velocity field

The scheme applied to the three-layer model is also applied to the small salt velocity field. Figure 4.22 shows the $S_{x_i}(z,t)$ wavefield at different values of $x = x_i$. Comparing with other velocity field, the behavior in the subsets $S_{x_i}(z,t)$ at $x = x_i$ is similar.

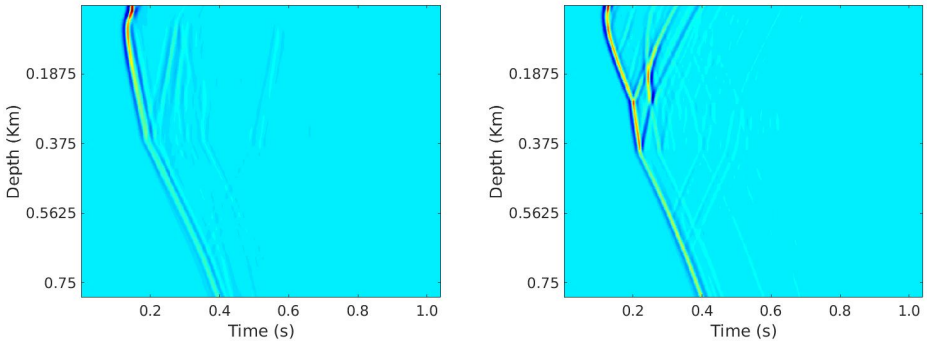

(a) $S_{x_i}(z,t)$ at $x = 0.375$ Km (b) $S_{x_i}(z,t)$ at $x = 0.75$ Km

Figure 4.22: Subsets of the source wavefield. 4.22a, 4.22b subsets $S_{x_i}(z,t)$ of the source wavefield, at $x = 0.375$ Km and $x = 0.75$ Km ,respectively.

Figure 4.23 shows the coefficients obtained by CWT of the subset $S_{x_i,z_i}(t)$ at an arbitrary value of $x = x_i$ and $z = z_i$.

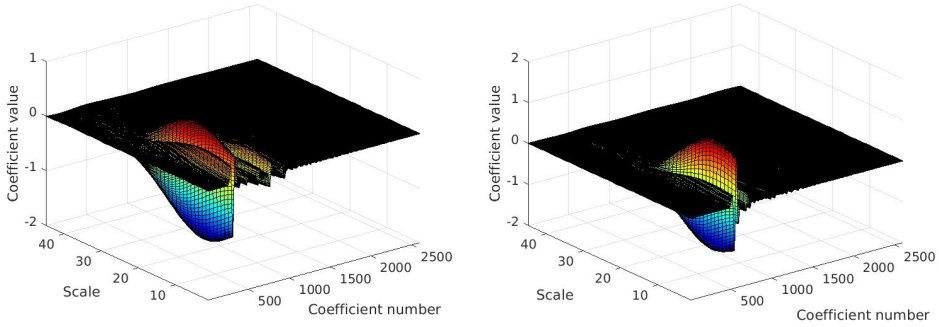

(a) $x = 0.75$ Km and $z = 0.0375$ Km (b) $x = 0.825$ Km and $z = 0.375$ Km

Figure 4.23: Coefficients of the CWT of the subset $S_{x_i,z_i}(t)$ at $x = 0.75$ Km and 4.23a at $z = 0.0375$ Km and 4.23b at $z = 0.375$ Km.

Figure 4.24 shows a snapshot of a source wavefield and the downgoing component of the source wavefield obtained by the proposed method.

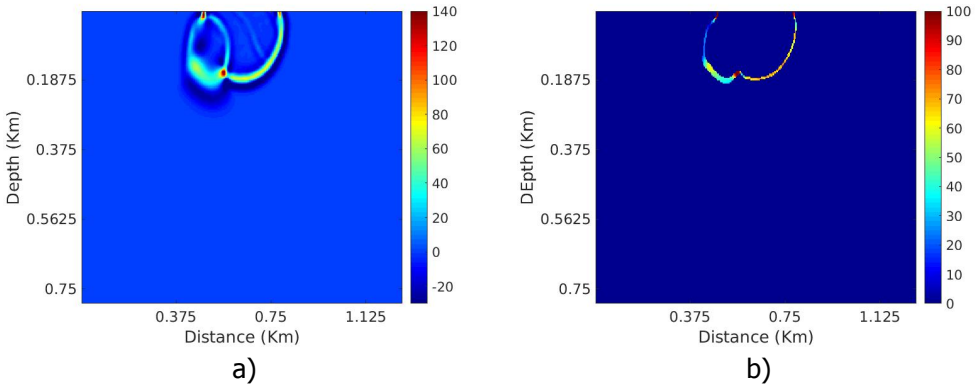

Figure 4.24: Downgoing separation wavefield results of the small salt model. a) Snapshot when $t = 0.15$ s b) downgoing wave snapshot when $t = 0.15$ s

Figure 4.25 shows a comparison between images obtained by using a conventional cross-correlation imaging condition and the proposed method with the cross-correlation between $S_d(x,z,t)$ and $R(x,z,t)$ wavefields.

We can be noted that the artifacts are removed in some regions and the scalar field is improved. The low-frequency uncertainties were reduced in the shallow parts of the scalar field and close to the flanks of the salt body.

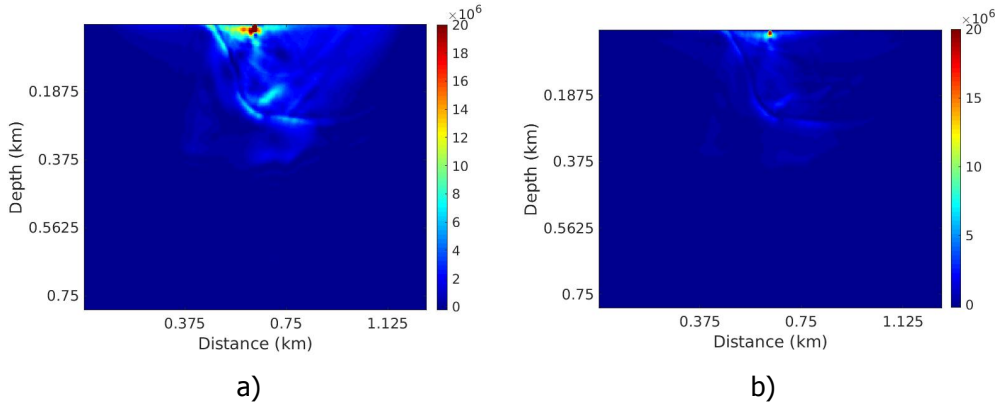

Figure 4.25: Comparison of migration results of the small salt model using a) the conventional cross-correlation imaging condition b) the proposed method using only the separated source wavefield

Summary

In this chapter, we proposed the use of the CWT to extract relevant information about the source and receiver wavefields in order to separate the component of these wavefields. We showed that the method has a good behavior and reduce considerably the uncertainties in scalar fields obtained by RTM. A modification of the ZL-CC-IC was used. This modified imaging condition is the same that is used in one-way wave equation methods. The proposed strategy allows to improve the scalar fields in complex models even only using the extracted information that corresponds to the downgoing source wavefield.

In next section, we will develop a post-processing method to be applied it in the scalar field obtained RTM and ZL-CC-IC and will be compared with a conventional post-processing strategy.

References

[1] F. Liu, G. Zhang, S. Morton, and J. Leveille, *An effective imaging condition for reverse time migration using wavefield decomposition,* Geophysics **76**, 29 (2011).

[2] T. W. Fei and Y. Luo, *De-blending reverse time migration,* SEG 2010 International Exposition and Annual Meeting , 3130 (2010).

[3] T. Chen and B. He, *A normalized wavefield separation cross-correlation imaging condition for reverse time migration based on Poynting vector,* Applied Geophysics **11**, 158 (2014).

5

Laguerre-Gauss transform in seismic imaging filtering

Reverse time migration (RTM) solves the acoustic or elastic wave equation by means of the extrapolation from source and receiver wavefield in time. A Real scalar field is obtained by applying a criteria known as imaging condition. The cross-correlation between source and receiver wavefields is the commonly used imaging condition. However, this imaging condition produces spatial low-frequency noise, called artifacts, due to the unwanted correlation of the diving, head and backscattered waves. Several techniques have been proposed to reduce the artifacts occurrence. Derivative operators as Laplacian are the most frequently used. In this chapter, we propose a technique based on a spiral phase function ranging from 0 to 2π and a toroidal amplitude bandpass filter, known as Laguerre-Gauss transform. Through numerical experiments we present the application of this particular integral transform on three synthetic data sets. In addition, we present a comparative spectral study of images obtained by the zero-lag cross-correlation imaging condition, the Laplacian operator and the Laguerre-Gauss transform, showing their spatial frequency features. We also present evidences not only with simulated spatial noisy velocity fields but also by comparison with the velocity field gradients of the dataset that this method improves the RTM scalar fields by reducing the artifacts and notably enhance the reflective events.

In chapter 2 we introduced the reverse time algorithm and the zero-lag cross-corelation imaging condition to obtain migrated model of the subsurface. These models are contaminated by spatial low-frequency uncertainties (noise) called artifacts due to the superposition between waves such as head, diving and backscattered waves immersed in the source and receiver wavefields and the amplitude of migrated models.

Uncertainties reduction has been widely studied and several techniques have been proposed. Some of them strategies were briefly described in Youn and Zhou (2001) used the Laplacian image reconstruction to process each frame from correlation for an individual shot recorded, Fletcher et al. (2005), added a directional damping term to the non-reflecting wave equation proposed by Baysal et al. (1984) and Yoon and Marfurt (2006) used the Poynting vector to improve the cross-correlation imaging condition.

In chapter 3, we proposed the use of a singularity spectrum algorithm, based on wavelet analysis (WTMM), for extracting the main time-scale features of a signal. We applied this algorithm to the retrieval of information about the receiver wavefield at $z = 0$ in order to find information to understand phenomena related to attenuation and reflection. These algorithm allows to characterize the frequency spectrum and to analyze changes in the velocity field and their effect on wave propagation.

In chapter 4 we explored and improved the final scalar fields via wavefield separation performing a time-scale analysis and a singularity analysis to the seismic signals and the source and the receiver wavefields.

Finally, we also propose a new post-processing method to improve the migrated scalar fields and diminish the artifacts occurrence by applying a Laguerre Gauss transform with a spiral phase function to implement a Radial Hilbert transform to post-process the cross-correlation models [1].

First, we will describe the Laplacian operator to post-process migrated models, which is the regular technique employed to remove the artifacts in RTM models. Second, the proposed method is described in an extended way. Third, we compare the models obtained by zero-lag cross-correlation imaging condition, Laplacian operator, and the Laguerre Gauss transform applied to three synthetic datasets, to present evidences from the effectiveness of our imaging implementation to reduce the low-frequency spatial noise.

Then, we compare and analyze the spatial Fourier spectra obtained by the 2D spatial fast Fourier transform of the models obtained by zero-lag cross-correlation imaging condition (ZL-CC-IC), zero-lag cross-correlation imaging condition plus Laplacian operator (ZL-CC-IC-LP) and zero-lag cross-correlation imaging condition plus Laguerre-Gauss transform (ZL-CC-IC-LG) in order to establish quantitative measurements of the spatial spectral features looking for the first step to determine the accuracy and enhancement capability of the method to reach better subsurface structures [2, 3].

Finally, by comparison we carefully demonstrate that despite the smoothed velocity models the Laguerre-Gauss transform preserves well the reflections with their true locations and significantly attenuates the low frequency noise in the model [3, 4].

5.1. Integral kernel transforms

5.1.1. Laplacian operator

The Laplacian operator has been used for an edge enhancement in digital image processing [5].
Second-order derivative edge detection techniques employ some form of spatial second-order differentiation to accentuate edges. An edge is marked if a significant spatial change occurs in the second derivative [5]. The edge Laplacian (Laplacian model reconstruction) of an model function $F(x,z)$ is defined as

$$G(x,z) = -\nabla^2\{F(x,z)\} \tag{5.1}$$

where, the Laplacian operator is

$$\nabla^2 = \frac{\partial}{\partial x^2} + \frac{\partial}{\partial z^2} \tag{5.2}$$

$G(x,z)$ is zero if $F(x,z)$ is constant or changing linearly in amplitude. If the rate of change of $F(x,z)$ is greater than linear, $G(x,z)$ exhibits a sign change at the point of inflection of $F(x,z)$. The zero crossing of G $G(x,z)$ indicates the presence of an edge. The negative sign in the definition of equation (5.1) is present so that the zero crossing of $G(x,z)$ has a positive slope for an edge whose amplitude increases from left to right or bottom to top in a model [5].

Youn and Zhou, (2001, [6]) used a Laplacian model reconstruction operator to apply to the correlated image frames.
The Laplacian model reconstruction is given by

$$I_{LP}(x,z) = \frac{\partial}{\partial x^2} I_{cc}(x,z) + \frac{\partial}{\partial z^2} I_{cc}(x,z) \tag{5.3}$$

where $I_{cc}(x,z)$ is a model obtained by eq. 2.17 for a single source point (Cross-correlation model).
An effect associated with the application of the Laplacian operator is a $\frac{\pi}{2}$ phase shift and an amplitude change because it is a second-order differential. The phase shift in the reflective events can affect the interpretation of real scalar fields and induce a bad decision at the time of the exploration.
The Laplacian operator shows good attenuation of the migration artifacts. This operator has two major effects: (1) it removes the low-frequency information and (2) it increases the high-frequency noise [7].

It is well-known that Laplacian operator boosts the high frequencies relative to the low frequencies. Therefore, the Laplacian is often used to dampen low-frequency artifacts in reverse-time migration models when the background medium contains sharp wave velocity contrasts [8].
Based on this, we decided to propose the use of another method to reduce or eliminate the low-frequency artifacts and does not introduce other uncertainties in the scalar field . In next section this method will be described.

5.1.2. Laguerre-Gauss transform

Laguerre Gauss transform kernel uses a pure-phase function with a vortex structure in spatial frequency domain, defined as $B(f_x, f_z) = \tan^{-1}\left(\frac{f_z}{f_x}\right)$. The particular property from this spiral phase function is that is composed by a heavy-side function with a π gap when crossing the origin in every angular direction. In the amplitude, the kernel includes a gaussian toroidal geometry. This kernel is depicted in Figure 5.1.

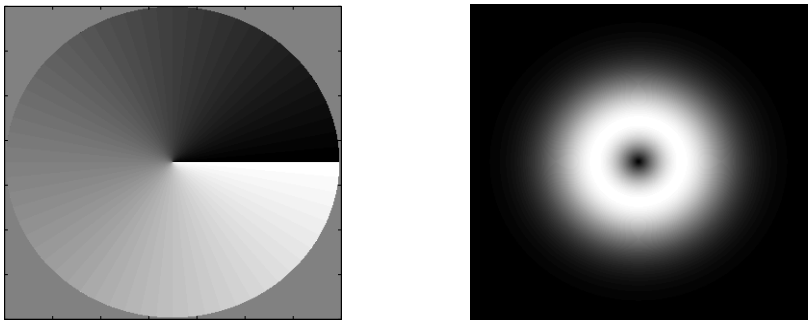

(a) (b)

Figure 5.1: Laguerre Gauss kernel: 5.1a Spiral phase function 5.1b Toroidal amplitude [9]

Let $I(x,z)$ be the scalar field obtained by RTM and ZL-CC-IC through eq. 2.8, 2.15 and 2.17, respectively. Let $\hat{I}(f_x, f_z)$ be the 2D Fourier transform of $I(x,z)$ expressed as

$$\begin{aligned} \mathcal{F} : \mathbb{R}^2 &\rightarrow \mathbb{C} \\ I(x,z) &\rightarrow \mathcal{F}\{I(x,z)\} = \hat{I}(f_x, f_z) \end{aligned}$$

and

$$\hat{I}(f_x, f_z) = \mathcal{F}\{I(x,z)\} = \int_{-\infty}^{\infty}\int_{-\infty}^{\infty} I(x,z) e^{-i(xf_x + zf_z)} dx dz \tag{5.4}$$

$I(x,z)$ may be related with its respective analytic model $\tilde{I}(x,z)$ by using a transformation kernel $LG(f_x, f_y)$, then

$$\tilde{I}(x,z) = \int_{-\infty}^{\infty}\int_{-\infty}^{\infty} LG\,(f_x, f_z)\,\hat{I}\,(f_x, f_z)\, e^{2\pi i(f_x x + f_z z)} df_x df_z \tag{5.5}$$

where

$$LG(f_x, f_z) = (f_x + i f_z)\, e^{-\left(\frac{f_x^2 + f_z^2}{\omega^2}\right)} = \rho e^{-\left(\frac{\rho^2}{\omega^2}\right)} e^{i\beta} \tag{5.6}$$

is a Laguerre-Gauss function in the frequency domain and $\rho = \sqrt{f_x^2 + f_z^2}$ and $\beta = \arctan(f_z/f_x)$ are the polar coordinates in the spatial frequency domain.

Taking into account eq. 5.6, the donut-shaped amplitude behaves as a bandpass filter suppressing low and high spatial frequency noise. The size of bandpass filter can be controlled by choosing the bandwidth parameter ω in eq. 5.6 [9], which changes the spatial frequency distribution in the obtained complex field. In this thesis, ω tends to one in order to preserve model spatial frequency distribution and perform the bandpass filter component from Laguerre Gauss.

After simple algebra, we find that

$$\tilde{I}(x,z) = \left|\tilde{I}(x,z)\right| e^{i\theta(x,z)} = I(x,z) * \mathbb{LG}(x,z) \tag{5.7}$$

where $*$ denotes convolution operation, and $\mathbb{LG}(x,z)$ is again a Laguerre-Gauss function in the spatial domain given by

$$\begin{aligned} \mathbb{LG}(x,z) = \mathcal{F}^{-1}LG(f_x,f_z) = & \quad (i\pi^2\omega^4)(x+iz)e^{-\pi^2\omega^2(x^2+z^2)} \\ = & \quad (i\pi^2\omega^4)[re^{-\pi^2r^2\omega^2}e^{i\alpha}] \end{aligned} \tag{5.8}$$

where $\mathcal{F}^{-1}$ is the 2D inverse Fourier transform expressed as

$$\begin{aligned} \mathcal{F}^{-1} : \mathbb{C} &\rightarrow \mathbb{R}^2 \\ LG(f_x,f_z) &\rightarrow \mathcal{F}^{-1}\{LG(f_x,f_z)\} = \mathbb{LG}(x,z) \end{aligned}$$

and $r = \sqrt{x^2+z^2}$ and $\alpha = arctan(z/x)$ are the spatial polar coordinates. The phase $\theta(x,z)$ of the complex signal is referred to as the pseudophase to distinguish it from the true phase of the scalar field $I(x,z)$.

5.1.3. Properties of the Laguerre-Gauss transform

The Laguerre-Gauss transform allows to realize an isotropic radial Hilbert transform without resolution loss [10]. In addition to the advantage of spatial isotropy common to the Riesz transform stemming from the spiral phase function with the unique property of a signum function along any section through the origin, the Laguerre-Gauss transform has the favorable characteristics to automatically exclude any DC component [11].

An effect associated with the application of the Laguerre-Gauss transform is the phase and amplitude changes in the final model. Figure 5.2 shows the close-up view of the phase of the pseudo complex field (Left) corresponding to the model obtained by zero-lag cross-correlation plus the Laguerre-Gauss transform around to the reflector and a vertical line profile (Right) at distance $x = 0.75$ Km. We can note that the Laguerre-Gauss transform changes the reflector phase in π.
Changes in amplitude are associated with the topological characteristics of the pseudo complex field and will be analyzed in future works to find its relation with seismic attributes such as amplitude and reflectivity.

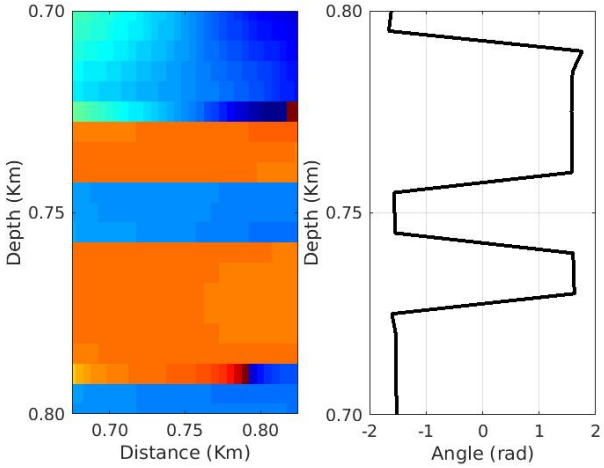

Figure 5.2: Phase (Left) and vertical line profile (Right) of pseudo complex field of Laguerre-Gauss model

5.2. Laguerre-Gauss transform of RTM scalar fields

We show the results for three synthetic datasets: Two-layer (Figure 2.7), 2D SEG-EAGE (Figure 2.12) and 2D Sigsbee2A (Figure 5.6a) applying the Laplacian operator and Laguerre-Gauss transform introduced above. We used a reverse time migration (RTM) algorithm with a second and eighth order finite difference scheme in time and space, respectively, described in chapter 2. The RTM scalar fields have been obtained using the zero-lag cross-correlation imaging condition (See eq. 2.17), the Laplacian operator (Eq. 5.3) and the Laguerre-Gauss transform (Eq. 5.5).

Two-layer velocity field

Figure 5.3b corresponds to the RTM two-layer scalar field obtained by cross-correlation imaging condition, it can be seen that model is contaminated with low frequency artifacts (Dark shadows) above and near the reflective event and in the shallow parts. This scalar field was obtained by the procedure described in section 2.4.

In Figure 5.3c we show the RTM result by using the Laplacian operator. The artifacts are reduced, but some high frequency noise remains in the model close to the surface. On the other hand, the result obtained by applying the Laguerre-Gauss transform (ZL-CC-IC-LG) is shown in Figure 5.3d. The artifacts in shallow parts and near the reflective event are significantly reduced and the subsurface structure focalized by the gather shots is more defined and enhanced.

2D SEG-EAGE salt velocity field

Figure 5.4b shows the SEG-EAGE scalar field obtained by applied RTM using the zero-lag cross-correlation imaging condition. This scalar field was obtained by the procedure described in section 2.4.

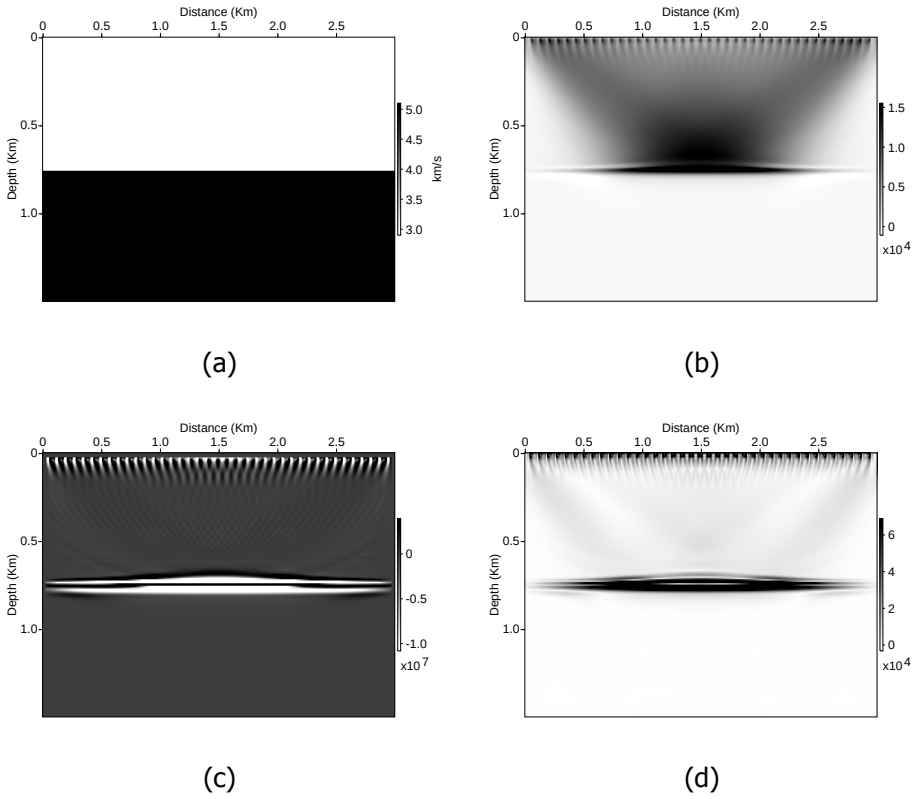

Figure 5.3: RTM of two-layer model using: 5.3a Velocity field, 5.3b zero-lag cross-correlation imaging condition, 5.3c zero-lag cross-correlation imaging condition plus laplacian operator, 5.3d zero-lag cross-correlation imaging condition plus Laguerre-Gauss transform

The model is contaminated with low frequency artifacts in the shallow parts and close to the salt body. We can note that these artifacts are located near at sharp interfaces and the shallow structures above the salt body are almost invisible.
Applying the Laplacian operator, the artifacts are reduced but in different parts there are some high frequency noise (Figure 5.4c). Figure 5.4d presents the model from using the Laguerre-Gauss transform presented in eqs. 5.5 and 5.6.

We demonstrate that the Laguerre-Gauss transform removes the undesired low frequency noise in the RTM models. Applying the Laguerre-Gauss transform to cross-correlation model the resulting model is improved: subsurface structures are more defined and the edges of the salt dome are enhanced. The artifacts in shallow parts and near the top salt dome are significantly reduced
The seismic model is improved to applying the Laguerre-gauss transform (Figure 5.4d): subsurface structures are more defined and the edges of the salt dome are enhanced. The artifacts are significantly reduced, the subsurface structures are

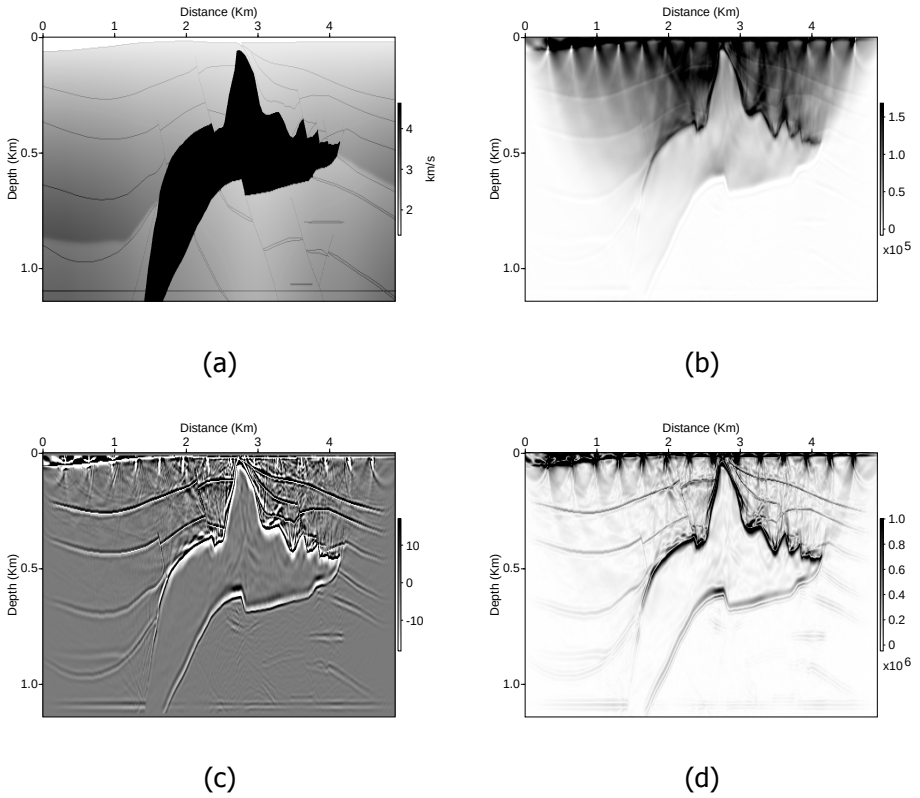

Figure 5.4: RTM of SEG-EAGE salt model using:5.4a Velocity field, 5.4b zero-lag cross-correlation imaging condition 5.4c zero-lag cross-correlation imaging condition plus laplacian operator, 5.4d zero-lag cross-correlation imaging condition plus Laguerre-Gauss transform.

more defined and the flanks of the salt body are enhanced.

We can note that the amplitude in the scalar field obtained by ZL-CC-IC plus laplacian operator changes abruptly compared to the scalar field obtained by ZL-CC-IC plus Laguerre-Gauss transform. This effect is important because if the amplitude field of the scalar field can be preserved, it can be related with the reflectivity and the geological characteristics of the subsurface. In future work this topic will be treated more deeply.

In Figure 5.5, a close-up view of two sections of the migrated model of SEG-EAGE is presented. The regions are marked with yellow boxes and these are depicted in Figure 5.5a. These were chosen due to its structure complexity. The artifacts reduction in models becomes apparent, by conducting the proposed technique models are improved and the salt body flanks are enhanced.

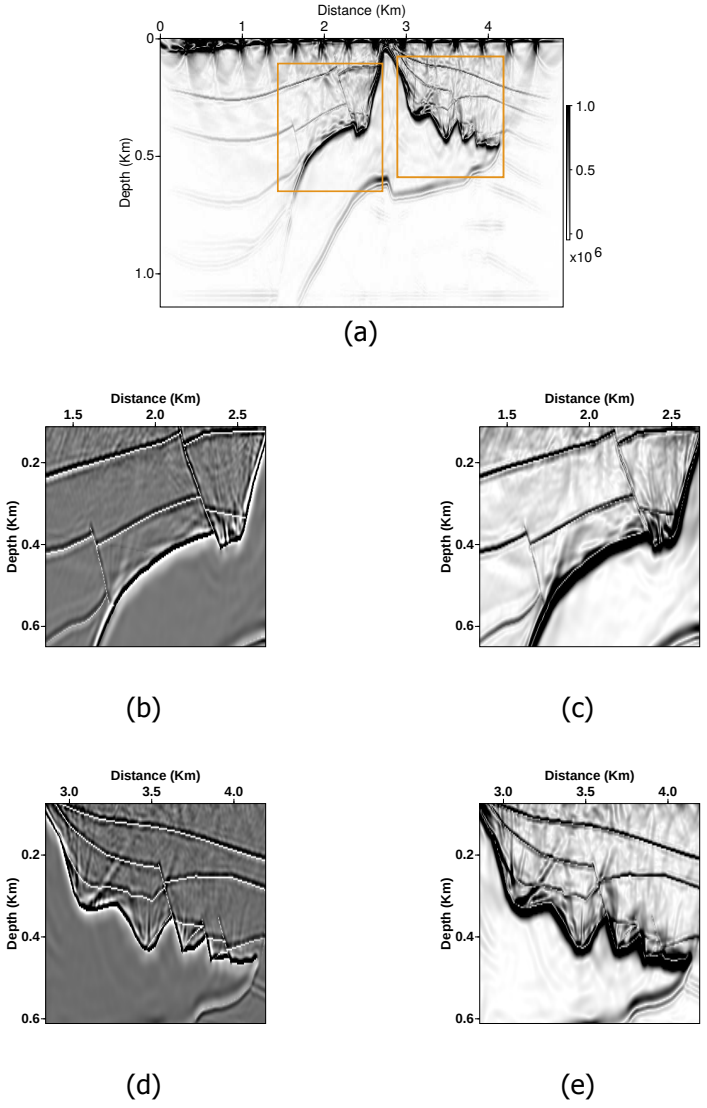

Figure 5.5: Detail of 2D SEG-EAGE RTM model with: 5.5a Details of the outline regions, 5.5b and 5.5d Laplacian operator, 5.5c and 5.5e Laguerre-Gauss transform

2D Sigsbee2A velocity field

Similarly, we apply the Laguerre Gauss filtering to 2D Sigsbee 2A model. Sigsbee 2A is a synthetic model of deep water in the Gulf of Mexico. It is characterized by the complex salt shape with rugose salt top found in this area. The velocity model is shown in Figure 5.6a.

In Figure 5.6 is shown a comparison of models obtained by zero lag cross-correlation imaging condition, laplacian operator and Laguerre-Gauss transform. The RTM

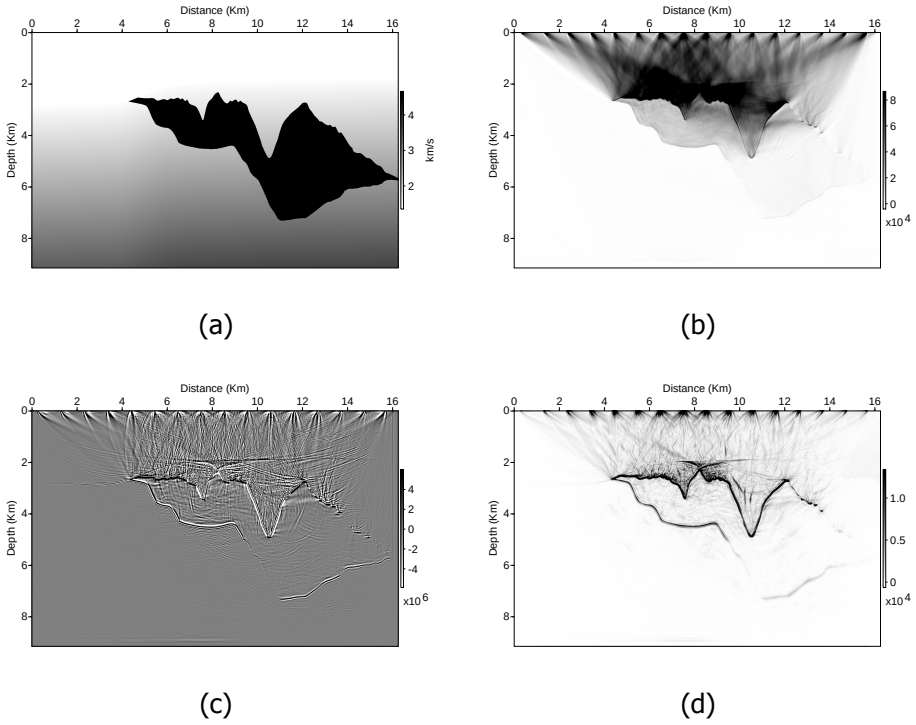

Figure 5.6: RTM of Sigsbee2A salt model using:5.6a Velocity field, 5.6b zero-lag cross-correlation imaging condition 5.6c zero-lag cross-correlation imaging condition plus laplacian operator, 5.6d zero-lag cross-correlation imaging condition plus Laguerre-Gauss transform.

model was obtained using only sixteen sources distributed along the surface. The first source is located at 0.15 Km and the last one at 7.68 Km from the beginning of the model on the surface, the source interval is 506.1 m, each source contains 2133 receivers and the receiver interval distance is 3.75 m.

In order to verify that the results obtained by using the proposed technique match the velocity field interfaces, we proceed to overlap the found interface structures using red lines. Red lines are obtained eroding the contrast inverted Laguerre-Gauss grayscale model, by means of the convolution between the image and a disk with 2-pixel radius. The objects smaller than the mask disappear and a zero is assigned in its place, the positions of the remaining objects are assigned a one. To these binarized model a skeletonization process is applied by obtaining the distance transform of the model. The model skeleton lies along the transform singularities.

Figure 5.7a presents the interfaces obtained when using the proposed technique overlapped with the SEG-EAGE velocity field, it should be noted the high correspondence between the obtained interfaces with those presented in the model, and Figure 5.7b shows the magnitude of the velocity gradient of the SEG-EAGE velocity

model.

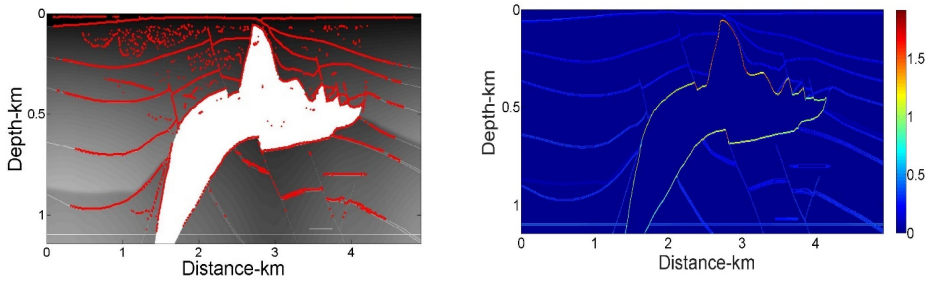

Figure 5.7: 5.7a Comparison between image obtained with Laguerre Gauss filtering and the initial model of the 2D SEG-EAGE 5.7b Magnitude of the velocity gradient.

We can note that the enhanced edges and flanks of the salt body coincide with the structures present in the velocity model and they are in their true locations. In addition, some details below the salt body are enhanced and better illuminated. The geometry of the salt bodies gives rises to poorly illuminated regions, specifically, below them and the Laguerre-Gauss filter can detect and enhance small amplitude changes.

This effect is evident when comparing the image obtained by Cross-correlation imaging condition plus Laguerre-Gauss filter with the magnitude of the velocity gradient in areas below the salt body. Despite of the small changes in the magnitude of the velocity gradient, the structures are enhanced

5.2.1. Effects of the Laguerre-Gauss transform in the magnitude spectrum

In order to describe properly the Laguerre-Gauss transform, the magnitude of the spatial Fourier spectrum of the image.s of both models presented above is shown in Figure 5.8 and 5.9 (Left column). It is interesting to find out a way to properly compare the results of the post processing procedure so we perform the line profile of the Fourier Spectrum in order to extract features [12] and compare the intensity profiles and related them to the enhancement of the edges in the structural model. The horizontal (x- axis) and vertical (z- axis) line profile is evaluated in each spectrum (center and right column, respectively). The top row corresponds to the zero lag cross-correlation model crossing the origin of the Fourier spectrum, the center row to the cross-correlation image plus Laplacian filtering and the bottom row to the cross-correlation image plus Laguerre-Gauss filtering.

Two-layer velocity field

Figure 5.8 shows the magnitude of the spatial Fourier spectrum (left) and horizontal (center) and vertical (right) line profiles of the models of the two-layer model showed in Figure 5.3.

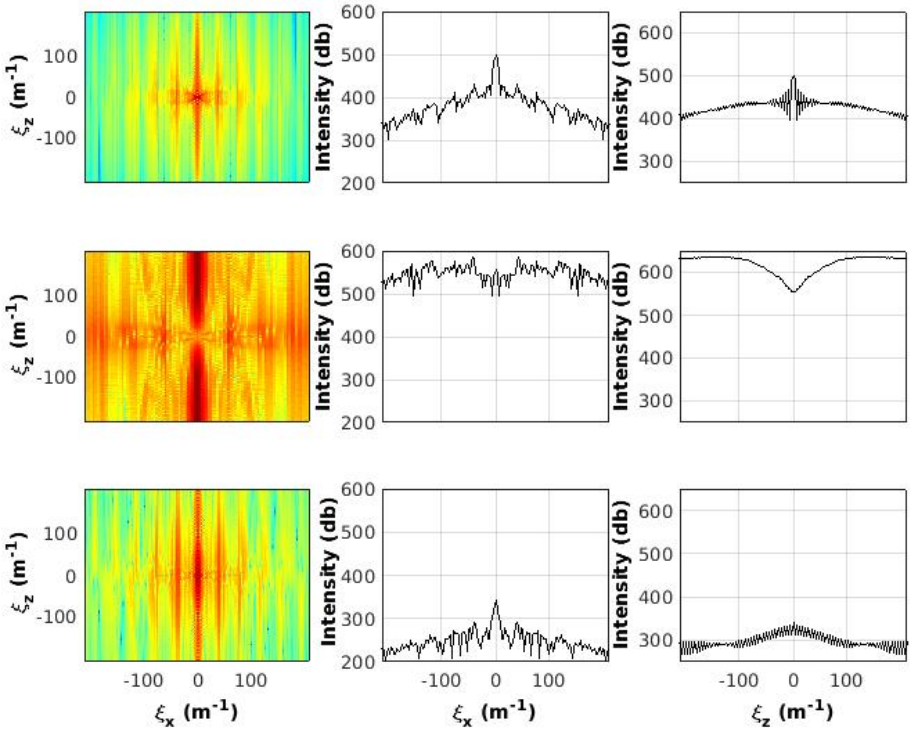

Figure 5.8: Magnitude of the spatial Fourier spectrum and horizontal and vertical line profiles from models presented in Figure 5.3

From vertical profile, we can note that the Laplacian filtering modifies the intensity of low frequencies abruptly and increases the intensity in high frequencies. In horizontal profile, the intensity of the line profile was increased in all frequency values. These modifications are evidenced in the strong changes in the shape of the line profiles from the Fourier spectrum of the Laplacian image respect to the Fourier spectrum of cross-correlation model [2].

On the other hand, the Laguerre-Gauss filtering shows a good behavior due to its isotropic feature. In addition to the advantage of spatial isotropic common to the Riesz transform stemming from the spiral phase function, the Laguerre-Gauss transform has the favorable characteristics to automatically exclude any DC component of the original input function [9]. The intensity at low and high frequencies are distributed smoothly and homogeneously. The shape of the horizontal line profile of Laguerre-Gauss spectrum is similar to the horizontal line profile of the cross-correlation spectrum. In vertical profile the variations in intensity at high and low frequencies are attenuated and smoothed.

SEG-EAGE salt velocity field

As presented in previous section for the two-layer model, the spatial Fourier spectra and the horizontal and vertical line profiles are analyzed in order to quantify the effect of the Laplacian and Laguerre-Gauss filtering in the Fourier spectrum of the cross-correlation image of the 2D SEG-EAGE salt model.

In Figure 5.9, the top row corresponds to the magnitude spectrum and the horizontal and vertical lines profiles of the cross-correlation image, respectively, the center row to the cross-correlation image plus Laplacian filtering and the bottom row to the cross-correlation image plus Laguerre-Gauss filtering. Similarly, horizontal and vertical line profiles cross the origin of the Fourier spectrum.

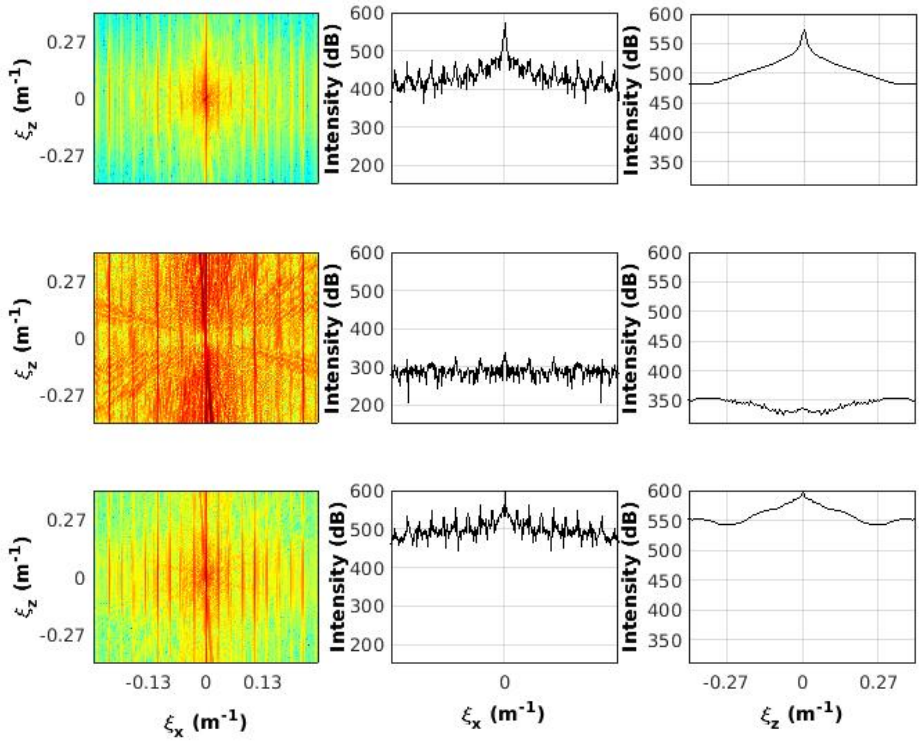

Figure 5.9: Magnitude spectra and horizontal and vertical line profiles from images of 2D SEG-EAGE RTM presented in Figure 5.4

The Laplacian filtering shows a strong attenuation of the intensity at high and low frequency noise, modifying the shape of the line profiles, and changing the intensity in each spatial frequency value. We can note this effect in the shape of the horizontal and vertical line profiles. In the vertical line profile, the reduction is more evident in the intensity at low frequencies values. Laguerre-Gauss filtering shows that the intensity in all frequency values are modified homogeneously and smoothly.

The shape of the horizontal line profile is similar to the shape of the horizontal line profile of the cross-correlation spectrum. From vertical line profile, we can note that the variations of the intensity are smoother and evenly distributed.
In conclusion, the Laguerre-Gauss filter has a good behavior and distributed homogeneously and smoothly the intensity of the magnitude of the Fourier spectrum due to its isotropic feature. The shape of the line profiles that cross the origin of the Fourier spectrum is similar to the line profiles of the Fourier spectrum of the cross-correlation image but the intensity in all frequency values are distributed smoothly.
In next section, the good performance of the Laguerre-Gauss transform will be explored through the robust need against certain uncertainties in velocity fields due to the real lack of accurate information of the velocity fields for RTM procedure. It is clearly reasonable to claim that if the RTM procedure receives an inaccurate velocity model, the resulting imaging condition can contain certain undesirable frequency effects. If a transformation such as the proposed one is used in a post processing stage, the model obtained can improve significantly compared to the traditional post-processing approach and behaves properly in certain sections of the subsurface such as highly singularity regions.

5.2.2. Uncertainties in wave propagation velocity fields

We evaluate the capability of the Laguerre-Gauss transform on the 2D SEG-EAGE salt model. We applied RTM using the ZL-CC-IC-LG with the original and two smoothed velocity fields. The velocity fields were smoothed by using a 2D spatial Gaussian filter with two arbitrary chosen standard deviations of 10 and 20.

Figure 5.10 shows the original SEG-EAGE velocity field and the RTm scalar field with ZL-CC-IC-LG.

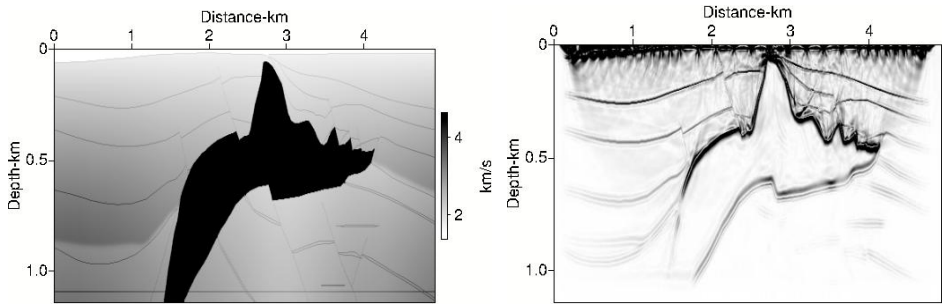

(a) Original velocity field (b) Laguerre-Gauss model of 5.10a

Figure 5.10: The original SEG-EAGE velocity field 5.10a and its RTM results with ZL-CC-IC-LG 5.10b

The resulting scalar fields from the smoothed velocity fields and thier RTM scalar field with ZL-CC-IC-LG are shown in Figure 5.11.
Figure 5.10b shows the model obtained by ZL-CC-IC-LG using the original velocity field (Figure 5.10a). We obtain a good structural model where the artifacts are

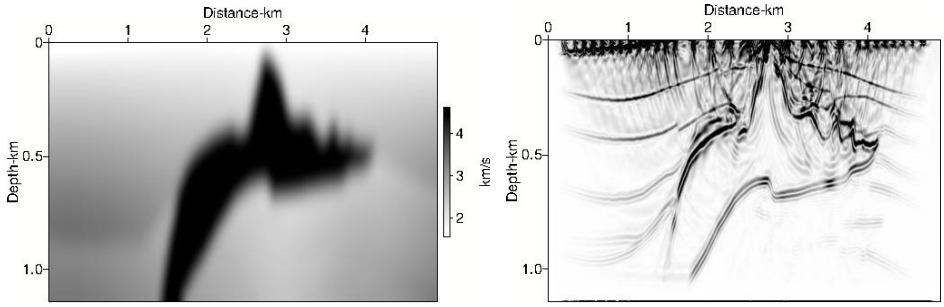

(a) Smoothed velocity field with standard deviation of 10

(b) Laguerre-Gauss model of 5.11a

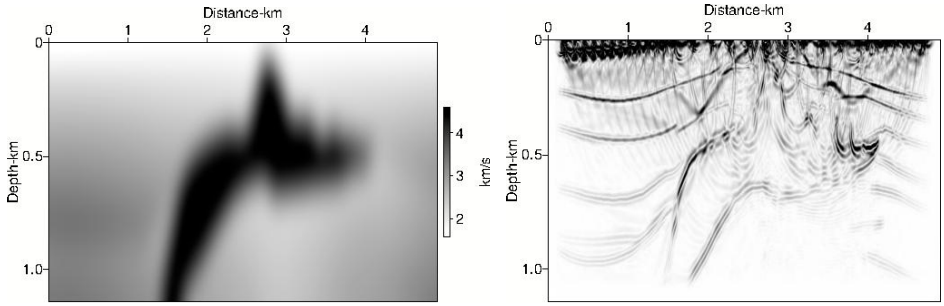

(c) Smoothed velocity field with standard deviation of 20

(d) Laguerre-Gauss model of 5.11c

Figure 5.11: Smoothed with standard deviation of 10 5.11a and smoothed with standard deviation of 20 5.11c 2D SEG-EAGE velocity field used for migration. RTM scalar fields with ZL-CC-IC-LG 5.11b and 5.11d for velocity fields 5.11a, 5.11c, respectively.

significantly reduced, the subsurface structures are more defined and the flanks of the salt body are enhanced [4].

In Figure 5.11a and 5.11b, the velocity field smoothed with the spatial Gaussian filter with standard deviation of 10 and the model obtained by ZL-CC-IC-LG are shown, respectively. The artifacts in shallow parts and near the salt dome are significantly reduced. The edges are enhanced, especially the salt flanks of the salt body. From Figure 5.11d, we can note that the flanks of the salt body are enhanced, even below the salt dome. Similarly, artifacts in the model are reduced and the subsurface structures are well delineated and located in their correct position. Despite the smoothed velocity field, the Laguerre-Gauss transform has a good behavior by enhancing the structures and flanks of the salt body and the reduction of low spatial artifacts. It is capable of detecting even very small changes.

In presence of smoothed velocity fields, the Laguerre-Gauss transform obtain similar results, achieving the reduction of low-frequency noise and preserving the reflective events, enhancing any small change in the seismic image and preserving the true

locations of reflections.
Independent of the phenomena of attenuation of the propagated wave or of the contamination of the velocity field with uncertainties, the Laguerre-Gauss transform allows to locate reflective events that not be perceived by the human eye and which affect the interpretation of the scalar fields, due to its isotropic and edge enhancement properties.

Summary

In this chapter we described a new post-processing method of the scalar field by using the Laguerre-Gauss transform. This integral transform maps the real scalar field obtained by RTM and ZL-CC-IC into a complex scalar field with improved features. The Laguerre-Gauss transform allows to attenuate the low-frequency spatial artifacts, reduce the high frequency spatial noise and enhanced the subsurface structures.
We demonstrated that the Laguerre-Gauss transform applied on RTM scalar fields, in presence velocity fields with or without uncertainties, has a good behavior, reducing the artifacts and preserving the reflective events. With this transformation the seismic scalar fields are improved and we obtained a good structural scalar fields that are a good representation of the subsurface structure.
We showed that the Laguerre-Gauss transform has a good behavior and distributed homogeneously and smoothly the intensity of the magnitude of the Fourier spectrum due to its isotropic feature. The shape of the line profiles of this is similar to the line profiles of the Fourier spectrum of the cross-correlation scalar field but the intensity in all frequency values are distributed smoothly.
Despite of the smoothing of the velocity fields, the Laguerre-Gauss transform is capable to enhance any small changes in the seismic scalar field and preserving the true location of reflections. This can be important for real data examples where the velocity field is not accurate and more relevant in the reduction of uncertainty in the interpretation of the scalar fields.

References

[1] J. G. Paniagua and D. Sierra-Sosa, *Laguerre Gaussian filters in Reverse Time Migration image reconstruction,* VII Simpósio Brasileiro de Geofísica. Expanded abstract (2016).

[2] J. G. Paniagua and O. L. Quintero, *The use of Laguerre-Gauss transform in 2D reverse time migration imaging,* 15th International Congress of the Brazilian Geophysical Society. Expanded abstracts (2017).

[3] J. G. Paniagua, D. Sierra-Sosa, and O. L. Quintero, *Laguerre-Gauss filters in reverse time migration image reconstruction,* Revista Brasileira de Geofísica (2017).

[4] J. G. Paniagua and O. L. Quintero, *Attenuation of reverse time migration ar-*

tifacts using Laguerre-Gauss filtering, 79th EAGE Conference and exhibition. Extended abstracts (2017).

[5] W. K. Pratt, *Digital image processing* (Wiley Interscience, 2001).

[6] O. Youn and H. Zhou, *Depth imaging with multiples,* Geophysics **66**, 246 (2001).

[7] A. Guitton, A. Valenciano, D. Bevc, and J. Claerbout, *Smoothing imaging condition for shot-profile migration,* Geophysics **72**, 149 (2007).

[8] A. Guitton, B. Kaelin, and B. Biondi, *Least-square attenuation of reverse time migration,* 76th International Annual Meeting, SEG, Expanded abstracts , 2348 (2006).

[9] W. Wang, T. Yokozeki, R. Ishijima, M. Takeda, and S. G. Hanson, *Optical vortex metrology based on the core structures of phase singularities in Laguerre-Gauss transform of a speckle pattern,* Optics Express **14**, 10195 (2006).

[10] C. Gou, Y. Han, and J. Xu, *Radial Hilbert transform with Laguerre-Gaussian spatial filters,* Optics Letters **31**, 1394 (2006).

[11] Z. Wang, H. Ding, G. Lu, and X. Bi, *Reverse-tiome migration based optical imaging,* IEEE Transactions on medical imaging **35**, 273 (2016).

[12] D. Sierra-Sosa, M. Bastidas, and O. L. Quintero, *Double Fourier analysis for emotion identification in voiced speech,* Journal of Physics **705** (2016).

6

Conclusion

The scalar fields obtained by reverse time migration with the zero-lag cross-correlation imaging condition present spatial low-frequency uncertainties. These uncertainties are produced by unwanted correlation of the diving, head and backscattered waves in the wave propagation phenomenon.

We illustrated the behavior of the wave propagation and the generation of scalar fields with uncertainties through several numerical examples in order to understand how the numerical effects, the changes in amplitude of the wavefields and changes in frequency content of the wave traveling through mediums with strong velocity gradients can cause undesired results.

In this thesis, we proposed and developed two methods to reduce or to eliminate the uncertainties in the scalar fields taking into account the features of the linear integral transforms and their ability to extract information from different types of signals defined and supported in different domains.

First, a method based on the time-scale analysis and the singularity analysis of signals via the continuous wavelet transform, the wavelet transform modulus maxima and the Hölder exponent was proposed. This method allowed to analyze the features of the seismic traces from the receiver wavefield at $z = 0$, extracting their main information in the time-scale domain.

The time-scale and singularity analysis allowed a characterization of the signal and a measure of its regularity through the Hölder exponent when the scale decreases. In small scales, the use of the wavelets of the Gaussian family as used in this thesis, allows to relate the maximum lines with the solutions of the heat equation.

Taking into account the features of the CWT, we applied it on some subsets of the source and receiver wavefields in order to extract relevant information that allowed to separate the wavefields in their upgoing and downgoing components, subsets of the source and receiver wavefields, respectively.

The selection of the subsets was not arbitrary, on the contrary, the scalograms were analyzed one by one in order to find relevant characteristics that allowed to find some regularity in the analyzed signals.

According to the similarity of the characteristics of the scalograms, the values of the CWT coefficients located in the time-scale domain were located in the time-space domain, finding the values of a relative maximum and its neighborhood, both for source and receiver wavefields. This allowed us to locate the reflective events with a better accuracy and obtain an improved scalar field, with an evident reduction of uncertainties.

Time scale wavefield separation (TSWS) was applied in simple and complex velocity fields and the results were promising. We achieved the improvement of the scalar field using only the separated source wavefield and the complete receiver wavefield, considerably reducing the uncertainties induced by the undesired correlation of some subsets of the source and reciever wavefields. The information about the downgoing component of the source wavefield can be extracted adequately.

The information about the upgoing component of the receiver wavefield was partially extracted and in future work, the full extraction of information about this component of the receiver wavefield will be studied and the characteristics obtained through the CWT and WTMM will be analyzed.

We proposed the use of the Laguerre-Gauss transform to post-process the scalar field obtained by RTM and ZL-CC-IC. This transformation maps the RTM real scalar field into a complex scalar field using a complex-valued kernel composed by a spiral phase function and a gaussian toroidal amplitude. The Laguerre-Gauss transform reduces the low-frequency uncertainties and the high spatial frequency components that create unstable phase singularities. In addition, this transformation enhances the edges in the scalar field.

The scalar field that represents the subsurface structures corresponds to the amplitude of the complex scalar field. This representation of the subsurface is a good approximation of the geological structures. However, the amplitude field is not preserved, that is, we could not find a relationship of the amplitude of the complex scalar field with the reflectivity of the media. But we compared the effects of the Laguerre-Gauss transform and the laplacian operator in the amplitude of the scalar field and we found that the laplacian operator abruptly changes the value of the amplitude and the Laguerre-Gauss transform makes smooth amplitude changes due to the gaussian properties of the Laguerre-Gauss function.

We showed that the Laguerre-Gauss transform has a good behavior and distributed homogeneously and smoothly the intensity of the magnitude of the spatial Fourier spectrum due to its isotropic feature. The shape of the line profiles that cross the origin of the spatial Fourier spectrum is similar to the line profiles of the spatial Fourier spectrum of the scalar field obtained by RTM and eq. 2.17 but the intensity in all frequency values are distributed smoothly.

In addition, in presence of smoothed velocity fields, the Laguerre-Gauss transform obtain similar results, achieving the reduction of low-frequency uncertainties and preserving the reflective events, enhancing any small change in the scalar field and preserving the true locations of reflections

The methods described in this thesis looking for make a contribution to the exploration of hydrocarbons in order to reduce the uncertainty in the interpretation stage, providing seismic scalar fields with high resolution and fidelity, with preservation of amplitudes and a clear delineation of structures in complex geological areas both onshore and offshore. The relationship between of the amplitude of the scalar fields and the seismic attributes such as amplitude and reflectivity fields will be developed and analyzed in a future research.